Shahid Beheshti
University

Faculty of
Physics

Universiteit
Antwerpen

Faculteit
Wetenschappen
Departement
Fysica

Many body properties in monolayer and doublelayer black phosphorus

Veel-deeltjes eigenschappen in monolaag en dubbellaag fosfeen

Thesis submitted to achieve the degree of doctor of science by

Samira Saberi-Pouya

Supervisors:

Dr. Taraneh Vazifehshenas
Shahid Beheshti University, Tehran, Iran

Prof. Dr. Francois Peeters
University of Antwerpen, Antwerpen, Belgium

June 2018

I am dedicating this thesis to my brother "Hojat" gone forever away from our loving eyes and who left a void never to be filled in our lives. Though your life was short, I will make sure your memory lives on as long as I shall live. I love you and miss you beyond words.

Members of the Jury:

Chairman: Dr. Farshad Ebrahimi, Shahid Beheshti University, Tehran, Iran.

Members:

- Prof. Dr. Naser Nafari, Instituted for Research in Fundamental Science and Sharif University of Technology, Tehran, Iran.
- Dr. Seyed Akbar Jafari, Sharif University of Technology, Tehran, Iran.
- Dr. Farshad Ebrahimi, Shahid Beheshti University, Tehran, Iran.
- Dr. Ali Sadeghi, Shahid Beheshti University, Tehran, Iran.

Many thanks to financial support of my PhD by:

- Iran Ministry of Science, Research and Technology
- Iran Science Elites Federation
- Fonds Wetenschappelijk Onderzoek (FWO)

Acknowledgements

I would like to express my sincere gratitude to my supervisor at Shahid Beheshti university in Iran "Dr. Taraneh Vazifehshenas" for her support and guidance. Our meetings and discussions made this thesis possible. Also, a special thanks goes to Prof. Dr. Francois Peeters my supervisor at university of Antwerp for creating such a nice work environment and making it possible for me to work in the CMT group.

Further, I'd like to thank Dr. Mohammad Zarenia, Prof. Dr. Andrea Perali, Dr. Mojtaba Farmanbar and Dr. Taha Salavati-Fard for a nice collaboration and all the discussions, which have led to a better understanding of my work.

I would also like to thank my friends. We were not only able to support each other by deliberating over our problems and findings, but also happily by talking about things other than our papers. Thank you so much Haniyeh, Neda, Nasrin and Maryam. Thank you so much to all my friends in CMT group especially Sara, Rebeca and Victor.

I owe so much to my whole family for their undenying support, their unwavering belief that I can achieve so much. I just want you all to know that you count so much. Had it not been for all your prayers and blessing; were it not for your sincere love and help, I would never have completed this thesis. So thank you all.

Last, I owe a special thank to my fiance "Amin" who was beside me during the writing of my thesis. Your support and encouragement strengthened me when I needed them, thank you so much.

Contents

List of figures

List of tables

List of abbreviations

zz	Zigzag
ar	Armchair
GPa	Gigapascal
vdW	van der Waals
PL	Photoluminescence
BP	Black phosphorus
GaAs	Gallium arsenide
SiC	Silicon carbide
SiO_2	Silicon dioxide
Al_2O_3	Aluminum oxide
2D	Two-dimensional
3D	Three-dimensional
SOC	Spin-orbit coupling
MoS_2	Molybdenum disulfide
CDW	Charge density wave
SDW	Spin density wave
h-BN	Hexagonal boron nitride
FET	Field effect transistor

AFM	Atomic force microscopy
RPA	Random phase approximation
LFC	Local field correction
VBM	Valence band maximum
CBM	Conduction band minimum
2DEG	Two-dimensional electron gas
TMDC	Transition-metal dichalcogenide
SEM	Scanning electron microscope
TEM	Transmission electron microscopy
EELS	Electron energy-loss spectroscopy
ARPS	Angle resolved photoemession spectroscopy

Chapter 1

Introduction

> “Begin at the beginning,¨ the King said gravely, “and go on till you come to the end: then stop."
>
> Lewis Carroll

1.1 The rise of 2D materials

The isolation of graphene in 2004 from graphite was a defining moment for the birth of a new field: two-dimensional (2D) materials. In recent years, there has been a rapidly increasing number of papers focusing on two-dimensional (2D) atomic-layer systems, including graphene [1, 2, 3], transition metal dichalcogenides (TMDCs) [4, 5, 6], hexagonal boron nitride (h-BN) [7, 8] and phosphorene (a single layer of Black phosphorus (BP)) [9], as candidate materials for future electronic applications. Compared with traditional three dimensional (3D) materials such as gallium arsenide (GaAs) and silicon (Si), 2D materials exhibit many exceptional properties. First, quantum confinement in the direction perpendicular to the 2D plane leads to novel electronic and optical properties that are distinctively different from their bulk parental materials [10, 11]. Second, their surfaces are naturally passivated without any dangling bonds, which makes it easy to integrate 2D materials with photonic structures [12]. Third, despite being atomically thin, many 2D materials interact strongly with light. For example, a single layer of MoS_2

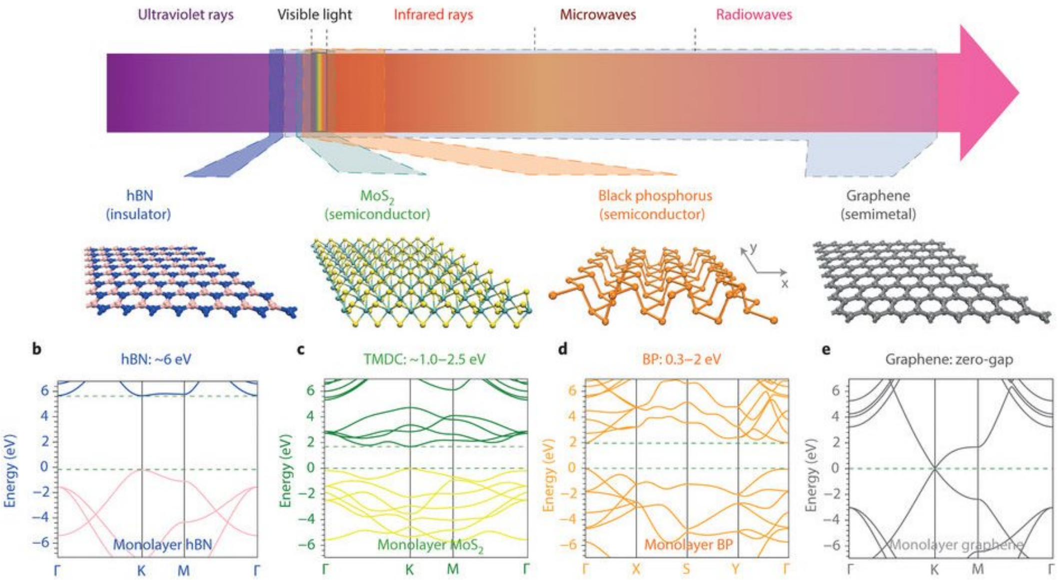

Figure 1.1: (a) Electromagnetic spectrum. Band structures of single-layer (b)h-BN, (c) MoS$_2$, (d)BP, and (e) graphene. Figure taken from Ref. [14].

absorbs around 10% of vertically incident light at excitonic resonances (615 nm and 660 nm) [13]. Finally, 2D materials can cover a very wide range of the electromagnetic spectrum because of their diverse electronic properties (Fig. 1.1(a)).

A high-performance device such as a field-effect transistor (FET) requires a moderate electronic band gap, a reasonably high carrier mobility of the channel material and excellent electrode-channel contacts. Graphene offers extremely high mobilities, due to its very low carrier effective mass, and thus is considered to be a promising candidate for high-speed FET devices, but its intrinsic dispersion is gapless [15, 16]. Despite extensive efforts following a wide variety of approaches to the problem of opening a gap in different graphene nanostructures, all devices to date have a relatively large 'off' current and thus a low 'on−off' ratio. For this reason the emergence of monolayer TMDCs has attracted substantial research interest, and in particular MoS$_2$ (Fig. 1.1(c)) has recently been used to fabricate a FET [17]. Unlike graphene, monolayer MoS$_2$ is a direct-bandgap semiconductor with a carrier mobility of $\approx$200 cm^2 V^{-1} s^{-1}, improvable up to 500 cm^2 V^{-1} s^{-1} [18], a value which is not unreasonable for applications but remains orders of magnitude lower than that of graphene [19]. h-BN is another important type of 2D material

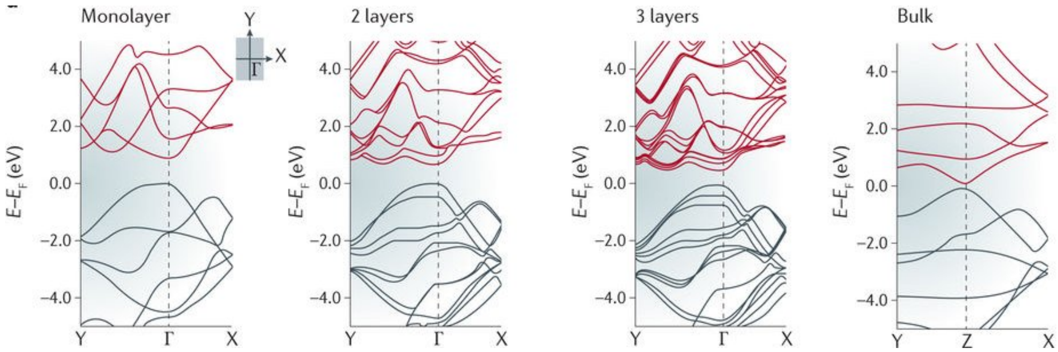

Figure 1.2: Band structures obtained by density functional theory for one, two and three layers of phosphorene, and for bulk black phosphorus. Figure taken from Ref. [21].

[20]. It has a large band-gap of around 6 eV (Fig. 1.1(b)), which makes it an excellent dielectric, and can be incorporated into various heterostructures for the electrostatic gating of other 2D materials, as 'lattice matching' is not necessary in these van der Waals heterostructures. Different from Graphene, TMDCs and *h*-BN, the recently rediscovered BP (Fig. 1.1(d)) exhibits a direct bandgap of around 0.3 eV in its bulk form which increases up to 2 eV in its monolayer form. Thus the entire community working on atomic layer transport continues to search for a 2D material which is semiconducting, preferably with a direct band gap, has high carrier mobility and has the potential to form excellent contacts with known electrode materials.

1.2 Phosphorene

In the family of 2D materials, phosphorene, a monolayer of black phosphorus (BP), with puckered structure has recently attracted considerable attention because of the unique physical properties associated with its anisotropic band structure [21, 22, 23, 24, 25]. BP is the most thermodynamically stable phase of phosphorus at ambient temperature and pressure [26, 27]. BP was discovered by P. W. Bridgman in 1914 in an attempt to convert white phosphorus to red phosphorus using high hydrostatic pressure [28]. This was achieved using a 200^{o}C oil bath and 1.2 GPa of pressure. Bridgman found that BP was more dense than either white or red phosphorus, and also the most stable allotrope of the three in air. BP consists of puckered hexagonal layers

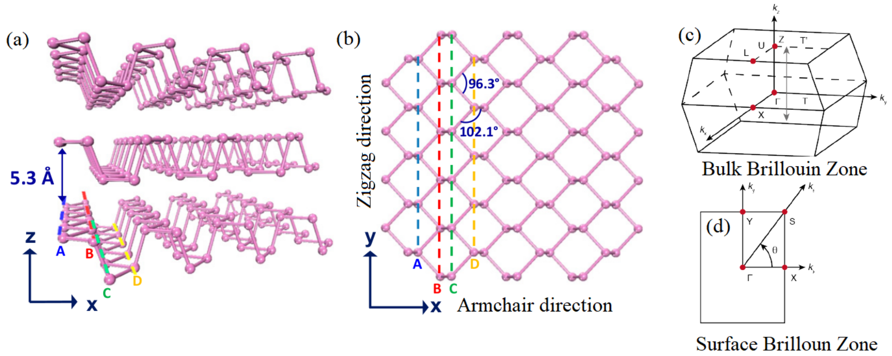

Figure 1.3: Crystal structure and band structure of BP. (a) Side view of the BP crystal lattice. The interlayer spacing is $0.53nm$. (b) Top view of the lattice of single-layer BP. (c) 3D bulk Brillouin zone (top) and (d) corresponding 2D surface Brillouin zone (bottom) of BP. The high-symmetry points are marked by red circles. The bond angles are shown. The corresponding x, y, and z directions are indicated in both A and B. x and y correspond to the armchair and zigzag directions of BP, respectively. Figure taken from Ref. [22].

that coupled through weakly van der Waals interlayer interactions [29, 30]. Such as graphene and $h - BN$, monolayer and few-layer of BP can be exfoliated from its bulk material with great potential for applications in new 2D electronic devices [31, 32]. BP is a layered material in which each layer forms a puckered surface due to sp^3 hybridization. In its bulk crystalline form, BP is a semiconductor with a direct band gap of 0.3 eV which reaches up to 2 eV in the monolayer structure (see Fig. 1.2) [33, 9]. Phosphorene has a direct energy gap [33] and high carrier mobility [34, 35] which has recently attracted significant attention as a new 2D semiconductor material for electronic and optoelectronic applications [35, 36, 37, 38, 23]. BP is a single-elemental layered crystalline material consisting of only phosphorus atoms. Unlike in group IV elemental layered materials, such as graphene, silicene, or germanene, each phosphorus atom has five outer shell electrons. BP has three crystalline structures: orthorhombic, simple cubic, and rhombohedral. The single-layer BP includes two atomic layers and two kinds of P–P bonds. The shorter bond length of 0.2224 nm connects the nearest P atoms in the same plane, and the longer bond length of 0.2244 nm connects P atoms between the top and bottom of a single layer. A top view of BP along the z

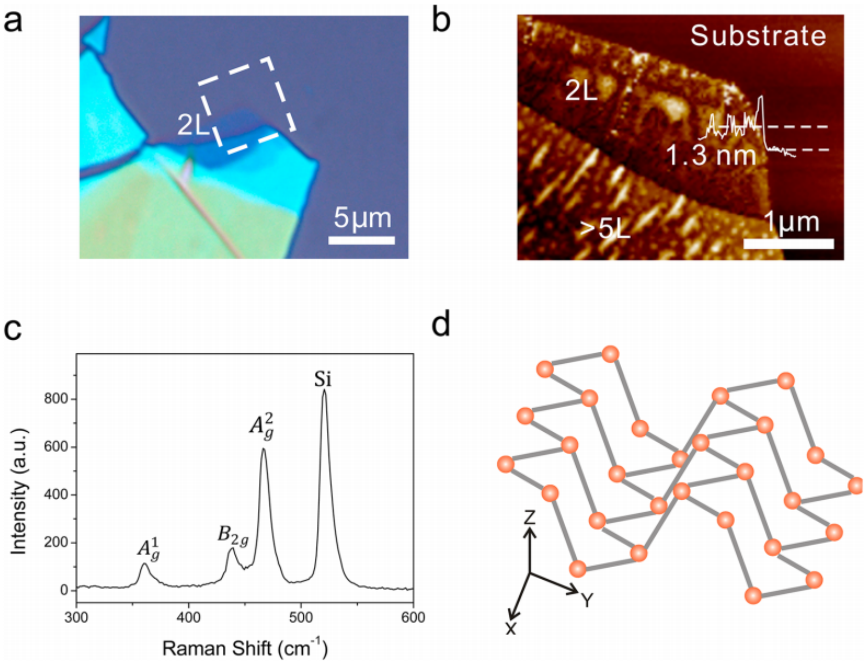

Figure 1.4: Images and characterization of exfoliated phosphorene. (a) Microscope image of 2L phosphorene. (b) AFM image of 2L phosphorene, with region indicated in the dashed line box in (a). (c) Raman spectrum of 2L phosphorene. (d) Schematic plot of phosphorene layer structure. Figure taken from Ref. [48].

direction shows a hexagonal structure with bond angles of 96.3° and 102.1° (See Fig. 1.3) [22].

A special feature of phosphorene is the high in-plane anisotropy of its energy band structure. This anisotropy comes from the layered puckered-honeycomb structure of phosphorene resulting from sp^3 hybridization of phosphorene. Motivated by this peculiar property, several theoretical and experimental studies investigated different anisotropic properties of phosphorene [21, 39, 40, 41]. Recently, many-body aspects of phosphorene have been also addressed through the study of collective excitation modes in a doped monolayer and in coupled phosphorene bilayers [42, 43, 44, 45, 46, 47].

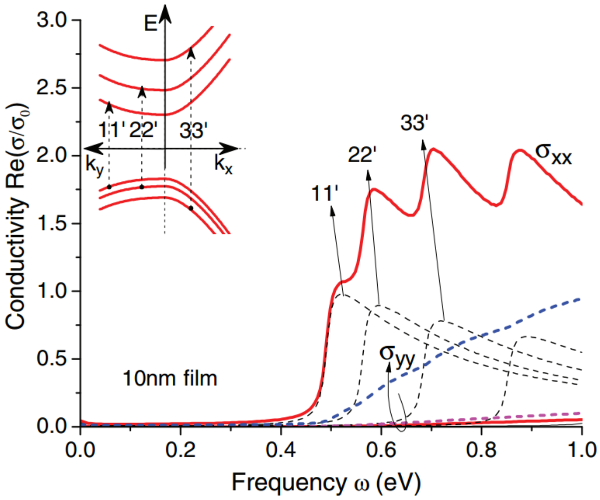

Figure 1.5: Real part of optical conductivities Re(σ_{xx}) and Re(σ_{yy}) for 10-nm-thick intrinsic BP, i.e., Fermi level is located at midgap. Figure taken from Ref. [50].

1.2.1 Optical properties of phosphorene

Characterization of the optical properties of phosphorene, including Raman scattering and photoluminescence (PL) spectroscopy, is essential to further understand its electronic band structure, crystalline orientation, and highly anisotropic exciton dynamics. The highly anisotropic nature of phosphorene has been demonstrated through Raman and polarization photoluminescence measurements [49, 48]. It was shown that, phosphorene is a two-dimensional semiconductor with layers-dependent band gap in the near-infrared range [48]. Few-layer phosphorene flakes (Fig. 1.4) were fabricated using mechanical exfoliation techniques onto a Si/SiO$_2$ chip substrate, similar to that for graphene and MoS$_2$ [48]. The flakes were first identified by optical contrast in a microscope. Regions with different colors correspond to phosphorene flakes with different thicknesses. Fig. 1.4(a) displays the optical microscope image of a typical thin phosphorene sample on a Si/SiO$_2$ substrate. The layer number identification was confirmed by atomic force microscopy (AFM) imaging of the same sample (Fig. 1.4(b)). Thus polarized Raman spectroscopy provides a non-destructive, accurate method to determine the crystalline orientation of phosphorene. As it was mentioned, in order to prevent the few layer phosphorene from reacting with the moisture or other possible reactants from the environment, the samples were put into a microscope-compatible chamber with a slow flow of nitrogen gas. The measured Raman peaks (Fig. 1.4 (c)), at 359, 437, and 466 cm^{-1} are attributed to the A_g^1, B_{2g}, and A_g^2 phonon modes in the crystalline few-layer phosphorene flakes, which matched well with observations in bulk BP. The measured PL spectra (Fig. 1.4 (a)) in few-layer phosphorus were highly dependent on the number of layers (two to five layers). Strong PL peaks at 961, 1268, 1413, and 1558 nm were observed in two-, three-, four-, and five-layered phosphorene, respectively, which correspond to energy peaks of 1.29, 0.98, 0.88, and 0.80 eV, respectively. The measured PL peaks are attributed to the nature of excitons, which represent lower bounds on the fundamental band gap values in few-layer phosphorene, respectively.

Physical quantities observed in optical experiments can often be expressed in terms of the optical conductivity. It was shown that the optical conductivity, similarly the absorption spectra, of multilayer BP vary sensitively with thickness, doping, and light polarization, particularly for frequencies in the range from $2500-5000$ cm^{-1}, which resides in the technologically relevant mid- to near-infrared spectrum [50]. Hence, multilayer BP might offer attractive alternatives in terms of tunability, flexibility, and cost, to narrow-gap compound semiconductors for infrared-optoelectronics. Fig. 1.5 presents the calculated real part of optical conductivities of an undoped 10-nm BP thin film. Results are normalized with respect to $\sigma_0 = e^2/4\hbar$, the well-known universal conductivity of graphene [51]. The large asymmetry between σ_{xx} and σ_{yy} is immediately apparent.

1.2.2 Mechanical properties of phosphorene

Besides the electrical and optical properties, the mechanical attributes of two dimensional materials (2DMs) are of great importance as well [52, 53]. The mechanical behavior of 2D materials reveal a wealth of physics and provide valuable insights into the lattice-electron interactions in low dimensional systems. These properties have been investigated for phosphorene using first-principles calculations [54]. As a result of its puckered structure, both the Young's modulus and strain were found to be highly anisotropic and nonlinear [54, 55, 38]. The suspended strips aligned with armchair and zigzag directions allow ones to carry out systematic measurements of the anisotropic Young's modulus of few-layer BP. The average Young's moduli in armchair and zigzag directions, E_{arm} and E_{zig}, were calculated using the AFM bending

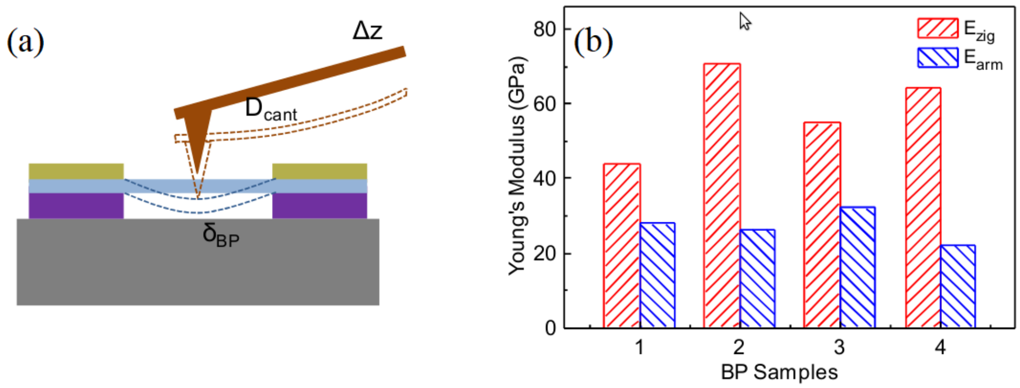

Figure 1.6: Young's modulus measurements. (a) Schematic diagram of the AFM bending measurement carried out on the suspended BP strip. (b) Young's modulus in the zigzag and the armchair directions of 4 pairs of suspended BP strips. Figure taken from Ref. [56].

method (see Fig. 1.6). It has been shown that on average E_{zig} is about 2 times larger than E_{arm} ($E_{zig} = 58.6 \pm 11.7$ GPa, $E_{arm} = 27.2 \pm 4.1$ GPa) [56].

Phosphorene has also demonstrated superior mechanical flexibility and can withstand a surface tension and tensile strain up to 10 N/m and 30%, respectively which opens doors for applications in flexible displays [55]. It was shown that a moderate -2% strain in the zigzag direction can trigger the direct-to-indirect band gap transition when axial strain is applied. In Fig. 1.7(a), five strain zones were identified based on their distinct band structure. Zone I is for a direct band gap within the strain range -12% to -10.2%, in which the CBM is represented by state C and the VBM is given by state F. Zone II corresponds to an indirect band gap from -10.2% to -2%, where the VBM is state E. Zone III is a direct gap at Γ from -2% to $+8\%$. Zone IV is an indirect gap from $+8\%$ to $+11.3\%$, where the CBM is at $\mathbf{k} = (0, 0.3, 0)$. Zone V shows a direct band gap with both the CBM and VBM at $\mathbf{k} = (0, 0.3, 0)$. The critical strains of -10.2%, -2%, $+8\%$, and $+11.3\%$ are the zone boundaries for transition from direct to indirect band gap and vis versa. Fig. 1.7(b) presents the band gap as a function of strain applied in the armchair direction. The drop of the gap value at $+12\%$ results from the fact that the CBM is replaced by the CB at X (state G). The Poisson's ratio is also a fundamental mechanical property that re-

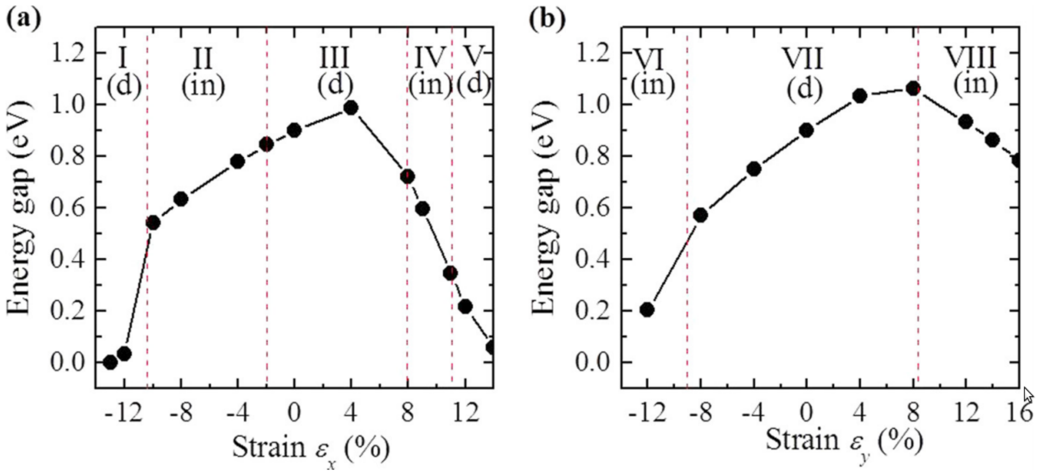

Figure 1.7: The band gap of phosphorene as a function of strain applied (a) in the zigzag and (b) in the armchair directions, respectively. Figure taken from Ref. [55].

lates the resulting lateral strain to applied axial strain. Although this value can theoretically be negative, it is positive for nearly all materials, though negative values have been observed in so-called auxetic structures. However, nearly all auxetic materials are bulk materials whose microstructure has been specifically engineered to generate a negative Poisson ratio. The existence of a negative Poisson ratio in phosphorene has been shown by using first-principles calculations [57]. In contrast to engineered bulk auxetics, this behavior is intrinsic for phosphorene, and originates from its puckered structure. This phenomena should be intrinsic to other puckered two-dimensional nanomaterials because of the fact that it functions as a nanoscale re-entrant structure, which has previously been exploited in bulk materials to induce a negative Poisson ratio.

1.3 Organization of the thesis

The thesis is organized as follows: In chapter 2, the electronic properties of phosphorene are briefly reviewed. In this chapter the necessary mathematical concepts that will be used throughout the thesis are introduced, the peculiar electronic properties of phosphorene are mentioned. As an example of an electronic phosphorene peculiarity, the anisotropic plasmon modes of a phosphorene are elaborated upon.

In chapter 3, we investigate the effect of band anisotropy on the Coulomb drag resistivity in a double-layer electron system, consisting of two individual isolated layers which are coupled via the Coulomb interaction. We start from the expression for the drag resistivity based upon the semiclassical Boltzmann transport equation in the relaxation time approximation, and develop a general formalism, which includes the effect of anisotropic energy dispersion and rotationally misaligned 2D layers. As an example we apply this formalism to calculate Coulomb drag resistivity in a double-layer phosphorene system. Our results show a strong drag resistivity dependence on the band anisotropy.

In chapter 4, we calculate the optical conductivity of an anisotropic two-dimensional system with Rashba spin-flip excitation within the Kubo formalism. We show that the anisotropic Rashba effect caused by an external field changes significantly the magnitude of the spin splitting. Furthermore, we obtain an analytical expression for the longitudinal optical conductivity associated with inter-band transitions as a function of the frequency for arbitrary polarization angle.

In chapter 5, we model a system of phosphorene on polar insulator substrates. We go beyond the assumption of independent electrons and indeed SO phonon modes and theoretically study the coupled plasmon-SO phonon interaction in monolayer and double-layer phosphorene using perturbation theory. We find that in the case of phosphorene in contrast to graphene and TMDCs, the mode coupling effect not only modifies the plasma dispersion relation but also enables us to tune the hybrid plasmon-SO phonon modes in the two crystallographic directions.

In chapter 6, the effects of an applied in-plane uniaxial strain on the plasmon dispersions of monolayer, bilayer and double-layer phosphorene structures in the long-wavelength limit within the linear elasticity theory are studied. In the low energy limit, these effects can be modeled through the change in the curvature of the anisotropic energy band along the armchair and zigzag directions. We derive analytical relations for the plasmon modes under uniaxial strain and show that the direction of the applied strain is important.

In chapter 7, we study excitonic superfluidity at zero temperature in the electron-hole double layer phosphorene system by using an anisotropic effective mass in the free-electron model. Highly anisotropic superfluidity is predicted where the magnitude of the gap function is not only momentum dependent, but also depends on the direction of the wavevector $\mathbf{k}$.

We study the possibility of an inhomogeneous charge density wave phase in a system of two electron and hole phosphorene monolayers separated by h-BN insulating layers in chapter 8. Our results show that the negative compressibility in phosphorene enables the formation of a charge density wave through the application of an uniform force field.
Finally, we conclude the thesis in chapter 9 and present an outlook for future studies.

Chapter 2

Electronic properties of phosphorene

How do the electronic properties
of black phosphorene behave?

In this chapter the electronic properties of phosphorene are reviewed. First the energy band spectrum of the charge carriers in phosphorene is derived from **k.p** theory. It is shown that the conduction and valence bands have peculiar energy band near the Γ point for the Brillouin zone. Around this point all the interesting physics happens because here the CBM and VBM are situated and the carriers have an anisotropic dispersion. This chapter briefly reviews the theoretical concepts that are common to phosphorene electronics and here we mainly introduce the readers that are unfamiliar with phosphorene physics. Secondly, it also determines the notation for the succeeding chapters.

2.1 Low-energy Hamiltonian of BP

BP has an orthorhombic crystal structure consisting of puckered layers. The lattice constant in the out-of-plane direction is about 10.7 $\mathring{A}$, and the effective layer-to-layer distance is half of this value [58]. In monolayer BP, translational symmetry in the z direction is broken, and its band structure has a direct energy gap at the Γ point instead of the Z point in the bulk case. Having obtained the band structure using ab initio calculations, a simplified model was constructed that describes the bands around the Γ point. Based on **k.p** theory and symmetry arguments, the in-plane electron dispersion around the Γ point can be described by the following low-energy Hamiltonian. In this case, the perturbing Hamiltonian is given by [59]

$$H_1 = \frac{\hbar(k_x \hat{p_x} + k_y \hat{p_y})}{m_0}, \tag{2.1}$$

where m_0 is the free electron mass. The true eigenstates of the system at the Γ point are either even or odd with respect to σ_h reflection (a symbol for horizontal mirror planes) and can written as a sum over irreducible representations of the C_{2h} point group

$$|\psi_i^e\rangle = |A_i^g\rangle + |B_i^u\rangle\,,\; |\psi_i^0\rangle = |A_i^u\rangle + |B_i^g\rangle\,, \tag{2.2}$$

where $A_{u/g}$ and $B_{u/g}$ are the irreducible representations. Using the symmetry argument, we show how the different bands mix through the perturbing Hamiltonian by rewriting the matrix element $\langle\psi_i^s|\,\hat{p}_{x/y}\,|\psi_j^{s'}\rangle$ as

$$\langle\psi_i^s|\sigma_h^\dagger\sigma_h\hat{p}_{x/y}\sigma_h^\dagger\sigma_h|\psi_j^{s'}\rangle = \pm ss'\,\langle\psi_i^s|\,\hat{p}_{x/y}\,|\psi_j^{s'}\rangle\,, \tag{2.3}$$

where $s, s' = \pm$ are the σ_h symmetry indices. This result tells us that the matrix element for $p^x(p^y)$ is nonzero only if the states have the same (different) σ_h symmetry. According to the first principles calculations, the valence and the conduction bands are even in σ_h. Thus, to the lowest order, the effective low-energy Hamiltonian is

$$\hat{H}_\mathbf{0} = \begin{pmatrix} E_c & \gamma_1 k_x \\ \gamma_1^* k_x & E_v \end{pmatrix}, \tag{2.4}$$

where $\gamma_1 = \hbar\,\langle\psi_c|\,\hat{p}_{x/y}\,|\psi_v\rangle\,/m_0$. Note that without including the rest of the bands, Eq. (2.4) describes a 1D system. The lack of y-dependence agrees with the weak dispersion in the y-direction close to the Γ point seen in the numerical results. The rest of the H_{eff} is obtained by including the remaining bands and using the Löwdin partitioning [60]. The leading order correction to the effective Hamiltonian is given by

$$(H_{\text{corr}})_{mm'} = \sum_l \frac{(H_1)_{lm}(H_1)_{lm'}}{2}\left[\frac{1}{E_m - E_l} + \frac{1}{E_m' - E_l}\right], \tag{2.5}$$

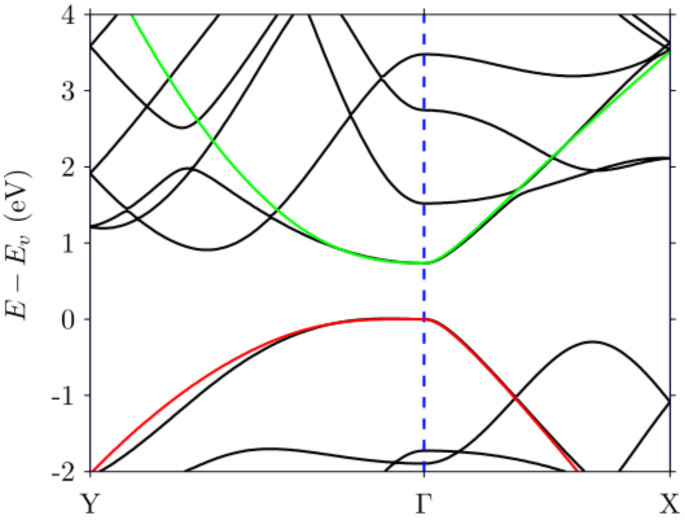

Figure 2.1: Fitting of the H$_{eff}$ results to the ab initio band structure. Figure taken from Ref. [59].

where the summation goes over the remaining bands. The diagonal elements of the correction are

$$(H_{\text{corr}})_{mm'} = \sum_{l} \frac{(\gamma^x_{ml})^2 (k_x)^2 + (\gamma^y_{ml})^2 (k_y)^2}{E_m - E_l} = \eta_m k_x^2 + \nu_m k_y^2. \tag{2.6}$$

This result captures the mass difference between the conduction and the valence bands as well as the $\hat{x}$ and $\hat{y}$ directions where x and y stand for the armchair and zigzag directions, respectively. Finally, the off-diagonal elements are

$$\begin{aligned} (H_{\text{corr}})_{cv} &= \alpha k_x^2 + \beta k_y^2, \\ \alpha &= \sum_{l,even,\sigma_h} \frac{\gamma^x_{cl}\gamma^x_{vl}}{2} [\frac{1}{E_c - E_l} + \frac{1}{E_v - E_l}], \\ \beta &= \sum_{l,odd,\sigma_h} \frac{\gamma^y_{cl}\gamma^y_{vl}}{2} [\frac{1}{E_c - E_l} + \frac{1}{E_v - E_l}]. \end{aligned} \tag{2.7}$$

Then, the corresponding Hamiltonian of BP near the Γ point can be expressed as

$$\hat{H}_{\mathbf{0}} = \left(\begin{array}{cc} E_c + \eta_c k_x^2 + \alpha_c k_y^2 & \gamma k_x + \beta k_y^2 \\ \gamma k_x + \beta k_y^2 & E_v - \eta_v k_x^2 - \alpha_v k_y^2 \end{array} \right), \tag{2.8}$$

E$_c$ (E$_v$) is the energy of conduction (valence) band edge, γ and β describes the effective coupling between the conduction and valence bands. $\eta_{c,v}$ and $\alpha_{c,v}$ are related to the known anisotropic effective masses of phosphorene [59].

$$\begin{aligned} m_e^x &= \frac{\hbar^2}{2(\eta_c + \gamma^2/2\Delta)}, \\ m_h^x &= \frac{\hbar^2}{2(\eta_v - \gamma^2/2\Delta)}, \\ m_{e(h)}^y &= \frac{\hbar^2}{2\alpha_{c(v)}}, \end{aligned} \tag{2.9}$$

where Δ is the energy band gap. One can then use these masses to obtain an approximation for the spectrum [44, 61]

$$\xi^i(\boldsymbol{k}) = \frac{\hbar^2}{2}\left(\frac{k_x^2}{m_x^{e(h)}} + \frac{k_y^2}{m_y^{e(h)}}\right) - \mu^{e(h)}, \tag{2.10}$$

where $m_x^{e/h}$ and $m_y^{e/h}$ are the electron/hole effective masses along zigzag and armchair direction in each layer. Close to the Γ point, only the leading coupling terms have been retained. A fit for the conduction and valence bands is shown in Fig. 2.1. For this fit, γ_1= 6.85 w/π eVm, η_v= -3 w$^2/\pi^2$ eVm^2, α_c= 3w$^2/\pi^2$ eVm^2, and β = 7 w$^2/\pi^2$ eVm^2, where w= 2.23$\times10^{-10}$m and π/w is the BZ width in the x direction. The rest of the parameters are set to zero. Note that this fit gives a direct band gap.

2.2 Anisotropic polarization function

A simple framework to include electron-electron interactions is called the random phase approximation (RPA) that was originally introduced by Gell-Mann and Bruckner and Bohm and Pines [62] in two seemingly different ways. For an electron gas system, the non-interacting temperature dependent polarization function can be obtained from the following equation [62]

$$\Pi_i(\mathbf{q},\omega) = -\frac{g_s}{\nu}\sum_{\mathbf{k}} \frac{f^0(E^i_{\mathbf{k}}) - f^0(E^i_{\mathbf{k+q}})}{E^i_{\mathbf{k}} - E^i_{\mathbf{k+q}} + \hbar\omega + i\eta}. \tag{2.11}$$

Here $f^0(E^i_{\mathbf{q}})$ is the Fermi distribution function in layer i at energy E corresponding to the wave vector $\mathbf{q}$, $g_s = 2$ is spin degeneracy and η is the broadening parameter, which accounts for disorder in the system. The temperature-dependent dynamic polarization function for intra-band transition in an anisotropic 2D material can be calculated by making use of the following anisotropic parabolic energy dispersion relation

$$E^i_{\mathbf{k}} = \frac{\hbar^2}{2}(\frac{k_x^2}{m_x} + \frac{k_y^2}{m_y}) - \mu_i, \tag{2.12}$$

in Eq.(2.11) for the polarization function

$$\frac{\Pi_i(\mathbf{q},\omega)}{g_{2d}} = -\int dK \frac{\Phi_i(K,T)}{Q}\left[sgn(\Re(Z_-))\frac{1}{\sqrt{Z_-^2 - K^2}} - sgn(\Re(Z_+))\frac{1}{\sqrt{Z_+^2 - K^2}}\right]. \tag{2.13}$$

In the above symmetric form of temperature-dependent anisotropic polarization function, we define $\mathbf{Q} = \sqrt{m_d/\hat{M}}(\mathbf{q}/k_F)$, $\mathbf{K} = \sqrt{m_d/\hat{M}}(\mathbf{k}/k_F)$ where $\hat{M}$ is the mass tensor with diagonal element m_x and m_y along x and y direction, and $m_d = \sqrt{m_x m_y}$ is the 2D density of state mass. Moreover, $g_{2d} = m_d/\pi\hbar^2$ and $Z_\pm = ((\hbar\omega + i\eta)/\hbar Q\nu_F) \pm (Q/2)$ with $\nu_F = \hbar k_F/m_d$ and $\Phi_i(K,T)$ is given by

$$\Phi_i(K,T) = \frac{K}{1 + \exp[(K^2 E^i_F - \mu_i)/k_B T]}, \tag{2.14}$$

where μ_i is the chemical potential of layer i, which is determined by the particle number conservation condition [63]

$$\mu_i + k_B T \ln[1 + \exp(-\mu_i/k_B T)] = E^i_F. \tag{2.15}$$

Here, we consider $\mathbf{q} = q(\cos\theta, \sin\theta)$, in accordance to the notation in Ref. [46], to introduce rotational parameter for the layers. Rotational angle, τ_i, is defined as the angle between x-axis in the laboratory frame and x direction

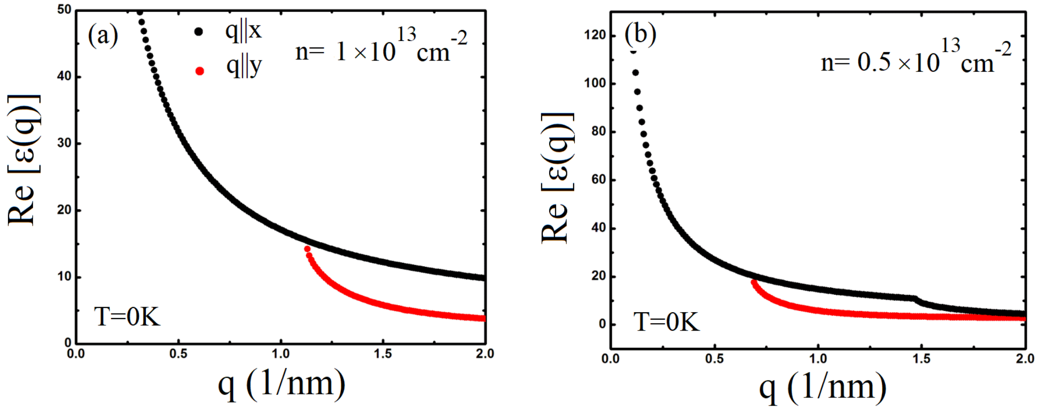

Figure 2.2: Static dielectric function in the RPA for monolayer phosphorene along the armchair and zigzag direction for (a) $n = 1 \times 10^{13}\text{cm}^{-2}$ and (b) $n = 0.5 \times 10^{13}\text{cm}^{-2}$ for T=0K.

of the ith layer. So, we can write $Q = q\sqrt{m_d R_i}/k_F$ in which the orientation factor, R_i , is expressed as

$$R_i = \left(\frac{\cos^2(\theta - \tau_i)}{m_x} + \frac{\sin^2(\theta - \tau_i)}{m_y}\right). \tag{2.16}$$

In case of phosphorene, we have $m_x \approx 0.15 m_0$ and $m_y \approx 0.7 m_0$ [64].

2.3 Screening potential

The dynamically screened inter-layer potential can be obtained by solving the corresponding Dyson equation [65]

$$U_{ij}(\mathbf{q}, \omega) = \frac{V_{ij}(q)}{det|\epsilon_{ij}(\mathbf{q}, \omega)|}, \tag{2.17}$$

where $V_{ij}(q) = \nu(q)\exp(-qd(1 - \delta_{ij}))$ is the unscreened 2D Coulomb interaction with d being the layer spacing. $\nu(q) = 2\pi e^2/q\kappa$, with κ being the average dielectric constant. Finally $\epsilon_{ij}(\mathbf{q}, \omega)$ is the dynamic dielectric matrix of the system. For systems with high electron density it is reasonable to employ the RPA to calculate $\epsilon_{ij}(\mathbf{q}, \omega)$ [66]

$$\epsilon_{ij}(\mathbf{q}, \omega) = \delta_{ij} + V_{ij}(q)\Pi_i(\mathbf{q}, \omega). \tag{2.18}$$

At low electron densities, the short-range local field effects are not negligible and must be included in the dielectric matrix by replacing $(1 - G_{ij}(q))V_{ij}(q)$ for, $V_{ij}(q)$ where $G_{ij}(q)$ denotes the static intra- $(i = j\ )$ and inter-layer $(i \neq j\ )$ elements of LFC matrix, respectively. Here we incorporate only the intra-layer components of the local field correction (LFC) factor because of their stronger effect on the drag resistivity [67]

$$G_{ii}(q) = \frac{q}{2\sqrt{q^2 + k_F^2}}, \tag{2.19}$$

where $G(q)$ and $k_F = \sqrt{2\pi n}$ is the Hubbard LFC factor and the Fermi wave vector, respectively, with n being the electron density.

Fig. 2.2 shows the static dielectric function of monolayer BP along zigzag $q||y$ and armchair $q||x$ direction of phosphorene for different densities. $\Pi(\mathbf{q})$ has a kink at $q = 2|\boldsymbol{k}_F.\hat{\boldsymbol{q}}|$. One can see how the kink migrates with changing doping. With increasing temperature and disorder, the kink is smoothed out as illustrated in Fig. 2.3. The otherwise isotropic screening at small momenta now becomes anisotropic.

2.4 Plasmon modes in phosphorene

There is one particular type of excitation which is immensely important, namely the plasmon excitation. This excitation can be measured by, for example, inelastic light scattering (Raman scattering), where the change of momentum and energy of an incoming photon is measured. Plasmons are collective density oscillations that arise due to the electron-electron interaction. They exist in many metals and semiconductors. While the electron-hole pair excitations are the only possible source of dissipation of plasmons in the non-interacting electron gas, this is certainly not true for the interacting case which is more complicated.

In order to find plasmons in a quantum mechanical framework, one needs to include electron-electron interactions. If one calculates the density-density response function including interactions, plasmons will appear as its poles. The plasma frequency is an important parameter of the interacting electron gas setting the energy scale for several processes, *e.g.* it marks the limit below which metals reflect incoming electromagnetic radiation, and above which they become transparent. A very direct manifestation of the plasmon frequency is the existence of the collective charge density oscillations, the

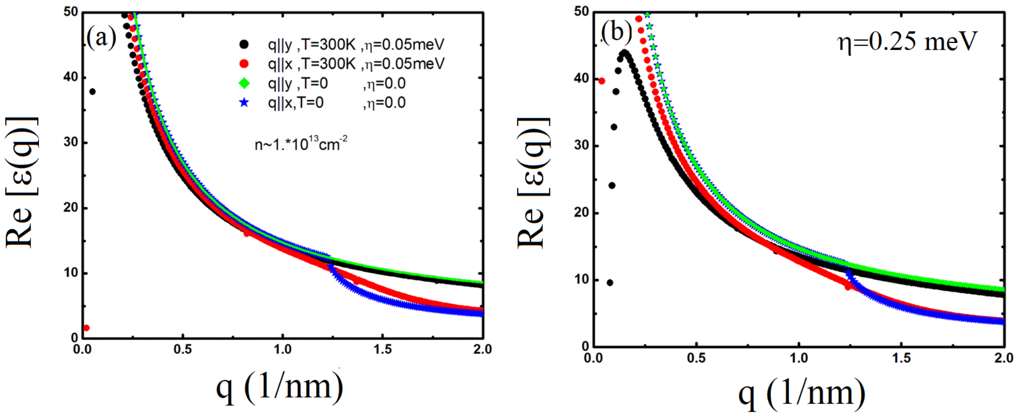

Figure 2.3: Dynamic dielectric function in the RPA for monolayer phosphorene along the armchair and zigzag direction for two broadening parameterη.

plasma oscillations. From a classical point of view, one can think of plasmons as the response of an interacting electron liquid to an external electric field that causes a disturbance in the density. These oscillations are obtained as follows. Consider the relation $\phi_{ext}(q,\omega) = \epsilon(q,\omega)\phi_{tot}(q,\omega)$. Note that $\epsilon(q,\omega) = 0$ in fact allows for a situation where the total potential varies in space and time in the absence of any external potential driving these variations.

The plasmons have infinite lifetime for small q. However, at some point the dispersion curve crosses into the dissipative $\Im\Pi(q,\omega) = 0$ area, and there the plasmon acquires a finite lifetime. In other words for high q-values the plasmonic excitations are not exact eigenmodes of the system, and they are damped out as a function of time. In the literature this damping mechanism is denoted Landau damping. This occur when the plasmon enters the SP phase space, whose boundaries are given by $\hbar\omega_{pl}^{\pm} = E(\pm k_F + q) - E(k_F)$.

2.5 The polarization function in the long-wavelength limit

The dynamic polarization function given by Eq. (2.13) has the following expression in the long-wavelength limit at zero-temperature:

$$\frac{\Pi(\omega,q,\theta)}{g_{2d}}=\frac{1}{2}\Big[-2+\sqrt{(1-\frac{2\omega}{k_F\nu_F Q^2})^2-\frac{4}{Q^2}}+\sqrt{(1+\frac{2\omega}{k_F\nu_F Q^2})^2-\frac{4}{Q^2}}\quad\Big],\tag{2.20}$$

One can rewrite Eq. (2.20) as:

$$\frac{\Pi(\omega,q,\theta)}{g_{2d}}=\frac{1}{2}\Big[-2+(1-\frac{2\omega}{k_F\nu_F Q^2})\big(1-\frac{2/Q^2}{(1-\frac{2\omega}{k_F\nu_F Q^2})^2}\big)(1+\frac{2\omega}{k_F\nu_F Q^2})\big(1-\frac{2/Q^2}{(1+\frac{2\omega}{k_F\nu_F Q^2})^2}\big)\Big],\tag{2.21}$$

from which we find the long wavelength approximation

$$\frac{\Pi(\omega,q\to0,\theta)}{g_{2d}}\approx\frac{-2}{Q^2}\bigg(\frac{1}{1-\frac{4\omega^2}{(k_F\nu_F Q^2)^2}}\bigg).\tag{2.22}$$

Finally, by ignoring unity in the denominator and making use of $Q_i(\theta)=q\sqrt{m_d R_i(\theta)}/k_F$ and $E_F=\hbar^2k_F^2/2m_d$, one obtains Eq. (3.5). The polarization function in the limit of low energy and long-wavelength can be written as:

$$\Pi(q\to0,\omega)=\frac{R_i(\theta)nq^2}{\omega^2}.\tag{2.23}$$

So, we can derive the plasmon dispersion for monolayer BP in the long wave length limit as

$$\begin{aligned}\epsilon(q\to0,\omega)&=1-\frac{2\pi e^2}{q\kappa}\frac{R_i(\theta)nq^2}{\omega^2}=0\\ \omega_{pl}(q)&=\frac{2\pi ne^2R_i(\theta)q}{\kappa},\end{aligned}\tag{2.24}$$

which results into

$$\omega_{pl}(q)=\frac{2\pi ne^2R_i(\theta)q}{\kappa},\tag{2.25}$$

where κ is the dielectric constant.

As it is well known, electronic collective modes of a double-layer system are obtained from zeros of the dielectric function determinant, Eq.(2.18). In the presence of intra-band single particle excitations, there are two plasmon modes. In order to determine the dispersion relation of the coupled modes, we need to calculate the zeros of determinant of the total dielectric matrix (Eq. (5.6)) in the long-wavelength limit

$$\begin{aligned}\epsilon(\omega, q \to 0, \theta) = 1 &- (R_1(\theta) + R_2(\theta))\Pi'(q \to 0, \omega)\nu(q) \\ &+ \nu(q)\Pi'(q \to 0, \omega))^2 R_1(\theta)R_2(\theta)(1 - e^{-2qd})\end{aligned} \tag{2.26}$$

where $\Pi'(\omega, q, \theta) = \Pi_i(\omega, q, \theta)/R_i(\theta)$.

In the long-wave length limit, we can write $(1 - e^{-2qd}) \approxeq 2qd$. As we have mentioned, for getting the plasmonic branches we should have the zero of dielectric function as

$$1 - \big(R_1(\theta) + R_2(\theta)\big)\Pi'(q \to 0, \omega)\nu(q) + \nu(q)\Pi'(q \to 0, \omega))^2 R_1(\theta)R_2(\theta)2qd = 0 \tag{2.27}$$

By doing some algebra, we get the following relation:

$$\nu(q)^2(2qd)R_1(\theta)R_2(\theta)[\Pi'(\omega, q, \theta) - \Pi_+(q \to 0, \theta)][\Pi'(\omega, q \to 0, \theta) - \Pi_-(q \to 0, \theta)] = 0 \tag{2.28}$$

where Π_+ and Π_- defined as

$$\Pi_+(\omega, q, \theta) = \frac{R_1(\theta) + R_2(\theta)}{(R_1(\theta)R_2(\theta)\nu(q)2qd} \tag{2.29}$$

and

$$\Pi_-(\omega, q, \theta) = \frac{1}{(R_1(\theta) + R_2(\theta))\nu(q)} \tag{2.30}$$

The dispersion relation of the couple modes is given by $\Pi'(\omega, q \to 0, \theta) = \Pi_\pm(\omega, q \to 0, \theta)$. In the leading-$q$ approximation (long-wavelength limit), two plasmonic branches are obtained through the following relations [46]:

$$\omega_{ac}(q, \theta) = 2q\sqrt{\frac{n\pi e^2 d_{12}}{\epsilon_\infty}\frac{R_1(\theta)R_2(\theta)}{R_1(\theta) + R_2(\theta)}}\ . \tag{2.31}$$

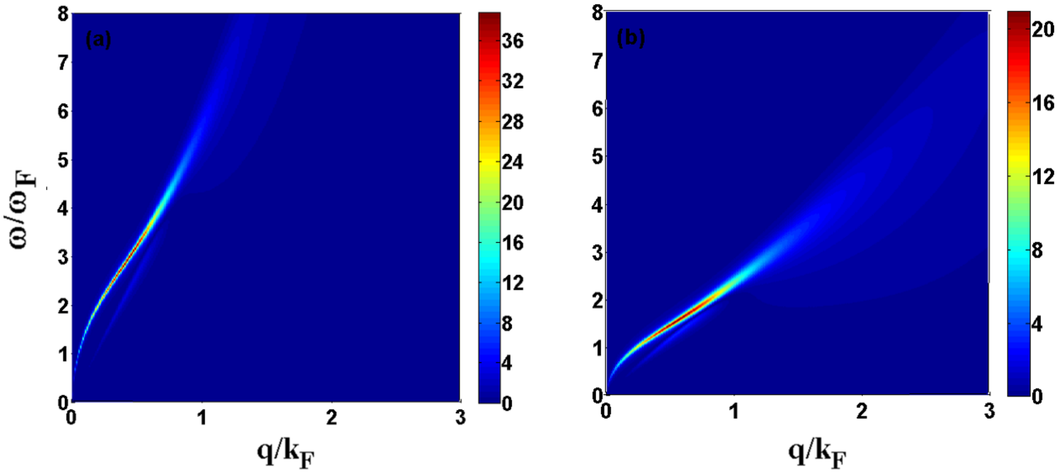

Figure 2.4: (Color online) Loss function, $|\Im(1/\det\epsilon(\mathbf{q},\omega,T)|$, for two crystallographic directions (a) $\theta=0$ and (b) $\theta=\pi/2$ at T=100 K with d =5 nm , $n=3\times10^{12}\mathrm{cm}^{-2}$ and η =1 meV.

$$\omega_{op}(q,\theta)=\sqrt{\frac{2n\pi e^2 q}{\epsilon_\infty}\big(R_1(\theta)+R_2(\theta)\big)}\ . \tag{2.32}$$

Finally, one obtains the so-called acoustic and optical modes, which show linear $\omega_{ac}(q)\sim\sqrt{(R_1R_2/(R_1+R_2)dq}$ and square-root $\omega_{op}\sim\sqrt{(R_1+R_2)q}$ behavior at small wave vectors, respectively, and dependence on the orientation factors R_1 and R_2 (see Eq.(2.16)) for phosphorene [46].

To make the above discussion clearer, we show the loss function of a system comprising two parallel monolayer phosphorene separated by $d=5$ nm at T= 100 K for two main crystallographic directions: $\theta=0$ and $\theta=\pi/2$, in Fig.2.4, respectively. One may notice that the acoustic plasmon mode calculated here are weaker than the optical one. This can be explained by the fact that the coherence of the acoustic mode is significantly affected by thermal fluctuations and disorder, η, broadening because the ω-q spectrum of this mode is very close to the single particle excitation region. Our numerical results for the loss function at small q is in good agreement with the loss function for bilayer black phosphorus in Ref. [45] where the two modes have been obtained by using a general tight-binding model. Additionally, it can be recognized that the lower-energy acoustic plasmon and higher-energy optical plasmon modes follow a different asymptotic behavior at small wave vectors in both panels of Fig. 2.4. Due to the anisotropic band structure, the long-lived plasmon modes disperse differently in such a way that the larger the effective mass along y leads to smaller resonance frequencies [46, 44]. As we know at low temperature, the carriers do not have enough energy to be exited above the Fermi surface but on the contrary at T near the Fermi temperature there is sufficient energy to excite carriers thermally.

As we mentioned earlier, the RPA is reliable for systems with high electron densities. The density parameter $r_s = \sqrt{2}/(k_F a_B^*)$ with effective Bohr radius $a_B^* = \kappa/(e^2 m_d)$, which is defined as the average distance between electrons in a non-interacting 2D electron gas, gives a measure for reliability of the RPA. In Fig. 2.4, we consider the same electron density in the both layers, $n_1 = n_2 = 3 \times 10^{12}\text{cm}^{-2}$, the substrate and spacer to be low with $\kappa \approx 12$ that leads to an $r_s \approx 1.7$ for which RPA predicts the qualitatively well electronic behavior. However, Hubbard LFC can improve the result of the calculations by including the exchange hole around the interacting electrons. As mentioned, the acoustic mode depends the finite separation between the layers, d. Due to the anisotropic band structure and electron-hole continuum of the system, long lived plasmons can disperse differently in phosphorene. Furthermore, different parameters are effective on the behavior of anisotropic double layer system such as the relative rotation angle, the relative chemical potential, as well as the separation between the layers.

2.6 Experimental observation of plasmons

From an experimental viewpoint, momentum resolved electron energy loss spectroscopy (EELS) [68] directly probes the loss function of a material, which in turn is simply the inverse of the imaginary part of the dynamical interacting dielectric constant of a material: $E_{Loss}(q,\omega) = -\big[1/\Im\epsilon(q,\omega)\big]$. It has been used extensively in a variety of materials such as graphene [69, 70] TMDs [71], and bulk BP [72], in order to explore the single particle and collective excitations such as excitons and plasmons. The energy and momentum resolved optical response of BP in its bulk form has been investigated by employing EELS in transmission [72]. Along the armchair direction of the puckered layers, a highly dispersive mode was found that is strongly suppressed in the zig-zag (zz) direction. This mode emerges out of the single-particle continuum for finite values of the momentum and is therefore interpreted as

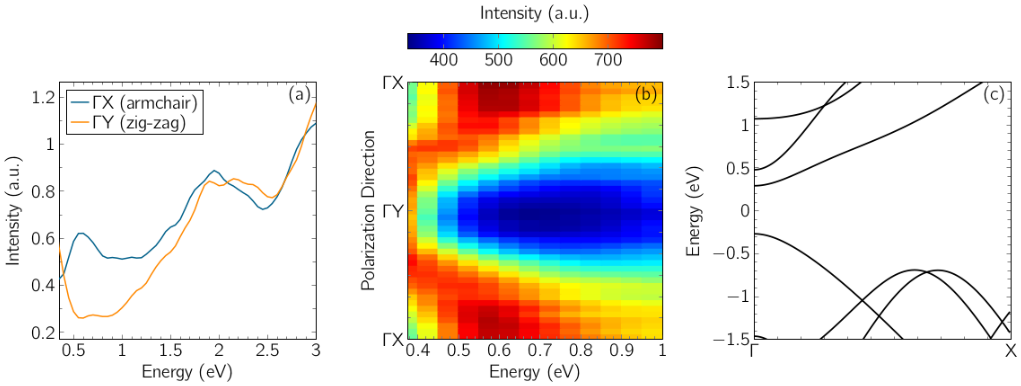

Figure 2.5: (a) EELS intensity along the two high-symmetry directions within the puckered layers of BP. (b) Low-energy polarization-map showing the smooth angular dependence of the EELS intensity within the puckered layers of BP. (c) Calculated single-particle band structure along ΓX. Figure taken from Ref. 2.5.

an exciton. Consequently, the behavior of the measured EELS intensity is shown in Fig. 2.5 where we see an angular dependent reduction of spectral weight when changing the polarization from ΓX (ar) to ΓY (zz)-direction. From Fig. 2.5, it is clear that this translates directly to a strongly anisotropic EELS response. A low-energy mode was found along the ΓX that resides at about $E = 0.6\ eV$. When changing the polarization direction from ΓX to ΓY within the puckered layers, this mode gradually shifts to lower energy and looses strength as can be seen from Fig. 2.5(b).

Chapter 3

Coulomb drag

“ How the drag effect in BP is affected by the anisotropy band structure?”

In this chapter [1], we theoretically study the Coulomb drag resistivity in a double-layer electron system with highly anisotropic parabolic band structure using Boltzmann transport theory. As an example, we consider a double-layer phosphorene on which we apply our formalism. This approach, in principle, can be used for other double-layered systems with paraboloidal band structures. Our calculations show that the rotation of one layer with respect to another layer is able to control the drag resistivity in such systems. As a result of the rotation, the off-diagonal elements of the drag resistivity tensor have non-zero values at any temperature. In addition, we show that the anisotropic drag resistivity is very sensitive to the direction of the momentum transfer between the two layers due to highly anisotropic inter-layer electron-electron interaction. Also the plasmon modes depend on the relative direction of the two layers and temperature. In particular, the drag anisotropy ratio, ρ_{yy}/ρ_{xx}, can reach up to ≈ 3 by changing the temperature. Furthermore, our calculations suggest that including the local field correction in the dielectric function changes the results significantly. Finally,

---

[1] The results of this chapter were published in Journal of Physics: Condensed Matter, 28 (28), 285301 [47]

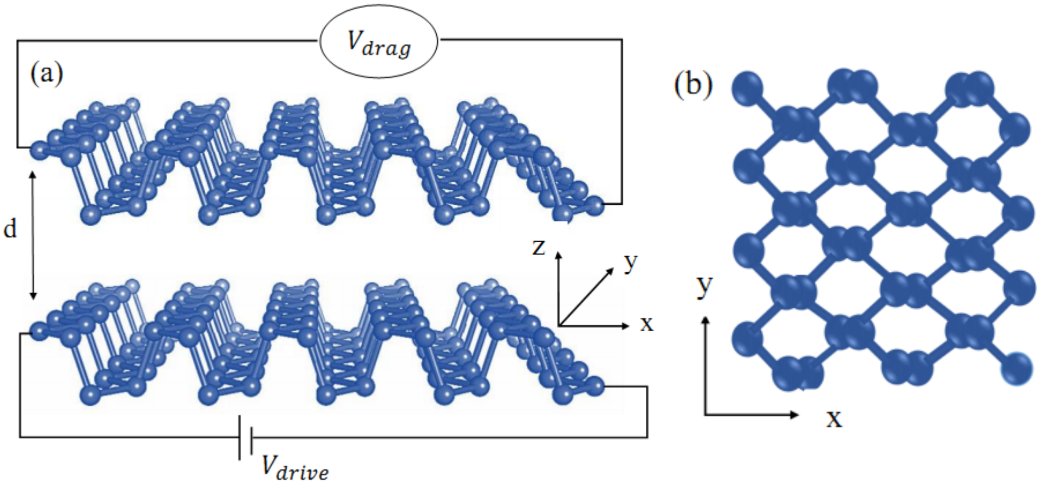

Figure 3.1: (a) Side view of a double-layer phosphorene system with the separation of d in the drag setup. (b) Top view of phosphorene.

we examine the dependence of drag resistivity and its anisotropy ratio on various parameters like inter-layer separation, electron density, short-range interaction and insulating substrate/spacer.

3.1 Introduction

Double-layered 2D structures consisting of two parallel electron or hole systems which are kept in close vicinity demand special attention due to many-body effects [73, 74, 75]. The inter-layer Coulomb interaction plays a significant role in these correlated systems. In Coulomb drag phenomenon, momentum can be transferred from interacting electrons in one layer to electrons in the adjacent layer [76, 77, 78]. The momentum transfer takes place through inter-layer Coulomb interaction, but does not involve any carrier exchanges due to the inserting materials between the two phosphorene layers. This phenomenon has been previously studied in different nanostructures such as double quantum wells (DQW) [79, 80, 81, 82, 83].

Van der Waals bonding of 2D heterostructures makes it possible to spatially separate two layers of graphene (or any other 2D materials) down to a few nano-meter, by inserting a few atomic layers of a 2D insulator, for instance h-BN to isolate the layers from one another. As shown by Gorbachev

[1], a double-layer graphene system has a strong Coulomb drag resistivity with respect to GaAlAs heterostructures [84, 85]. Likewise, phosphorene is a 2D material, however, with highly anisotropic energy dispersion in contrast to graphene and other 2D materials. Therefore, it is particularly worthwhile to examine the effect of anisotropy on the Coulomb drag [86].

In this chapter we investigate the effect of band anisotropy on the Coulomb drag resistivity in a double-layer electron system, consisting of two individual isolated layers which are coupled via Coulomb interaction. We start from the expression for the drag resistivity based upon the semi-classical Boltzmann transport equation within the relaxation time approximation, and develop a general formalism, which includes the effect of anisotropic energy dispersion and rotationally misalignment. As an example we apply this formalism to calculate the Coulomb drag resistivity in a double-layer phosphorene system, see Fig. 3.1. Numerical results show a strong dependence of the drag resistivity on the band anisotropy. It indicates that the drag resistivity along the bigger mass, i.e., m_y, has a larger value. Furthermore, we discuss how the drag resistivity and its anisotropy ratio depend on the carrier density, inter-layer separation, rotation of layers and the choice of insulating substrate/spacer. The drag resistivity is enhanced substantially in the y direction when adding the Hubbard local field correction (LFC) to our formalism. Note that the LFC includes the short-range exchange effect between electrons in the same the layer.

3.2 Coulomb drag resistivity in 2D anisotropic systems

3.2.1 Model

We consider a system composed of two parallel spatially separated 2D electron gases with anisotropic parabolic-like band structures. In this system the carriers are coupled through Coulomb interaction and there is no tunneling between layers so the Fermi energies and chemical potentials can be considered independently. The inter-layer Coulomb interaction can cause momentum transfer from the electrons in the drive layer, layer 1, to the carriers in the drag layer, layer 2. In doing so it generates a potential difference across the layers. In Fig. 3.1(a) we show a schematic of the drag setup with phosphorene layers as anisotropic 2D electron gases. Also, a top view of the phosphorene monolayer can be seen in Fig. 3.1(b).

The drag (inter-layer) resistivity, ρ, can be defined as [87]

$$\sum_{\alpha=x,y} \rho_{21}^{\alpha\beta} J_{1,\alpha} = \Xi_{2,\beta}, \tag{3.1}$$

where $\mathbf{J}$ and $\boldsymbol{\Xi}$ are the current density and electric field, respectively. α and β indexes label x and y components and $\rho_{21}^{\alpha\beta} = \rho_{12}^{\beta\alpha}$. The drag resistivity in the linear regime has been studied in a variety of theoretical approaches for (non)parabolic band structures, and particularly graphene by assuming intra-layer momentum (in)dependent relaxation times [88, 85]. Using different theoretical approaches such as the memory function formalism [89], Kubo formula based on the leading-order diagrammatic perturbation theory [90] and the linear response Boltzmann transport equation, the drag resistivity matrix can be obtained. We generalize the derivation of the drag resistivity tensor based on the Boltzmann equation approach to the case of anisotropic band structure with the assumption of a constant transport time and obtain (see Appendix **??**):

$$\rho_{21}^{\alpha\beta} = \frac{\hbar^2}{2\pi e^2 n_1 n_2 k_B T} \int \frac{d^2q}{(2\pi)^2} q_\alpha q_\beta \times \int_0^\infty d\omega \frac{|U_{21}(\mathbf{q},\omega)|^2 \Im\Pi_2(\mathbf{q},\omega) \Im\Pi_1(\mathbf{q},\omega)}{\sinh^2(\hbar\omega/2k_B T)}. \tag{3.2}$$

This is the same as the drag resistivity expression given for isotropic parabolic band structure systems in which q_α and q_β are the α and β components of the transferred wave vector corresponding to layer 1 and layer 2 in the laboratory frame, respectively. Here $U_{21}(\mathbf{q},\omega)$ is the temperature-dependent dynamically screened inter-layer interaction, $\Pi_i(\mathbf{q},\omega)$ and n_i being the 2D non-interacting polarization function and electronic density of ith layer, and k_B is the Boltzman constant. In Sec. 3.2.2, we will rewrite Eq. (3.2) to make it more convenient to use in a double-layer electron gas system with anisotropic band structure.

It is worth pointing out that considering a very thin double-layer phosphorene system when, at the same time, we assume there is no tunneling between the two layers, is not actually a problematic consideration because the space between layers is filled by a slim dielectric material. Al_2O_3 and h-BN have been successfully used as a substrate and spacer to make such thin heterostructures with no inter-layer tunneling [91, 92]. Throughout this chapter, we assume that the substrate is a thick layer of the same material as spacer.

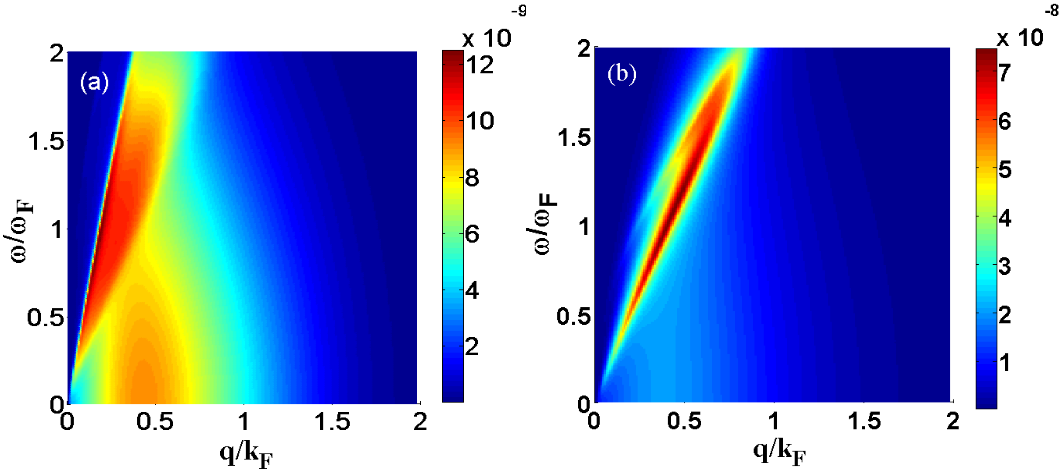

Figure 3.2: (a) $F^{xx}(q,\omega,T)$ and (b) $F^{yy}(q,\omega,T)$ for two aligned phosphorene monolayers sandwiched by $\mathrm{Al_2O_3}$ layers at T=100 K with $d=$ 5nm, $n = 3\times 10^{12}\mathrm{cm}^{-2}$ and η =1 meV .

3.2.2 Drag effect in a double-layer phosphorene

In this section, we first derive a formula for the drag resistivity of a 2D anisotropic double-layer system with parabolic band structure and then solve it by making use of numerical methods. Eq. (3.2) is the general formula for the drag resistivity based on the linearized Boltzmann transport equation. In the case of two coupled anisotropic layers, the off-diagonal components of the drag resistivity tensor may have non-zero values as a result of finite τ, unlike the isotropic systems such as double-layer graphene and conventional 2D electron gas. To make the difference more explicit, we rewrite Eq.(3.2) as follows

$$\rho_D^{\alpha\beta} = \frac{\hbar^2}{(2\pi)^3 e^2 n_1 n_2 k_B T}\int dq \int_0^\infty d\omega F^{\alpha\beta}(q,\omega,T), \tag{3.3}$$

where $\rho_D^{\alpha\beta} = \rho_{21}^{\alpha\beta}$ and $F^{\alpha\beta}(q,\omega,T)$ is defined as

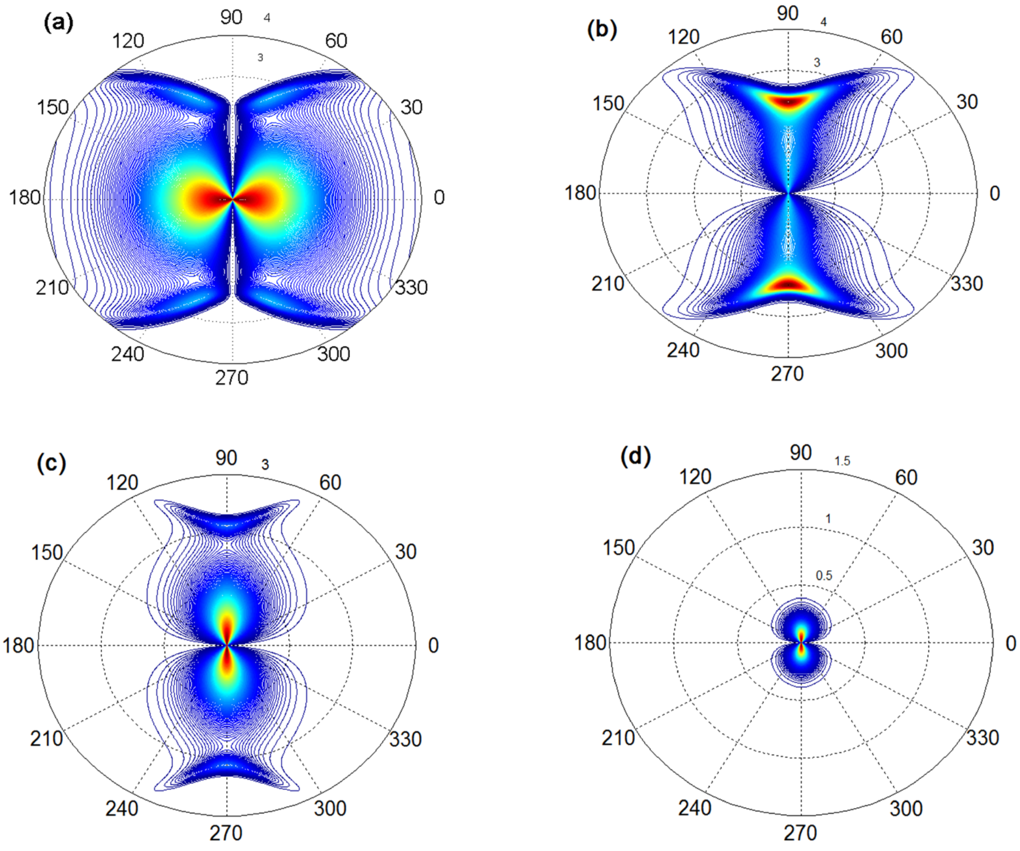

Figure 3.3: The integrand of Eq. (3.4) at $q = k_F$ for two aligned monolayers sandwiched by Al_2O_3 layers with $n = 3 \times 10^{12}$cm^{-2}, and η =1 meV, d =5 nm, along (a) x and (b) y directions at T=100 K and along y direction at (c) T= 50 K and (d) T= 10 K. The radial and azimuthal coordinates are ω/ω_F and the angular orientation of q, respectively.

$$F^{\alpha\beta}(q,\omega,T) = \int_0^{2\pi} d\theta \psi^{\alpha\beta}(\theta,\tau_1,\tau_2) \frac{q^3}{\sinh^2(\hbar\omega/2k_BT)} |U_{12}(q,\omega,T;\theta,\tau_1,\tau_2)|^2 \\ \times \Im\Pi_1(q,\omega,T;\theta,\tau_1)\Im\Pi_2(q,\omega,T;\theta,\tau_2) \tag{3.4}$$

with $\psi^{\alpha\beta}$ given by

$$\psi^{\alpha\beta}(\theta,\tau_1,\tau_2) = \begin{cases} \cos(\theta-\tau_1)\cos(\theta-\tau_2), & \alpha=\beta=x \\ \sin(\theta-\tau_1)\sin(\theta-\tau_2), & \alpha=\beta=y \\ \cos(\theta-\tau_1)\sin(\theta-\tau_2), & \alpha=x,\beta=y. \end{cases} \tag{3.5}$$

In order to understand how anisotropy affects the drag resistivity, it is worth looking into the integrand of Eq. (3.3), $F^{\alpha\beta}(q,\omega,T)$ in more depth. In Fig. 3.2, we show $F^{\alpha\beta}(q,\omega,T)$ for a coupled system composed of two aligned phosphorene monolayers separated by 5 nm at T=100 K. We use the dimensionless variables q/k_F and ω/ω_F, where $\omega_F = \hbar^{-1}E_F$. Note that the integrand has significant weight in the $0 < q < k_F$ interval, as is the case in a conventional 2D electron gas [90] but its values are larger along the y direction. This is due to the greater effective mass of electrons in y direction, which results in lower energies for the collective modes, and in this manner enhances the contributions of the plasmons [90, 79].

The angular orientation of $\mathbf{q}$ impacts the drag resistivity behavior considerably. We depict the integrand of Eq. (3.4) along $x(\alpha=\beta=x)$ in Fig. 3.3(a) and along $y(\alpha=\beta=y)$ in Fig. 3.3(b) in an aligned-layers system. At intermediate temperature T∼100 K, both modes (acoustic and optical) take part and the single particle excitation spectrum is sufficiently broadened to contribute effectively. As can be observed in the figure, the larger magnitude of the integrand occurs around $\theta = 0$ and 180° along the x direction and around $\theta = 90°$ and 270° for y direction, respectively. The integrand of Eq. (3.4) along the y direction plotted in Figs. 3.3(c) and (d) show the results for two different temperatures: (c) T=50 K and (d) T=10 K. According to this figure, at T=10 K the drag resistivity is mainly influenced by the acoustic mode which is lower in energy ($\omega < 0.5\omega_F$) and the optical mode contribution starts to appears at 50 K. Here, the radial and azimuthal coordinates denote ω/ω_F and the angular orientation of $\mathbf{q}$, respectively. The first set of calculations of the drag resistivity in a double-layer phosphorene is presented in Fig. 3.4. Here we show the diagonal and off-diagonal elements

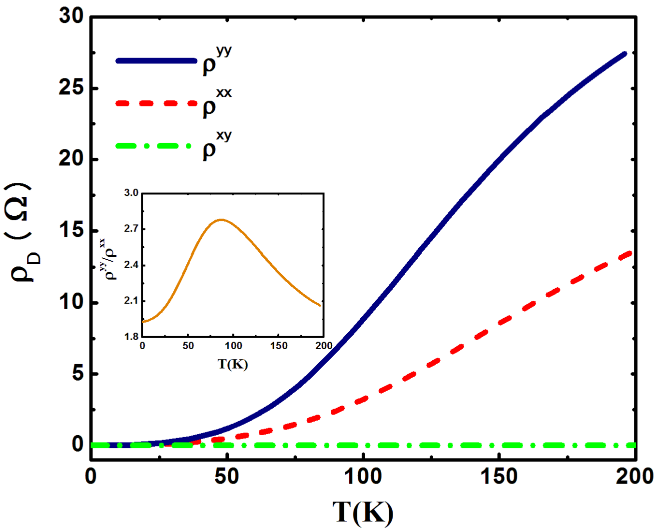

Figure 3.4: Anisotropic drag resistivity components, $\rho_D^{\alpha\beta}$ calculated within RPA as a function of temperature for two aligned phosphorene monolayers separated by an Al_2O_3 layer with $n = 3 \times 10^{12}\text{cm}^{-2}$ at η =1 meV and d =5 nm. The inset graph shows the anisotropy ratio ρ^{yy}/ρ^{xx}.

of the drag resistivity tensor calculated within the RPA, versus temperature for two parallel aligned phosphorene monolayers separated by Al_2O_3 layers of thickness d =5 nm. While the diagonal drag resistivity matrix elements increase in similar manner with temperature, there are significant differences between the values. Drag resistivity along the x direction, ρ^{xx}, is smaller than the drag resistivity along the y direction, ρ^{yy}, at any temperatures of interest with a drag anisotropy ratio (see inset graph), ρ^{yy}/ρ^{xx}, which approximately changes from 2 up to about 3. We believe that a higher-energy resonance along x direction resulting from the smaller effective mass, as discussed before, accounts for this behavior. Moreover, as expected from general symmetry arguments, the off-diagonal elements are zero.

In order to understand how rotation of one layer with respect to the other about the normal direction to the layers (z direction) impacts the behavior of the drag resistivity, we present calculations of the diagonal and off-diagonal elements of the drag resistivity matrix for a couple of rotational angles in Fig. 3.5. Here, we set $\tau_1 = 0$ and $\tau_2 = \tau$. It can be seen that as the angle of rotation increases, both diagonal elements of drag resistivity

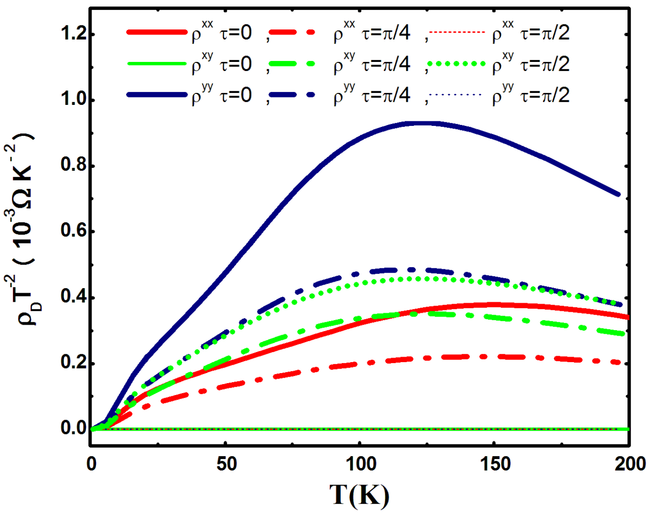

Figure 3.5: Scaled drag resistivity $\rho_D T^{-2}$ as a function of temperature for different angles with $n = 3 \times 10^{12}\text{cm}^{-2}$, and η =1 meV, d =5 nm. The phosphorene layers are sandwiched by Al_2O_3 layers.

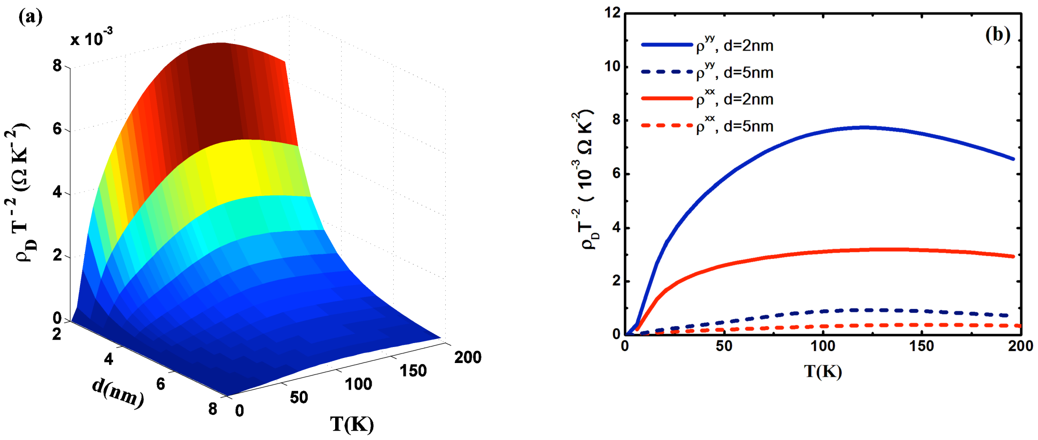

Figure 3.6: Scaled drag resistivity calculated within RPA (a) along y direction as a function of temperature and for different values of the distance between the two layers and (b) along x and y directions as a function of temperature. Here, $n = 3 \times 10^{12}\text{cm}^{-2}$ and η =1 meV and the system comprising of two aligned phosphorene monolayers sandwiched by Al_2O_3.

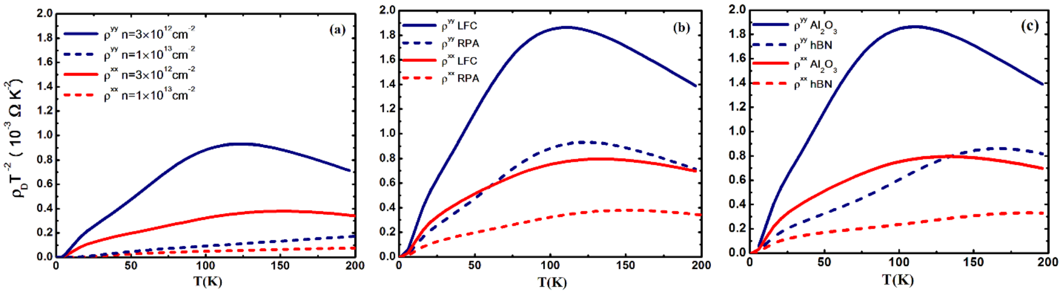

Figure 3.7: Scaled drag resistivity, $\rho_D T^{-2}$, as a function of temperature for two aligned phosphorene monolayers sandwiched by $\mathrm{Al_2O_3}$ and calculated (a) within RPA for two different electron densities $n = 3 \times 10^{12}\mathrm{cm}^{-2}$ (solid line) and $n = 1 \times 10^{13}\mathrm{cm}^{-2}$ (dashed line), (b) within RPA and Hubbard LFC at $n = 3 \times 10^{12}\mathrm{cm}^{-2}$ and (c) sandwiched by $\mathrm{Al_2O_3}$ and h-BN calculated within Hubbard LFC at $n = 3 \times 10^{12}\mathrm{cm}^{-2}$. Here we set $d = 5$ nm and $\eta = 1$ meV.

decrease considerably. This observation can be rationalized through the fact that by increasing the angle of rotation, one of the plasmonic branches is forced into the damped regime. As a result, the contribution of plasmons to the Coulomb drag phenomenon, which is known to be significant, decreases. Furthermore, our calculations show that when the layers are rotated with respect to one another the anisotropic effects can create an interesting non-zero transversal drag resistivity, ρ^{xy}, which is absent in isotropic materials at zero magnetic field. This observation can be fully understood by Eq. (3.3-3.5) in which a misalignment of the laboratory and the layer axes gives rise to a non-zero value for the off-diagonal elements. This effect, however, may exist in double-layer structures subjected to a perpendicularly applied magnetic field [93, 1]. Another interesting geometrical effect in a double-layer phosphorene structure comes from changing the inter-layer distance, which is presented in Fig. 3.6(a) is a 3D plot showing the variation of $\rho^{yy}T^{-2}$ as a function of layer spacing and temperature. It can be observed that the peaks occur at intermediate temperatures where the plasmon contribution to the drag resistivity is significant, over the whole range of inter-layer distances. Also the scaled drag resistivity decreases strongly when increasing the separation between the two layers at all temperatures. One can attribute this behavior to the inter-layer interaction, which decays exponentially with increasing distance between the layers, and decreases due to acoustic modes

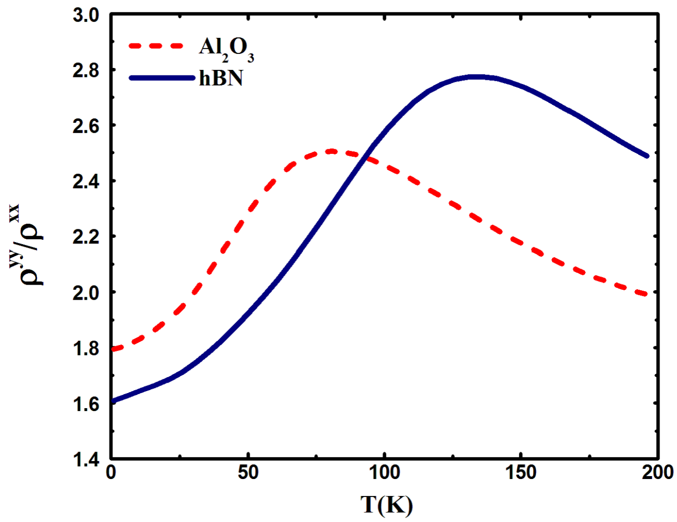

Figure 3.8: The anisotropy ratio of drag resistivity, ρ^{yy}/ρ^{xx}, as a function of temperature for two aligned phosphorene monolayers sandwiched by Al_2O_3 (solid line) and h-BN (dashed line) calculated within Hubbard LFC at electron density $n = 3 \times 10^{12}\mathrm{cm}^{-2}$. Here we set $d = 5$ nm and $\eta = 1$ meV.

shifting toward higher energies. Having said that, it is worth pointing out that the changing inter-layer distance does not significantly change the drag anisotropy ratio. To trace this behavior, we plot both scaled ρ^{xx} and ρ^{yy} as a functions of temperature for two different layer spacings: $d = 2$ nm and 5 nm in Fig. 3.6(b), which shows that the anisotropy ratio is less dependent on the inter-layer distance.

The effect of electron density on the drag resistivity is also of interest; hence, we illustrate it in Fig. 3.7(a). As expected for double-layer systems, for which the electron density increases, the Coulomb drag decreases and the resistivity peak moves towards higher temperature [79]. Moreover, it is worth mentioning that the anisotropic effect is more pronounced at lower electron density.

By including the Hubbard zero-temperature LFC, improvements on the RPA results are studied in Fig. 3.7(b). Here, we employ the intra-layer local field factor, Eq.(2.19), which is responsible for most of the drag resistivity enhancement by the short-range interaction effects [94]. Exchange interaction, which is taken into account by the Hubbard LFC, impacts the inter-layer interaction through the dielectric function of the system (see Eq.

(2.17)). Our calculations show that including the LFC factor enhances the drag resistivity results notably by strengthening the inter-layer interaction [94]. Furthermore, for the parameters used here one can see that the values of the anisotropy ratio are almost the same for both approximations. We also investigate the effects of substrate and spacer dielectric materials on the anisotropic drag resistivity by considering two already experimentally used insulators, namely Al_2O_3 [95] and h-BN [91], in phosphorene systems. Here, we assume $n = 3{\times}10^{12}\mathrm{cm}^{-2}$ corresponding in h-BN case to density parameter $r_s \sim 5$ which makes it necessary to consider the LFC factor in our calculation. The results indicate that including the LFC in drag resistivity calculations is important for both studied substrates. Significant differences between the results of RPA and local field factor approximation suggest a strong sensitivity of the drag resistivity to the effective intra-layer electron-electron interactions. Our results indicate that the anisotropic drag resistivity has larger values at all temperatures, when Al_2O_3 is used as spacer/substrate compared with the case in which h-BN is used (see Fig. 3.7(c)), due to a larger dielectric constant of Al_2O_3. Employing the high- κ materials as substrates/spacers reduces screening, and as a result enhances the inter-layer electron-electron interactions.

Finally, we present the anisotropy ratio for two different substrates in Fig. 3.8. We have employed Hubbard LFC to dielectric function to account for exchange short-range effects. Calculations show that different substrates has a moderate effect on the anisotropy ratio and shift the maximum expected anisotropy ratio.

3.3 Conclusion

To summarize, we have derived a formula for the anisotropic drag resistivity in a structure composed of two spatially separated 2D electron gas systems with parabolic band structures. We have assumed that the electron gases are sandwiched by insulators so that there is no tunneling between the layers. We have chosen double-layer phosphorene as an example system on which we apply our anisotropic drag theory. Our numerical results confirm that the drag resistivity depends not only on the typically considered parameters such as temperature, inter-layer separation, carrier density and nature of elementary excitations, but also on the direction of momentum transfer between the two layers in addition to the rotational parameter. Our calculations also show that while the diagonal elements of anisotropic drag resistivity tensor have different values due to different electron effective masses along x and y directions at any temperatures of interest, there are non-zero off-diagonal elements for the rotated structure. The non-zero off-diagonal elements have not been reported before in a 2D coupled system without an applied magnetic field. According to the numerical results, both diagonal elements of anisotropic drag resistivity tensor increase with decreasing interlayer separation and electron density. We show that, the anisotropic ratio varies effectively with the change of temperature and electronic density. To improve on RPA results at low electron density, we have included the zero temperature Hubbard LFC factor in our calculations and shown that the inclusion of LFC strongly influences the drag resistivity values. Moreover, we have studied the effects of substrate/spacer on the anisotropic drag resistivity. We show that a substrate/spacers with high dielectric constant is able to increase the anisotropic drag resistivity considerably. These results provide qualitative insights into the impact that an anisotropic band structure can have on drag resistivity, as an important transport quantity in a coupled 2D structure. The present work also suggests that the rotational parameter between layers can be considered as an extra degree of freedom for the applications of momentum transfer between coupled layers.

Chapter 4

Optical conductivity with the Rashba effect

"What is the optical response of an anisotropic 2D electron gas system in the presence of Rashba spin-orbit interaction?"

In this chapter [1] we calculate the optical conductivity of an anisotropic two-dimensional system with Rashba spin-flip excitation within the Kubo formalism. We show that the anisotropic Rashba effect caused by an external field changes significantly the magnitude of the spin splitting. Furthermore, we obtain an analytical expression for the longitudinal optical conductivity associated with inter-band transitions as a function of the frequency for arbitrary polarization angle. We find that the diagonal components of the optical conductivity tensor are direction-dependent and the optical absorption spectrum exhibits a strongly anisotropic absorption window. The height and width of this absorption window are very sensitive to the anisotropy of the system . While the height of absorption peak increases with increasing effective mass anisotropy ratio, the peak intensity is larger when the light polarization is along the armchair direction. Moreover, the absorption peak width becomes broader as the density of state mass or Rashba interaction is

---

[1] The results of this chapter were published in Physical Review B 96 (7), 075411 (2017) [40]

enhanced. These features in the optical absorption spectrum can be used to determine parameters relevant for spintronics.

4.1 Spin-orbit interaction

Nowadays, spin-orbit coupling interaction is a field of great interest owing to potential applications in spintronic phenomena and electric manipulation of spins [96, 2, 97, 98]. This interaction shows up when crystalline lattices lack a center of inversion symmetry (the Dresselhaus type [99]) or there is a structural asymmetry in the interfaces/surface region of quantum wells (the Rashba type [100]). In two dimensional (2D) materials, when inversion symmetry is broken by an applied transverse electric field or a substrate, spin degeneracy is lifted due to the Rashba effect [101]. Therefore, transitions between spin split states results in a non-zero value for the optical conductivity in the presence of an alternating electric field. The absorption part of the optical conductivity can be used in order to probe the spin-split energy levels. Like the unique anisotropic properties of excitons in phosphorene [39], the spintronic parameters such as the Rashba coupling strength, electron density and also spin polarization in the 2D materials can be measured optically [102, 103, 5]. Phosphorene-like materials, group IV-VI compounds, resemble in many respects, for instance, in-plane anisotropy, orthorhombic lattice and puckered layered structure [104, 105]. Similar to phosphorene and as a consequence of their orthorhombic structure, transport, optoelectronic and spintronic properties of these materials are highly anisotropic [106, 107].

Recently, Xiao *et al.* [5] studied the optical conductivity of $\mathrm{MoS_2}$ in the presence of spin-orbit coupling and found that the Rashba spin-orbit parameter can change the absorption peak or absorption window in the optical spectrum. In contrast to the isotropic band structure of $\mathrm{MoS_2}$ the anisotropic band structure in phosphorene results in a highly anisotropic Rashba splitting; [108, 109] hence, the strength of spin splitting depends on the direction of wave vector, as well as its magnitude [109]. The anisotropic Rashba spin-orbit interaction in 2D electron or hole gas systems due to the k-cubic Rashba spin-orbit interaction gives rise to different features in the optical conductivity, anisotropic spin susceptibility and also distinctive behavior of the spin Hall conductivity [110, 111]. Another anisotropic behavior of the spin splitting appears for the interplay between both Rashba and Dresselhaus spin-orbit coupling in a 2D electron gas. It has been shown that the

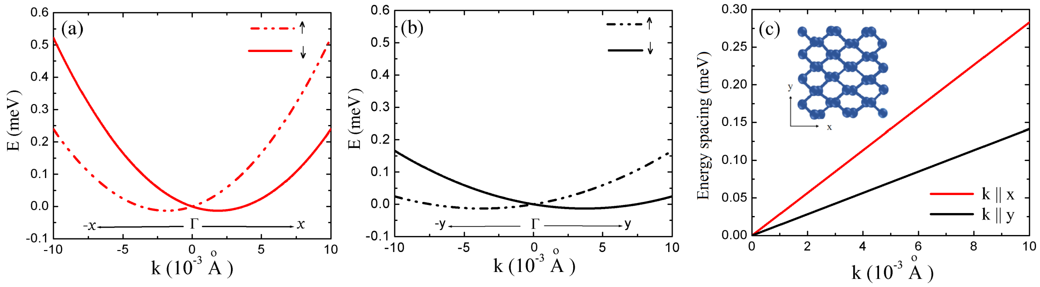

Figure 4.1: Energy dispersion (a) along the x direction (θ=0) and (b) along the y direction ($\theta = \pi/2$) with m_x=m_0, m_y=4m_0, and α_R=10meV$\mathring{A}$ (c) Spin splitting along the x and y directions for several values of α_R with m_x=m_0 and m_y=4m_0. The inset figure is a top view of an anisotropic monolayer with the x and y axes being the armchair and zigzag directions, respectively.

anisotropic dynamical optical conductivity can be used as a powerful tool to probe and manipulate the coupling strengths and set out the range of frequencies where the optical conductivity is essentially non-zero [112].

In this Chapter, we use the k-linear Rashba Hamiltonian for anisotropic 2D materials, such as phosphorene and group-IV monochalcogenides, which have been predicted to exhibit an anisotropic energy band [113, 32, 104]. Based upon the Kubo formalism, we obtain an analytical expression for the longitudinal optical conductivity with arbitrary polarization angles, including inter-band transitions. In contrast to isotropic systems, the longitudinal optical conductivity depends not only on the Rashba parameter but most importantly also on the effective mass anisotropy. The most significant contribution to the optical absorption occurs when the polarization of light is along the armchair direction (the direction with a smaller effective mass). We find that the extrinsic spin-orbit coupling due to the broken inversion symmetry is strongly anisotropic which has an impact on the optical response of 2D electron systems. The level splitting caused by the anisotropic Rashba effect gives rise to an optical response with a direction-dependent absorption peak. The width of the absorption window depends strongly on both the polarization direction and the effective mass ratio. The latter can be considered as an additional degree of freedom to tune the height and width of this absorption peak. High carrier mobility or increased electric field shifts the position of the absorptive peak to higher frequencies which can be adjusted

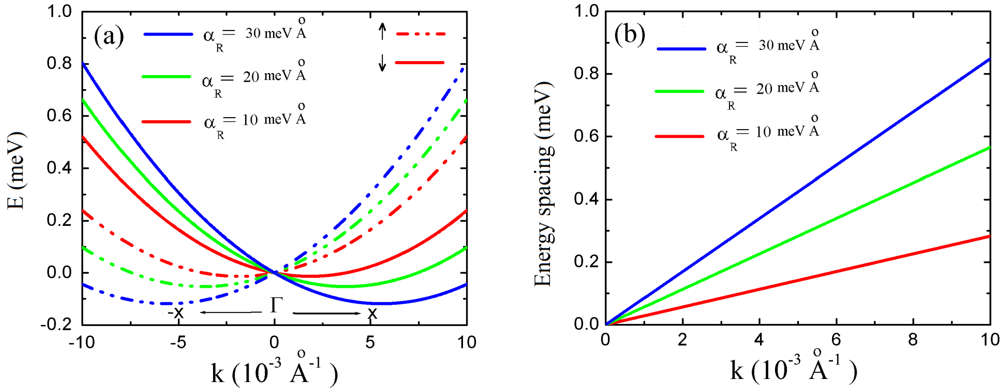

Figure 4.2: (a) Energy dispersion and (b) spin splitting along the x (armchair) direction for a few values of α_R with m_y=$4m_0$ and m_x=m_0.

appropriately. Our calculations of the absorption part of the optical conductivity with Rashba spin-orbit coupling are compared with measurement of infrared spectra on BP thin film at different polarizations [114]. Moreover, these values compare favorably with the optical conductivity of typical MoS_2 in the presence of Rashba interaction at low temperature in the infrared to terahertz spectral range [5]. We predict that single and few layer BP with anisotropic crystal structure and MoS_2 have great potential for infrared optoelectronics. Whereas phosphorene is a good example of a 2D anisotropic system, our formalism is also applicable to other 2D puckered materials.

4.2 Paraboloidal energy band with anisotropic Rashba effect

We study the low-energy dispersion and optical conductivity of a 2D system with paraboloidal energy band in the presence of Rashba spin-orbit coupling. We assume that the 2D system is a puckered honeycomb lattice where the x and y axes are taken to be along its armchair and zigzag directions, respectively. The Hamiltonian for such a system including the extrinsic Rashba term is given by:

$$\hat{H} = \hat{H}_0 + \hat{H}_R \; . \tag{4.1}$$

Here, $\hat{H}_0$ is the **k.p** free-electron Hamiltonian whose low-energy spectrum for an anisotropic 2D system is obtained as [115]

$$\hat{H}_0 = \frac{\hbar^2}{2}(\frac{k_x^2}{m_x} + \frac{k_y^2}{m_y})\hat{\sigma_0} \ , \tag{4.2}$$

where m_x and m_y are the electron effective masses along the x and y directions respectively, and $\hat{\sigma_0}$ is the 2×2 unitary matrix. The Rashba anisotropic Hamiltonian, which has been recently introduced for phosphorene [109] can be rewritten as

$$\hat{H}_R = -\alpha_R(\sqrt{\frac{m_d}{m_x}}k_x\hat{\sigma_y} - \sqrt{\frac{m_d}{m_y}}k_y\hat{\sigma_x}) \ . \tag{4.3}$$

Here, α_R is the Rashba coefficient, $m_d = \sqrt{m_x m_y}$ is the density-of-state masses and $\hat{\sigma_x}$ and $\hat{\sigma_y}$ are the Pauli matrices.

Upon diagonalizing the total Hamiltonian, one obtains two branches of the energy spectrum:

$$E^{\lambda}(\mathbf{k}) = \frac{\hbar^2 k^2 R(\theta)}{2} + \lambda\alpha_R^*(\theta)k \ , \tag{4.4}$$

where λ refers to the electron spin in the upper $(+)$ or lower $(-)$ branch, and θ denotes the angle of wave vector with respect to x-axis. $R(\theta)$ is the orientation parameter which is defined as [47]

$$R(\theta) = \left(\frac{\cos^2\theta}{m_x} + \frac{\sin^2\theta}{m_y}\right) \ , \tag{4.5}$$

and α_R^* is the anisotropic Rashba coefficient, given by:

$$\alpha_R^*(\theta) = \alpha_R\sqrt{m_d R(\theta)} \ . \tag{4.6}$$

To illustrate the effect of Rashba spin-orbit coupling on the anisotropic band structure, we plot the energy dispersion of the Rashba spin-split branches and energy spacing (the energy difference between the spin up and spin down branches) along the two main crystallographic directions in Fig. 4.1. Due to the Rashba interaction, the energy dispersion deviates from a parabola for each spin branch. Moreover, the anisotropic characteristic of the spin-split branches as a result of different effective masses along the armchair (x) and zigzag (y) directions is clearly observed. Also, it can be seen from Fig. 4.1(c) that the energy is direction-dependent and as expected along the armchair direction with smaller effective mass, the spin splitting is stronger. It is known that the Rashba spin-orbit interaction can be tuned by an external electric field, so, we show the energy dispersion and energy spacing along the armchair (x) direction for different Rashba parameters in Figs. 4.2(a) and 4.2(b). We find that the dispersion relation of a 2D material with anisotropic band structure can be well-tuned by the directional effective masses as well as the Rashba coefficient. Besides, there is a uniform enhancement of the energy spacing with increasing Rashba parameter due to the linear momentum dependence of the spin splitting interaction.

4.3 Optical conductivity

In a spin-orbit coupled system, the optical conductivity due to the transitions between different spin states is an important quantity. We calculate this property using the Kubo linear response formalism for a 2D system with anisotropic parabolic energy band in the presence of Rashba interaction. Assuming a spatially homogeneous electric field, the Kubo formula for conductivity which starts from the current-current correlation function, is given by [116, 100]

$$\sigma_{ij}(\mathbf{q},t) = \frac{ine^2}{m\omega}\delta_{ij} + \frac{1}{\omega}\int_0^\infty e^{i\bar{\omega}} < [\hat{J}_i(\mathbf{q},t), \hat{J}_j(\mathbf{q},0)] > dt \ , \tag{4.7}$$

where indices i and j stand for the two Cartesian coordinates x, y and n is the electron density, $\bar{\omega} = \omega + i\eta$ ($\eta \to 0^+$) and $\hat{J}_i = e\hat{v}_i$ is the current density operator with $\hat{v}_i = \hbar^{-1}\partial\hat{H}/\partial k_i$ being the electron velocity operator. In this paper, we concentrate on the absorptive part of the optical conductivity which is the real part of this complex quantity [117]. In the optical limit $q \to 0$, the dynamical optical conductivity can be obtained as follows:

$$\sigma_{ij}(\omega) = \frac{ie^2}{\omega}\sum_{\lambda,\lambda'}\sum_{\mathbf{k},\mathbf{k}'}\psi_{ij}(\mathbf{k},\mathbf{k}',\lambda,\lambda') \times \frac{f^0(E^\lambda(\mathbf{k})) - f^0(E^{\lambda'}(\mathbf{k}'))}{E^\lambda(\mathbf{k}) - E^{\lambda'}(\mathbf{k}') + \hbar(\omega + i\eta)} \ , \tag{4.8}$$

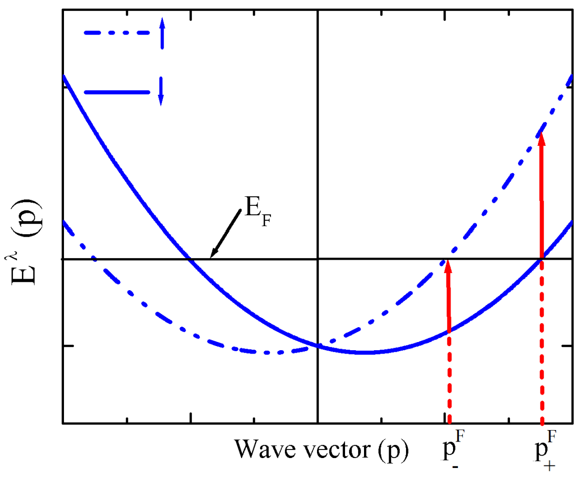

Figure 4.3: Transitions between spin branches. The arrows correspond to the transitions with threshold frequencies of $(2\alpha_R p_F^{\pm})/\hbar$.

where $\psi_{ij}(\mathbf{k},\mathbf{k}',\lambda,\lambda')$ is defined as

$$\psi_{ij}(\mathbf{k},\mathbf{k}',\lambda,\lambda') = \langle \mathbf{k}\lambda|\, \hat{v}_i\, |\mathbf{k}'\lambda'\rangle\, \langle \mathbf{k}'\lambda'|\, \hat{v}_j\, |\mathbf{k}\lambda\rangle \ . \tag{4.9}$$

The electron velocity operators for two spin-split branches in the x and y directions are given as

$$\begin{aligned} \hat{v}_x &= \frac{1}{\hbar}\left(\frac{\hbar^2 k_x}{m_x}\hat{\sigma}_0 - \alpha_R\sqrt{\frac{m_d}{m_x}}k_x\hat{\sigma}_y\right) \ , \\ \hat{v}_y &= \frac{1}{\hbar}\left(\frac{\hbar^2 k_y}{m_y}\hat{\sigma}_0 + \alpha_R\sqrt{\frac{m_d}{m_y}}k_y\hat{\sigma}_x\right) \ . \end{aligned} \tag{4.10}$$

Before calculating the eigenstates of the system, $|\mathbf{k}\lambda\rangle$, we introduce a new 2D wave vector $\mathbf{p} = (p_x, p_y)$ which is defined as $\mathbf{k} = \sqrt{M/m_d}\,\mathbf{p}$ with M being the mass tensor whose diagonal elements are m_x and m_y [44]. Now, we can rewrite the free electron and Rashba parts of the total Hamiltonian as follows:

$$\hat{H}_0 = \frac{\hbar^2 p^2}{2m_d}\hat{\sigma}_0 \ , \tag{4.11}$$

$$\hat{H}_R = -\alpha_R(\mathbf{p} \times \hat{z}).\hat{\sigma} \ , \tag{4.12}$$

where $\hat{\sigma} = \hat{\sigma}_x\hat{i} + \hat{\sigma}_y\hat{j}$. Thus, the two spin-split eigenstates can be identified as:

$$|\mathbf{p}\lambda\rangle = \frac{e^{(i\mathbf{p}.\mathbf{r})}}{\sqrt{2}} \begin{pmatrix} 1 \\ \lambda\frac{p_y - ip_x}{p} \end{pmatrix} \tag{4.13}$$

with $r = (x, y)$ being a 2D real space position vector. Also, the expressions for the velocity operators can be written in terms of $\mathbf{p}$:

$$\begin{aligned} \hat{v}_x &= \frac{\hbar}{\sqrt{m_x m_d}}\Big(p_x\hat{\sigma}_0 - p_R\hat{\sigma}_y\Big) \ , \\ \hat{v}_y &= \frac{\hbar}{\sqrt{m_y m_d}}\Big(p_y\hat{\sigma}_0 + p_R\hat{\sigma}_x\Big) \ , \end{aligned} \tag{4.14}$$

where $p_R = \alpha_R m_d/\hbar^2$ is the effective Rashba wave vector. It has been shown that the spin-conserving intra-band transitions give rise to low frequency absorption, whereas the spin-flip transitions result in a wide absorption peak [112, 5]. We focus on the optical conductivity due to the inter-band spin flip excitations. As ordinary 2D electron gas systems [112], it can be shown that the off-diagonal elements of the optical conductivity (transverse or Hall conductivity) are zero in the absence of a magnetic field, *i.e.* $\sigma_{xy} = 0$. By making use of Eqs. (4.13) and (4.14), one can calculate the diagonal elements of the ψ tensor as:

$$\psi_{jj}(\mathbf{p}, \mathbf{p}'; \lambda, \lambda') = \frac{\hbar^2}{2m_j m_d}\Big(p_j^2(1+\lambda\lambda') + p_\alpha^2(1+\lambda\lambda' cos2\phi) + 2p_R p_j cos\phi(1+\lambda\lambda')\Big)\delta_{\mathbf{pp}'} \ , \tag{4.15}$$

where $\phi = tan^{-1}(p_y/p_x)$. Accordingly, the non-equal diagonal components of optical conductivity (longitudinal optical conductivity) due to spin-flip transitions are obtained as:

$$\sigma_{jj}(\omega) = \frac{ie^2\hbar^2 p_R}{2\omega m_j m_d}\int\frac{pdpd\phi}{(2\pi)^2}(1-cos2\phi)\left(\frac{f^0(E^-(\mathbf{p})) - f^0(E^+(\mathbf{p}))}{E^-(\mathbf{p}) - E^+(\mathbf{p}) + \hbar(\omega + i\eta)} + (E^- \leftrightarrow E^+)\right) . \tag{4.16}$$

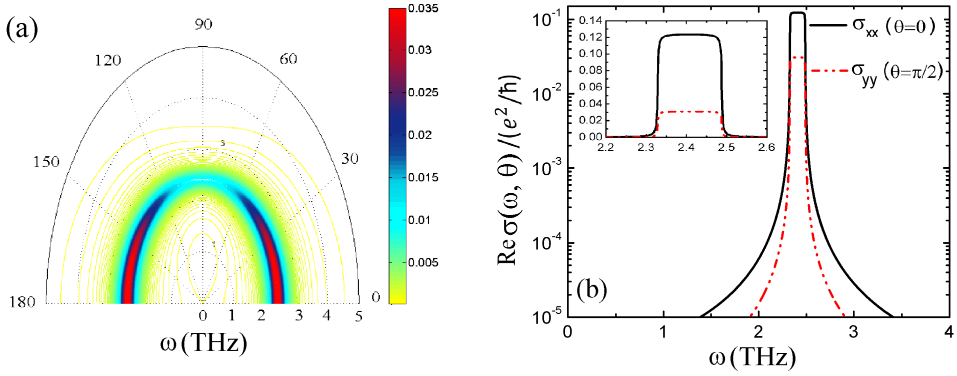

Figure 4.4: Real part of longitudinal optical conductivity as a function of excitation frequency: (a) for all θ, and (b) for $\theta = 0$ and $\theta = \pi/2$ with $n = 1 \times 10^{13}\text{cm}^{-2}$. Here we set α_R=10 meV$\mathring{A}$, m_y=$4m_0$ and m_x=m_0.

After performing the **p** integral, the following expression is obtained for σ_{jj} at zero temperature:

$$\sigma_{jj}(\omega) = -\frac{ie^2 m_d^2}{2\pi m_j \omega \hbar^4}\left[1 + \frac{\hbar^3 \omega R(\theta)\Lambda(\omega)}{8(\alpha_R^*(\theta))^2}\right] , \tag{4.17}$$

with $\Lambda(\omega)$ defined as:

$$\Lambda(\omega) = \ln\left(\frac{(\omega - \omega_- + i\eta)(\omega + \omega_+ + i\eta)}{(\omega + \omega_- + i\eta)(\omega - \omega_+ + i\eta)}\right) , \tag{4.18}$$

where $\omega_\pm$ are the threshold frequency modes induced by the inter-branch electronic transition:

$$\omega_\pm = \frac{2\alpha_R^* p_\pm^F}{\sqrt{m_d R(\theta)\hbar}} . \tag{4.19}$$

Here, $p_\pm^F = p_F \mp p_R$ are the Fermi wave vectors for the two spin branches with $p_F = \sqrt{2n\pi - p_R^2}$. A schematic diagram for the optical transitions is shown in Fig. 4.3. The arrows correspond to the vertical transitions between two spin branches in the optical limit ($q \to 0$).

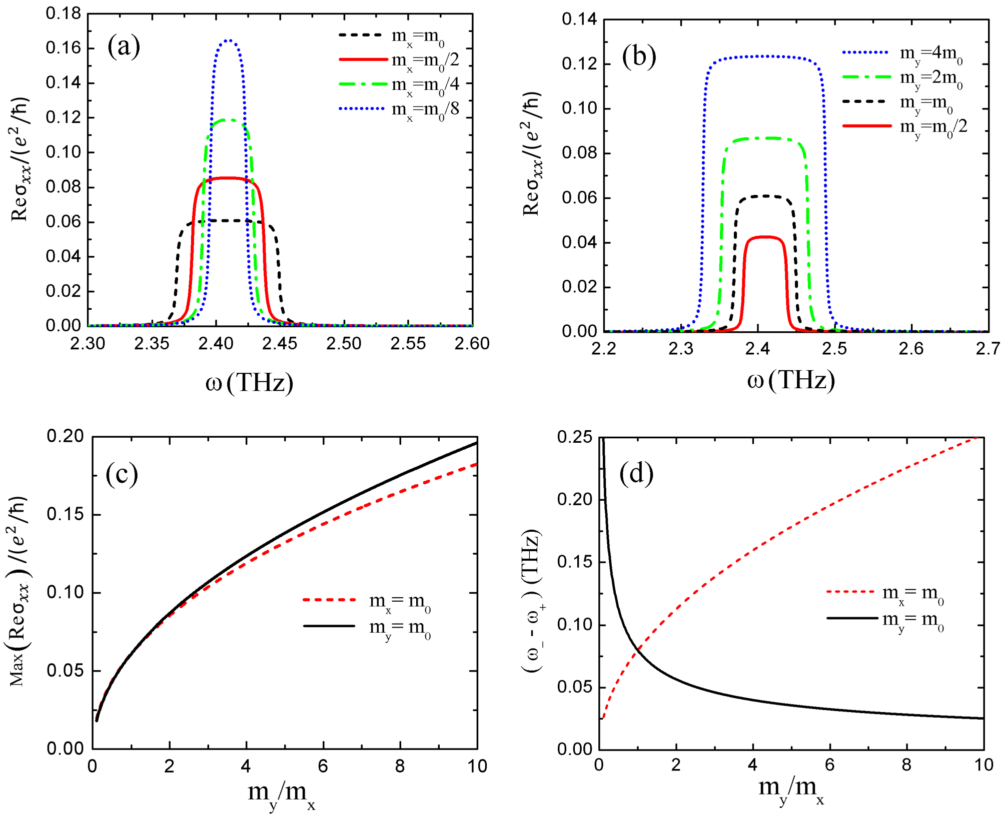

Figure 4.5: Real part of longitudinal optical conductivity as a function of excitation frequency for $\theta = 0$ with (a) $m_y = 4m_0$ and (b) $m_x = m_0$. (c) Maximum of real part of longitudinal optical conductivity as a function of mass anisotropy ratio. (d) Width of the absorption window as a function of mass anisotropy ratio. Here, we set $n = 1 \times 10^{13}\text{cm}^{-2}$ with α_R=10 meV $\mathring{A}$.

The longitudinal optical conductivity along an arbitrary polarization direction θ, is given by [50]:

$$\sigma(\omega,\theta) = \sigma_{xx} cos^2\theta + \sigma_{yy} sin^2\theta \ . \tag{4.20}$$

By inserting Eqs. (4.17) and (4.18) in the above equation we obtain:

$$\sigma(\omega,\theta) = -\frac{ie^2 m_d (\alpha_R^*(\theta))^2}{2\pi\omega\hbar^4}\left[1 + \frac{\hbar^3\omega R(\theta)\Lambda(\omega)}{8(\alpha_R^*(\theta))^2}\right] \ . \tag{4.21}$$

In Fig. 4.4(a), we illustrate the calculated real part of the anisotropic conductivity for arbitrary direction of polarization vector as a function of radiation frequency, ω, at a fixed electron density $n = 1 \times 10^{13}\text{cm}^{-2}$ and for α_R=10 meV$\mathring{A}$, m_y=4m_0 and m_x=m_0. As expected, the optical conductivity has its maximum value at $\theta = 0$ *i.e.* along the armchair direction of the 2D layer. The significantly smaller effective mass for the $\theta = 0$ direction suggests that the charge carriers prefer to flow along this direction. In addition, Fig. 4.4(b) shows the absorption part of the optical conductivity for the two main crystallographic directions $\theta = 0$ and $\theta = \pi/2$. The fact that the anisotropy ratio of the optical conductivity is equal to the inverse of the mass anisotropy ratio, *i.e.*, $\sigma_{yy}(\omega)/\sigma_{xx}(\omega) = m_x/m_y$, is clearly observed in this figure. Furthermore, as a consequence of the energy conservation law under vertical transitions ($q \to 0$) between spin branches (see Fig. 4.3)), the absorption part of the longitudinal optical conductivity at $T = 0$ has a step function like variation with the frequency, *i.e.*, a non-zero value for a range of frequencies which is given by

$$\omega_- - \omega_+ = \frac{2(\alpha_R^*)^2}{\hbar^3 R(\theta)} \ . \tag{4.22}$$

As is evident from Fig. 4.4, the absorption is in the THz region for the set of parameters used here. We have already mentioned above that the optical conductivity exhibits a strong dependence on the effective mass anisotropy. The variation of the real part of σ_{xx} with the effective mass along the x and y directions is shown in Fig. 4.5. One may notice that the mass asymmetry not only alters the maximum value of the optical conductivity but also changes the width of the peak. According to this figure, the peak height of $\sigma_{xx}(\omega)$ increases by decreasing the effective mass along the radiation polarization direction or increasing the effective mass along the direction perpendicular to the radiation polarization. In other words, a higher peak intensity is achieved as a consequence of the effective mass anisotropy ratio (m_y/m_x) enhancement. Moreover, the absorption window of the real part of longitudinal optical conductivity is extended by increasing the density of states mass (m_d). The effect of Rashba coupling strength on the absorption part of $\sigma_{xx}(\omega)$ is shown in Fig. 4.6(a). The absorption peak width is broadened and the onset frequency of the absorptive peak moves towards a higher value when the Rashba parameter increases [102]. The Rashba parameters chosen here are comparable to the as-obtained values for phosphorene and group-IV monochalcogenides from density functional theory calculations [109, 108]. For large values of α_R, a stronger spin splitting occurs which in turn shifts the absorption part of the optical conductivity from the THz to infrared frequencies. These features for the spin-flip absorption peak are similar to that of the conventional two dimensional electron gas systems and MoS_2 [5]. We observe that the predicted value of infrared spectra on BP thin film at different polarizations [114] is in very good agreement with our results of the absorption part of the optical conductivity for high value of Rashba parameters and density especially across the technologically relevant THz to mid-infrared spectrum [50]. We also depict the variation of the optical absorption with the electron density in Fig. 4.6(b) for fixed α_R=10 meV$\mathring{A}$ and effective masses m_y=$4m_0$ and m_x=m_0 . One of the important characteristics of this figure is that while the value of the peak height remains almost unchanged by increasing electron density, the absorption peak moves toward higher frequencies as a result of the Pauli blockade effect [118, 119, 120].

4.4 Conclusion

In summary, we have studied the energy spectrum and optical response of an anisotropic 2D electron gas system in the presence of Rashba spin-orbit interaction. Based on the Kubo formalism, we calculated the optical conductivity tensor considering the Rashba spin-flip excitations. We found that the effective mass anisotropy plays an important role in the optical absorption spectrum through the direction-dependent Rashba spin splitting. As a general result, the diagonal components of the optical conductivity tensor are inversely proportional to the corresponding effective mass elements. Furthermore, the effective mass asymmetry is an additional degree of freedom to tune the height and width of the absorption peak. This introduces aspects to the optical conductivity for spintronic applications of 2D anisotropic materials

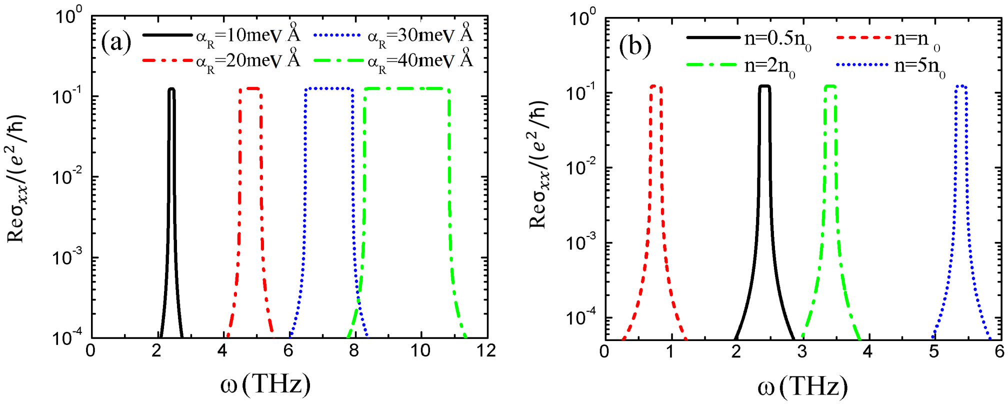

Figure 4.6: Real part of longitudinal optical conductivity as a function of excitation frequency for θ=0 with m_y=$4m_0$, m_x=m_0 for a few values of (a) Rashba parameter with $n_0 = 1 \times 10^{13}\text{cm}^{-2}$ and (b) electron density with α_R=10 meV $\AA$.

such as phosphorene and group-IV monochalcogenides. We also showed that larger optical absorption is generated when the polarization of radiation is along the armchair direction and its maximal value is enhanced by increasing the effective mass ratio. However, the width of the absorption window has a strong dependence on both the polarization direction and the effective mass ratio. Finally, the position of the absorptive peak moves to higher frequencies with increasing the Rashba parameter and electron density. Our results suggest an interesting way to determine some of the spintronic characteristics of a class of 2D nanostructures, with anisotropic Rashba effect, using optical methods.

Chapter 5

Surface optical phonon plasmon interaction

> "How do polar substrates/spacers influence the plasmons in monolayer and double-layer phosphorene systems?"

In this chapter[1], we investigate phosphorene on polar insulator substrates as shown in Fig. 5.1. We go beyond the assumption of independent electron and SO phonon modes and consider coupled plasmon-SO phonon oscillations. Here, we theoretically study the coupled plasmon-SO phonon interaction in monolayer and double-layer phosphorene on polar substrates using perturbation theory. We start from the expression for the dynamical dielectric function of the coupled system in a generalized RPA, and develop a general formalism, which includes the effect of anisotropic energy dispersion and rotationally misaligned double-layer system. In such systems having the interaction between electrons and SO phonons could yield phonon mediated electron-electron (e-e) interaction which creates new collective modes with highly anisotropic dispersion. We find that in the case of phosphorene, in contrast to graphene [121, 122, 123] and TMDs [6], the mode coupling effect

---

[1] The results of this chapter were published in Physical Review B **96** (7), 075411 (2017) [43].

not only modifies the plasmon dispersion relation but also enables us to tune the hybrid plasmon-SO phonon modes in two crystallography directions. So, anisotropy in phosphorene provides an extra dimension in the phase space of electron-SO phonon coupling.

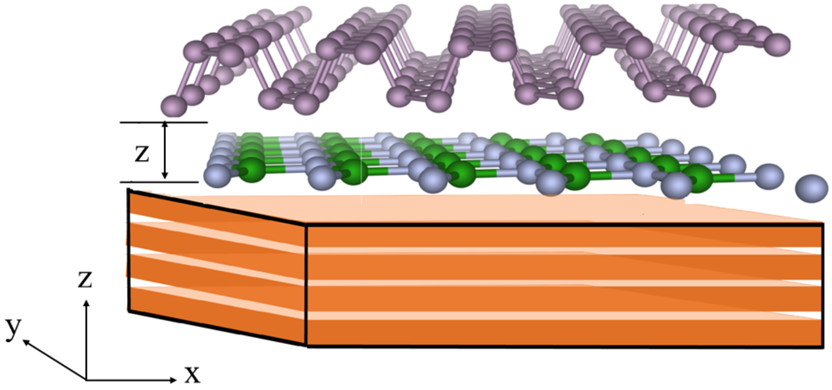

Figure 5.1: Schematic figure of a monolayer phosphorene where a polar insulating material (for example *h*-BN) has been used as a substrate. z indicates the vertical distance of the monolayer phosphorene from the substrate.

5.1 Introduction

The properties of the substrate often drastically alters the transport behavior of the 2D crystal and the overall characteristics of the device. Recently, phosphorene has been transferred on top of the *h*-BN substrate [7, 124]. The interaction between phosphorene and the substrate is considered to play a crucial role in the modulation of the electronic properties of phosphorene-based devices [125]. In most currently available 2DMs, a sample lies on the top of a polar substrate such as *h*-BN, SiO_2, SiC or Al_2O_3 [126, 91, 127, 15, 128]. In such heterostructures, the polar optical phonon modes of the substrate are localized near the 2DMs-substrate interface and are coupled to the surface optical (SO) phonon modes of the polar substrate through the long-range Fröhlich interaction. As a result, the SO phonon could be considered as the dominant plasmon-SO phonon coupling source in 2DMs on polar substrates. The coupling of SO phonon modes to the plasma oscillations of free carriers is known as plasmon-SO phonon coupling. These coupled modes may be observed by infrared (IR) transmission measurements [129, 130]. The plasmon-SO phonon coupling changes the dips in the IR reflectivity spectra from isolated plasmon and SO phonon frequencies to the normal coupled ones [123, 131].

The coupled plasmon-SO phonon modes have been extensively investigated in 2DMs with isotropic band structure such as graphene, silicene and germanene [132, 133, 134, 135]. It is shown that this phenomenon modifies many-body properties such as plasmon modes [122, 123, 136] and self energy [137] and can also change the mobility [138], effective mass [139, 137], scattering rate [140, 134] and inelastic lifetime [141] in carrier transport phenomena. Moreover, it can be considered as a mechanism for tuning the band gap [127, 142, 135].

In this chapter, we model a system of phosphorene on polar insulator substrates as shown in Fig. 5.1. We theoretically study the coupled plasmon-SO phonon modes in monolayer and double-layer phosphorene on polar substrates using perturbation theory. We start from the expression for dynamical dielectric function of the coupled system in the RPA, and develop a general formalism, which includes the effect of anisotropic energy dispersion and rotationally misaligned double-layer system. In such systems having the interaction between the electrons and substrate-SO phonons could yield phonon-mediated electron-electron interaction which creates a new set of collective modes with highly anisotropic dispersion. We find that in the case of phosphorene in contrast to graphene [122, 123] and TMDs [6], the mode coupling effect not only modifies the plasmon dispersion relation but also enables us to tune the hybrid plasmon-SO phonon modes in the two crystallographic directions. So, the anisotropy is an important feature of the coupled electron-SO phonon oscillation spectrum in phosphorene systems.

5.2 Hamiltonian for phosphorene on polar substrates

In a phosphorene multilayer system with no electron-phonon interaction, the electrons in each layer interact with themselves and also with the electrons in other layers through the following electron-electron interaction Hamiltonian:

$$H_{el-el} = \frac{1}{2}\sum_{ij}\sum_{\mathbf{kqp}} v_{ij}(q) a^{\dagger}_{\mathbf{k+q},i} a^{\dagger}_{\mathbf{p-q},j} a_{\mathbf{p},j} a_{\mathbf{k},i} \ , \tag{5.1}$$

where $v_{ij}(q) = v(q)e^{-qd_{ij}(1-\delta_{ij})}$ represents the diagonal (intralayer with $i = j$) and off-diagonal (interlayer with $i \neq j$) elements of the bare Coulomb potential matrix. Here, we define $v(q) = 2\pi e^2/q\epsilon_\infty$ with ϵ_∞ being the high-frequency dielectric constant and d_{ij} is the distance between i-th and j-th layers. Also, $a_{k,i}$ ($a^{\dagger}_{k,i}$) is the electron annihilation (creation) operator in layer i.

If the phophorene layers are supported by polar materials, an additional interaction term involving the electron-SO phonon coupling can be included by using the Fröhlich Hamiltonian [143]:

$$H_{el-ph} = \sum_{i}\sum_{\lambda}\sum_{\mathbf{kq}} [M_0^{\lambda}((q)] a^{\dagger}_{\mathbf{k+q},i} a_{\mathbf{k},i} (b_{\mathbf{q}\lambda} + b^{\dagger}_{-\mathbf{q}\lambda}) \ , \tag{5.2}$$

which renormalizes the screened electron-electron potential through the dielectric function matrix, $\epsilon_{ij}(\omega, \mathbf{q})$:

$$V^{sc}_{ij}(\omega, \mathbf{q}) = \frac{v_{ij}(q)}{det|\epsilon_{ij}(\omega, \mathbf{q})|}. \tag{5.3}$$

In Eq. (5.2), $b_{\mathbf{q}\lambda}$ ($b^{\dagger}_{\mathbf{q}\lambda}$) is the phonon annihilation (creation) operator with wave vector $\mathbf{q}$ and branch index λ and $M_0^{\lambda}(q)$ is the amplitude of the electron-SO phonon interaction [122]:

$$M_0^{\lambda}(q) = \left[v(q)\alpha\frac{\omega^{\lambda}_{SO}}{2}e^{-2qz}\right]^{1/2} \ , \tag{5.4}$$

where ω^{λ}_{SO} is the SO phonon frequency of the λ^{th} branch, z is the vertical distance between phosphorene and substrate and we define:

$$\alpha = \epsilon_\infty\left[\frac{1}{\epsilon_\infty + 1} - \frac{1}{\epsilon_0 + 1}\right], \tag{5.5}$$

with ϵ_o being the zero-frequency dielectric constant. Here, we assume that the phonon-phonon interaction is negligible so each mode couples to the electrons independently. In order to study the effect of electron-SO phonon coupling on the collective charge-density excitations, one needs to obtain the zeros of the determinant of the dynamical dielectric function matrix (the poles of the screened potential). We use the dynamical RPA dielectric function in which the contribution of the electron-SO phonon interaction is taken into account [144]:

$$\epsilon_{ij}(\omega, \mathbf{q}) = \delta_{ij} - U_{ij}(\omega, q)\Pi_i(\omega, \mathbf{q}). \tag{5.6}$$

Here, $U_{ij}(\omega, q)$ is the combined Coulomb and phonon-mediated interactions between ith and jth layers:

$$U_{ij}(\omega, q) = U_0(\omega, q)e^{-qd_{ij}(1-\delta_{ij})}, \tag{5.7}$$

where $U_0(\omega, q) = v_{ph}(\omega, q) + v(q)$ and the SO phonon-mediated electron-electron interaction, $v_{ph}(\omega, q)$, is given by [145]:

$$v_{ph}(\omega, q) = \sum_{\lambda}[M_0^{\lambda}(q)]^2 D_0^{\lambda}(\omega). \tag{5.8}$$

$D_0^{\lambda}(\omega)$ is the bare propagator for a phonon of branch index λ:

$$D_0^{\lambda}(\omega) = \frac{2\omega_{SO}^{\lambda}}{\omega^2 - (\omega_{SO}^{\lambda})^2}. \tag{5.9}$$

In the case of monolayer, we will have $\tau_i = 0$. The knowledge of the appropriate limiting behavior of the polarization function is important in investigating the excitation spectrum specially the collective excitations of the system. Therefore, we obtain the polarization function in the dynamic long-wavelength limit where the plasmon excitations are important due to their long lifetimes. In this limit, the polarization function of Eq. (5.6) can be approximated as (see the appendix B):

$$\frac{\Pi_i(\omega, q, \theta)}{g_{2d}} \approx R_i(\theta)E_F\frac{q^2}{\omega^2}. \tag{5.10}$$

In the following section, we present our calculations for the coupled plasmon-SO phonon modes in both monolayer and double-layer phosphorene systems with a number of experimentally chosen polar substrates/spacers.

5.3 Coupled plasmon SO-phonon modes in monolayer phosphorene

The RPA dielectric function for a monolayer system in which the electrons are coupled to SO phonons of a polar substrate can be obtained through

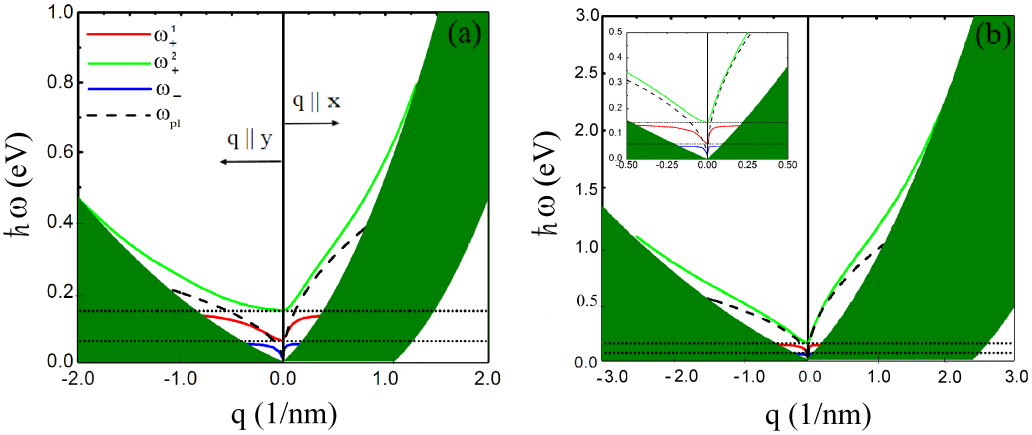

Figure 5.2: The hybrid plasmon-SO phonon dispersion in phosphorene monolayer on SiO_2 substrate as a function of wave vector q for two main crystallographic directions of phosphorene: $\theta = 0$ ($q \parallel x$) and $\theta = \pi/2$ ($q \parallel x$) with (a) $n = 1 \times 10^{13}$ cm^{-2}, (b) $n = 5 \times 10^{13}$ cm^{-2} and $z = 0.2$ nm. The uncoupled plasmon dispersion is shown by dashed curve. The two horizontal lines represent the frequencies of the SO phonon modes, *i.e.* $\hbar\omega_{so}^1 = 60$ meV and $\hbar\omega_{so}^2 = 146$ meV.

Table 5.1: Physical parameters of selected polar materials from Ref. [127].

	SiO_2	h-BN	Al_2O_3
$\hbar\omega^1_{SO}$(meV)	60	101	55
$\hbar\omega^2_{SO}$(meV)	146	195	94
ϵ_0	3.9	5.1	12.5
ϵ_∞	2.5	4.1	3.2
α	0.2	0.132	0.525

summing over all the bare bubble diagrams as [122]

$$\epsilon_i(\omega, \mathbf{q}) = 1 - \frac{2\pi e^2}{\epsilon_\infty q}\Pi_i(\omega, \mathbf{q}) + \sum_\lambda \frac{\alpha e^{-2qz}}{1 - \alpha e^{-2qz} - \omega^2/(\omega^\lambda_{so})^2}. \tag{5.11}$$

In the long-wavelength limit ($q \to 0$) by inserting Eq. (5.10) into Eq. (5.11), we get the following coupled collective modes (see appendix B):

$$\omega^\lambda_{(+)}(q, \theta) = \omega^\lambda_{so}\big(1 + \alpha e^{-2qz}\frac{\omega^2_{pl}(q, \theta)}{(\omega^\lambda_{so})^2}\big), \tag{5.12}$$

$$\omega_{(-)}(q, \theta) = \omega_{pl}(q, \theta)\big(1 - \frac{\alpha}{2}e^{-2qz}\big), \tag{5.13}$$

where $\omega_{pl}(q, \theta) = \sqrt{2\pi n e^2 R_i(\theta) q/\epsilon_\infty}$ is the plasmon frequency of the uncoupled anisotropic system. We consider a phosphorene monolayer sandwiched by polar materials such as SiO_2, h-BN or Al_2O_3 whose physical parameters are listed in Table 5.1. In addition, the effective masses in x and y directions of phosphorene monolayer are given as $m_x \approx 0.15m_0$ and $m_y \approx 0.7m_0$ where m_0 is the free electron mass [64].

In Fig. 5.2, we depict the coupled and uncoupled plasmon modes of phosphorene monolayer on SiO_2 substrate calculated for two main crystallographic directions $\theta = 0$ ($q \parallel x$) and $\theta = \pi/2$ ($q \parallel y$). According to this figure, in the case of SiO_2 substrate, there are three hybrid modes, one plasmon-like, $\omega_-(q, \theta)$, and two phonon-like, $\omega^\lambda_+(q, \theta)$, as were previously shown experimentally [129] for graphene monolayer. It can be seen that the $\omega_-(q, \theta)$ (plasmon-like mode) is lower in energy than the uncoupled plasmon mode, $\omega_{pl}(q, \theta)$, and the lower (upper) phonon-like branch starts from ω^1_{so} (ω^2_{so}) at $q = 0$ and increases below (above) the uncoupled plasmon dispersion by increasing

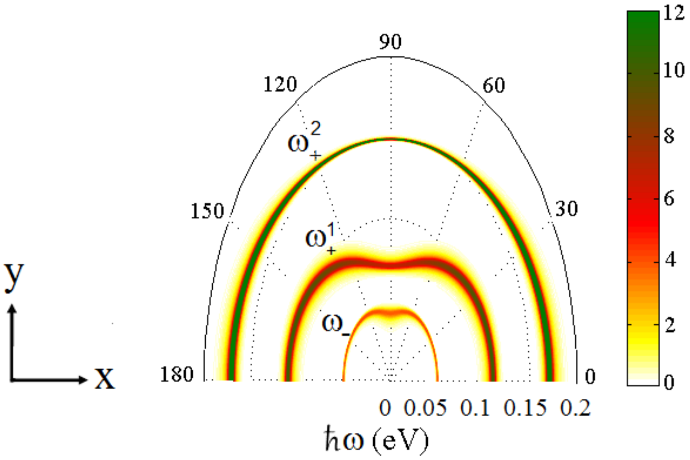

Figure 5.3: Loss function, $|\Im(1/\det\epsilon(\omega, q, \theta))|$, for q=0.1 nm with n = $1{\times}10^{13}$cm^{-2} and η = 5 meV. The radial and azimuthal coordinates are ω and the angular orientation of $\mathbf{q}$, respectively.

q along both directions. The coupling is strong when the frequencies of the phonon-like modes deviate considerably from the bare SO phonon modes, ω_{so}^{λ} (see Eq. (5.12)). As expected in 2DMs with anisotropic band structure, the hybrid plasmon-SO phonon modes have higher resonance frequencies [46, 44] and the plasmon-like modes are more affected by the electron-SO phonon coupling in the direction of the lighter mass, $q \parallel x$. In the coupled system, the electrons can be scattered either by the emission of hybrid plasmon-SO phonon modes (ω_+, ω_-) or by the single particle excitation (SPE). The boundary of the SPE continuum represented by green shaded area in Fig. 5.2 is given by:

$$\hbar\omega^{\pm}_{(SPE)}(q, \theta) = \frac{R_i(\theta)\hbar^2}{2} \pm q\nu_F\sqrt{R_i(\theta)m_d}\ . \tag{5.14}$$

Though all hybrid plasmon-SO phonon excitations are damped at IR frequencies, the plasmon-like mode, ω_-, experiences the Landau damping at smaller q with respect to the phonon-like modes. On the other hand, the higher frequency phonon-like mode, ω_+^2, stays away from ω_{SO}^2 and enters the SPE region at large q for both directions. Therefore, this mode shows a strong coupling and can be easily detected. Moreover, at high densities (Fig. 5.2(b))

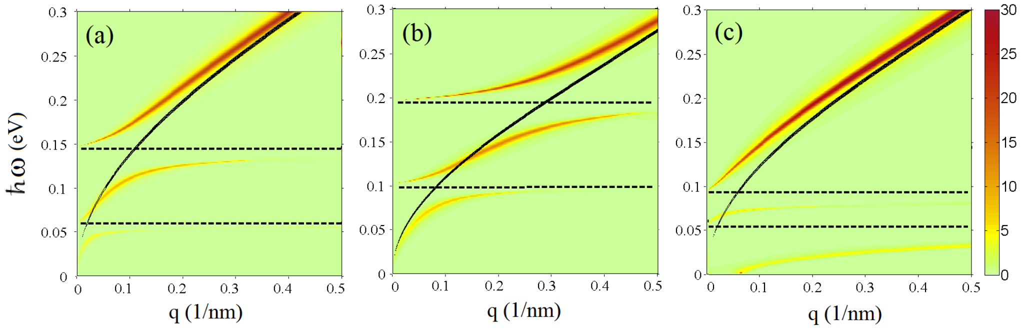

Figure 5.4: Effect of changing substrate: $|\Im(1/\det\epsilon(\omega,q,\theta))|$ for phosphorene monolayer at $\theta = 0$ ($q \parallel x$). The solid black line is the uncoupled plasmon branch and the two horizontal black dashed lines represent the frequencies of SO phonon modes of the substrate: (a) SiO_2, (b) h-BN and (c) Al_2O_3 with $n = 1 \times 10^{13}$ cm^{-2}, z =0.2 nm and η=5 meV.

where the Fermi energy exceeds the SO phonon energy *i.e.* $E_F \gg \hbar\omega_{SO}^2$, the upper phonon-like branch strongly deviates from the uncoupled SO phonon's energy while the ω_+^1 branch still remains between the two phonon energies. Thus, the high energy phonon-like mode, ω_+^2, which is very sensitive to the density and direction, can be considered as a tunable quantity for applications in optical plasmonic devices. Furthermore, we study the impact of angular orientation of $\mathbf{q}$ on the behavior of hybrid plasmon-SO phonon modes by plotting the loss function, $|\Im(1/\det\epsilon(\omega,q,\theta))|$, for q=0.1 nm (see Fig. 5.3). The results show that the maximum value of loss function occurs around θ= 0 and 180 (along x direction) for all three branches.

In order to explore the effects of a specific substrate on the hybrid plasmon-SO phonon modes, we show the loss function of phosphorene monolayer on (a) SiO_2, (b) h-BN and (c) Al_2O_3 polar substrates along x direction ($\theta = 0$) in Fig. 5.4. One can see that using the Al_2O_3 (with higher α) as a polar substrate results in a strong coupling as evidenced by considerable deviation of ω_- from ω_{pl} and of ω_+^λ from ω_{SO}.

It should be pointed out that while the phonon frequency ω_{SO} is an important parameter for the phonon-like modes, ω_+^λ, the α parameter mostly affects the plasmon-like spectrum. Hence, the choice of substrate can be used to engineer the plasmon dispersion in phosphorene.

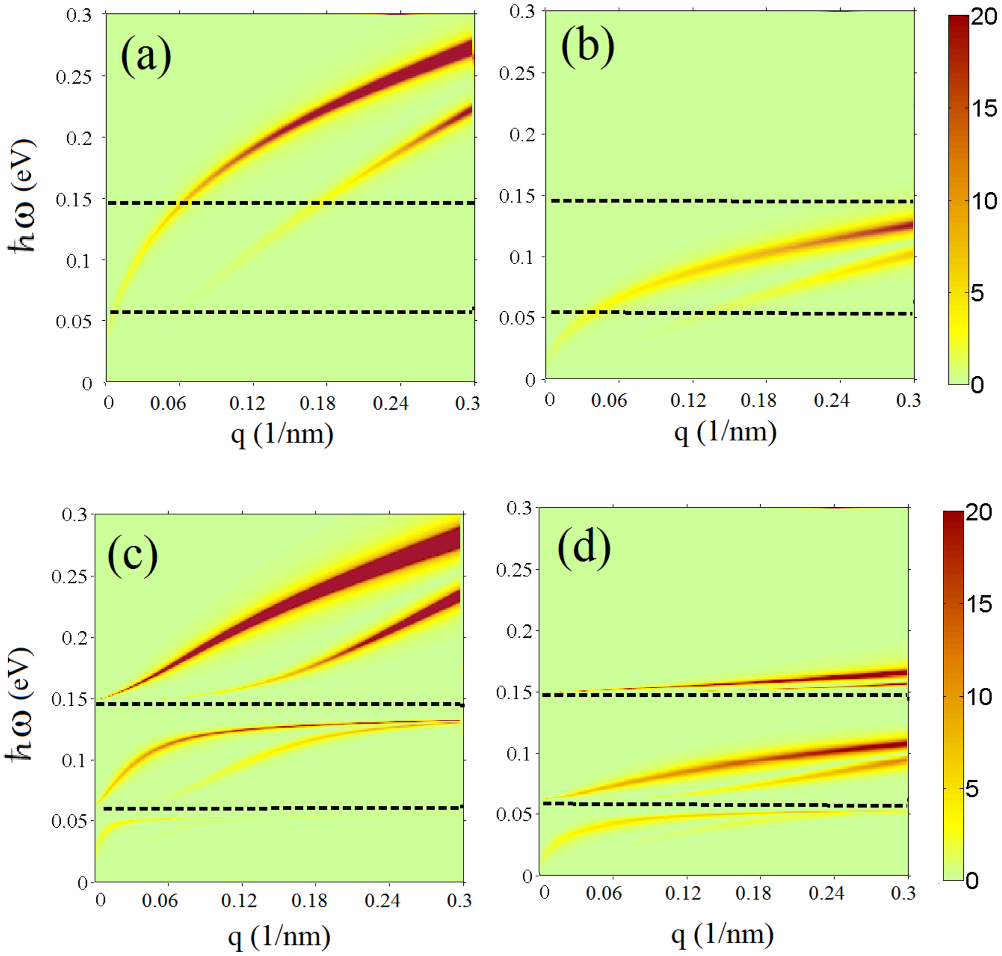

Figure 5.5: (a) and (b) The uncoupled and (c) and (d) coupled plasmon-SO phonon modes for two aligned phosphorene monolayers sandwiched by SiO_2 as a function of wave vector q for two main crystallographic directions: (a) and (c) $\theta = 0$ ($q \parallel x$) and (b) and (d) $\theta = \pi/2$ ($q \parallel y$) with $n = 1 \times 10^{13}$ cm^{-2}, d_{12}=5 nm z=0.2 nm and η=5 meV.

5.4 Coupled plasmon-SO phonon modes in double-layer phosphorene

Here, we consider a double-layer phosphorene with equal electron densities sandwiched by a homogeneous dielectric medium that models the substrate. It is reasonable to calculate the uncoupled plasmon modes before discussing the hybrid modes from the zeros of the determinant of the dielectric function matrix Eq. (5.6). In the leading-q approximation (long-wavelength limit), two plasmonic branches are obtained through the following relations [46]:

$$\omega_{ac}(q,\theta) = 2q\sqrt{\frac{n\pi e^2 d_{12}}{\epsilon_\infty}\frac{R_1(\theta)R_2(\theta)}{R_1(\theta)+R_2(\theta)}}. \tag{5.15}$$

$$\omega_{op}(q,\theta) = \sqrt{\frac{2n\pi e^2 q}{\epsilon_\infty}\big(R_1(\theta)+R_2(\theta)\big)}. \tag{5.16}$$

These two uncoupled branches are shown in Fig. 5.5(a) for $\theta = 0$ (along x direction) and in Fig. 5.5(b) for $\theta = \pi/2$ (along y direction) when SiO$_2$ is considered as a substrate/spacer [146, 46].

It can be seen that the plasmon modes experience a stronger reduction along y direction compared to x direction. For the case of electron-SO phonon coupling in double-layer phosphorene, we find two acoustic phonon-like modes, $\omega^{\lambda}_{ac(+)}$, with λ=1,2 and one acoustic plasmon-like mode, $\omega_{ac(-)}$ (see appendix B). The long-wavelength dispersions of the acoustic modes can be written as:

$$\omega^{\lambda}_{ac(+)}(q,\theta) = \omega^{\lambda}_{SO}\sqrt{1+\frac{4n\pi d_{12}e^2q^2\alpha e^{-2qz}}{(\omega^{\lambda}_{SO})^2\epsilon_\infty}\frac{R_1(\theta)R_2(\theta)}{R_1(\theta)+R_2(\theta)}}, \tag{5.17}$$

$$\omega_{ac(-)}(q,\theta) = 2q\sqrt{\frac{n\pi e^2 d_{12}(1-\alpha e^{-2qz})}{\epsilon_\infty}\frac{R_1(\theta)R_2(\theta)}{R_1(\theta)+R_2(\theta)}}. \tag{5.18}$$

In the same vein, we obtain two optical phonon-like modes, $\omega^{\lambda}_{op(+)}$, and one optical plasmon-like mode, $\omega_{op(-)}$ as

$$\omega^{\lambda}_{op(+)}(q,\theta) = \omega^{\lambda}_{SO}\sqrt{1+\frac{2n\pi e^2 q\alpha e^{-2qz}}{(\omega^{\lambda}_{SO})^2\epsilon_\infty}\big(R_1(\theta)+R_2(\theta)\big)}, \tag{5.19}$$

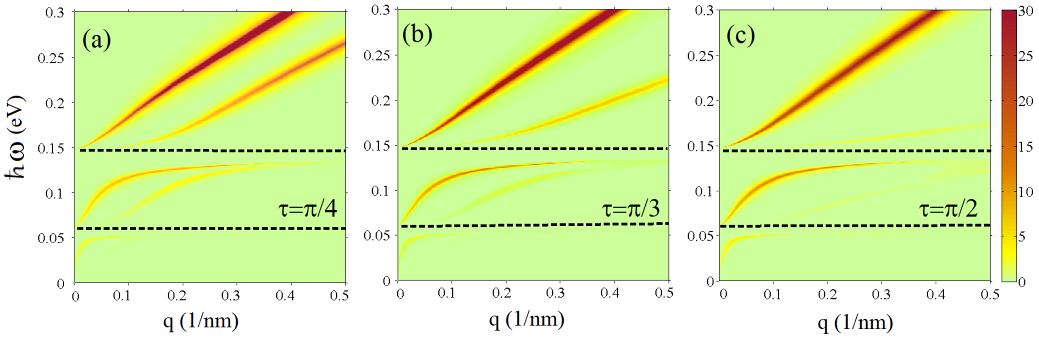

Figure 5.6: Effect of changing rotation angle on the loss function, $|-\Im[1/\varepsilon(\omega,q)]|$, for double-layer phosphorene sandwiched by $\mathrm{SiO_2}$ in (ω, q) space along $\theta = 0$ ($q \parallel x$) for $\tau_1 = 0$ and (a) $\tau_2 = \pi/4$, (b) $\tau_2 = \pi/3$ and (c) $\tau_2 = \pi/2$ with $\mathrm{d}_{12} = 5$ nm, $n = 1 \times 10^{13}$ cm^{-2} and z=0.2 nm.

$$\omega_{op(-)}(q,\theta) = \sqrt{\frac{2n\pi e^2 q(1-\alpha e^{-2qz})}{\epsilon_\infty}\big(R_1(\theta)+R_2(\theta)\big)}. \tag{5.20}$$

The behavior of the coupled modes with $\mathrm{SiO_2}$ as substrate/spacer is presented in Figs. 5.5(c) and 5.5(d) for $\theta = 0$ and $\theta = \pi/2$, respectively. The dispersion relations of the $\omega_{op/ac(-)}$ modes resemble the uncoupled acoustic and optical plasmon modes with an additional $(1-\alpha e^{-2qz})^{1/2}$ multiplier which makes these coupled modes lie below the uncoupled ones. Similar to the case of phosphorene monolayer, the hybrid plasmon-SO phonon frequencies along $q \parallel x$ are larger than along $q \parallel y$ because the carriers along y direction have larger mass and so get damped faster. One can also see that the uncoupled plasmon modes for $q \parallel y$ lie lower than ω_+^2 and therefore plasmon-SO phonon coupling along y direction is substantially weaker compared to the x direction.

In order to understand how the orientation parameter, $R_i(\theta)$, impacts the behavior of hybrid plasmon-SO phonon modes in the double-layer system, we show three cases in which $\tau_1 = 0$ and τ_2 progressively increases from $\pi/4$ to $\pi/3$ and to $\pi/2$ along x direction and for substrate/spacer $\mathrm{SiO_2}$ in Fig. (5.6). One may notice that, in general, with the reduction of τ_2, the coupled plasmon-SO phonon modes become significantly stronger because the hybrid modes are larger along the lower mass direction, *i.e.* $\theta = 0$. Furthermore, it is clear that the three acoustic plasmon/phonon-like modes

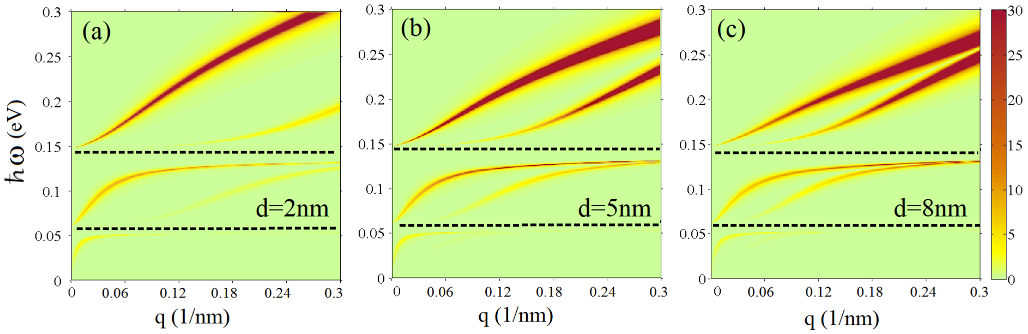

Figure 5.7: Effect of changing separation between layers on the loss function, $|-\Im[1/\varepsilon(\omega,q)]|$, for two parallel phosphorene monolayers sandwiched by SiO_2 in (ω,q) space along $\theta=0$ $(q \parallel x)$ for (a) $d_{12}=2$ nm (b) d_{12}=5 nm and (c) d_{12}=8 nm with $n=1\times10^{13}$ cm^{-2} and z=0.2 nm.

are very sensitive to the rotation of layers and get damped as the angle of rotation is increased. Finally, we address the effect of separation between layers, d_{12}, on the coupled modes along x direction in Fig. (5.7) for the substrate/spacer SiO_2. Here, increasing the separation between layers shows a similar effect on hybrid mode frequencies as the reduction of rotation angle τ_2 (see Fig. 5.6). As expected, the hybrid acoustic branches, similar to the uncoupled ones, depend strongly on the separation between layers at long-wavelengths and move to the optical branches by increasing the layers' spacing. As a result, by adjusting two parameters τ_2 and d_{12}, the acoustic branches may get strongly damped or a transition to the optical modes may be observed.

5.5 Conclusion

In summary, we have considered monolayer and double-layer phosphorene systems located on polar substrates/spacers and derived the anisotropic coupled plasmon-SO phonon dispersion relations in the long wavelength limit. Here, the dynamical dielectric function is calculated within the RPA and including many-body electron-electron interaction in phosphorene layer(s) as well as the interaction between electrons and the long range electric field generated by SO phonon modes. In the case of monolayer, due to the two relevant SO phonon modes of the substrate, three hybrid plasmon-SO phonon branches are obtained. It is shown that the hybrid plasmon-SO phonon modes are stronger along x direction because of lower corresponding effective mass and at large electron densities, these modes are stronger especially along x direction. Exploring the effects of specific substrates on the coupled modes showed that the phonon frequency (ω_{SO}) of a substrate is the most effective parameter in phonon-like modes (ω_+^λ) whereas the α parameter changes the plasmon-like mode, ω_-. Hence the choice of substrate can be utilized in order to engineer the plasmon-SO phonon dispersion phosphorene systems.

Also, analytical expressions for the hybrid modes at the long wavelength limit have been derived for double-layer phosphorene. The results showed that there are six hybrid modes: three acoustic, $(\omega_\pm)_{ac}$, and three optical modes, $(\omega_\pm)_{op}$. By evaluating the energy loss function, it was found that similar to the case of monolayer phosphorene, all plasmon-SO phonon modes are stronger along x direction than the modes along y direction. The effect of misalignment of the two layers on the hybrid modes has been also investigated and found that the acoustic branches may become strongly damped or a transition to the optical modes can be observed in at small rotations. Finally, the hybrid modes of double-layer phosphorene was studied for several inter-layer separations and a transition to the optical modes (fast damping excitations) by increasing (decreasing) of d_2 is observed for the acoustic modes. As a result of our calculations, rotation angle and separation between two layers can be used as a mechanism for tuning the effects of the plasmon-SO phonon coupling.

Chapter 6

Plasmon modes under applied uniaxial strain

> "Can plasmon modes of BP be affected by an applied uniaxial tensile strain?"

In this chapter[1], we study the effects of an applied in-plane uniaxial strain on the plasmon dispersion of monolayer, bilayer and double-layer phosphorene structures in the long-wavelength limit within linear elasticity theory. In the low energy limit, these effects can be modeled through the change in the curvature of the anisotropic energy band along the armchair and zigzag directions. We derive analytical relations for the plasmon modes under uniaxial strain and show that the direction of the applied strain is important. Moreover, we observe that along the armchair direction, the changes of the plasmon dispersion with strain are different and larger than those along the zigzag direction. For the two-layer phosphorene systems, we find that the relative orientation factor of the two layers can be used to control the plasmon energy. Furthermore, our study shows that the plasmon collective modes are more affected when the strain is applied equally to the layers as compared to the case in which the strain is applied asymmetrically to the layers. We also

---

[1] The results of this chapter were accepted to Journal of Applied Physics 123, 174301 (2018).

Table 6.1: Physical parameters of phosphorene under uniaxial strain along armchair and zigzag edges.

	x-axis	y-axis
u' (eV)	0.33	0.19
δ' (eV)	2.15	2.91
χ' (eV$\mathring{A}$)	-2.96	3.43
η'_x (eV$\mathring{A}^2$)	1.21	-0.45
η'_y (eV$\mathring{A}^2$)	-0.45	0.89
γ'_x (eV$\mathring{A}^2$)	2.37	-3.81
γ'_y (eV$\mathring{A}^2$)	-3.81	3.81

calculate the effect of strain on the drag resistivity in a double-layer phosphorene structure. The changes in the plasmon excitations due to an applied strain are mainly responsible for the predicted changes in the drag resistivity. This study can be easily extended to other anisotropic two-dimensional materials.

6.1 Introduction

BP is the most stable allotrope form of crystalline phosphorus and is a layered van der Waals (vdW) material like graphite. BP is a semiconductor with a puckered orthorhombic structure offering highly anisotropic optical and electronic properties [43, 32, 40, 113]. Few-layer BP has the unique feature that its direct bandgap deceases exponentially from 2 to 0.35 eV as the number of layers increases from monolayer to its bulk form. This property allows layer-engineering to tune the electronic bandgaps and light absorption spectra of BP.

This structure, with no surface dangling bonds withstands high deformation without breaking. Strain engineering, a recently developed and widely adopted technique, is capable of changing the electronic and optical properties of BP. The band structure of this novel material is highly sensitive to an applied strain and is highly deformable [147], making it a good potential candidate for electro-mechanical applications [38, 148]. While silicon typically breaks at strain level of 1.5 % [149] and MoS_2 gets folded and wrinkled by tensile strain of about 10 % [150, 151], monolayer BP (phosphorene) is able to withstand a surface tension and tensile strain up to 10 N/m and 30 %, respectively [38, 152, 147, 23, 55, 153].

Plasmons, the collective excitations of the oscillating charges have been extensively studied in graphene and other two-dimensional (2D) materials [154, 155, 156, 157]. It was shown that plasmon collective modes in graphene have relatively long propagation length [158, 159]. In a doped MoS_2 monolayer, as a result of a strong spin-orbit coupling, the plasmon modes are different from those in graphene-like materials and enter the electron-hole continuum region just similar to the case of 2D electron or hole gas with spin-orbit coupling [160, 161]. The effect of uniaxial strain on the dispersion relation of plasmons in graphene was investigated and a strain-induced anisotropic enhancement of the deviations from linearity of the transverse modes was obtained [162]. Also, the anisotropic collective excitations in pristine single-layer and multi-layer BP have been studied in the absence and presence of a magnetic or electric field [163, 164]. In the context of plasmons in layered BP, the effect of strain is one of the main issues that should be addressed. Particularly, it is interesting to explore the strain influence on the spatially separated double-layer phosphorene system in which the layers are coupled only via the long-range Coulomb interaction and the system exhibits a rich variety of phenomena like Coulomb drag [165]. The interaction-induced Coulomb drag transresistivity in phosphorene double-layer, that was recently investigated [47], is attractive because of its dependence on the plasma oscillations and sensitivity to the structural anisotropy of the system.

In this chapter, we theoretically investigate the effects of an applied uniaxial strain on the plasmon dispersion of monolayer, double-layer and bilayer phosphorene structures within linear elasticity theory. We calculate the strain-dependent dynamic dielectric function within the RPA and obtain the plasmon dispersion relation in the long-wavelength limit. We show that the energy of the plasmon modes depends upon the applied strain through the resulting effective masses along the armchair (x-axis) and zigzag (y-axis) directions. In two-layer phosphorene systems, the relative orientation of the two layers controls the plasmon frequencies. We also present numerical results for the effect of strain on the drag resistivity in a double-layer phosphorene structure and conclude that the changes in the plasmon excitation energies, due to applied strain, are mainly responsible for the predicted behaviors.

6.2 Strain-dependent electronic structure

We consider a system composed of phosphorene layers under externally applied strain.

The unit cell of monolayer phosphorene contains four phosphorus atoms which are stacked in puckered subplanes. In the tight-binding (TB) model, the Hamiltonian of the system is given as [166] $H_t = \sum_{i,j} t_{ij} c_i^\dagger(c_j)$, where t_{ij} represents the hoping between ith and jth sites and $c_i^\dagger(c_j)$ is the creation (annihilation) operator of electrons at site $i(j)$. A strain-dependent two-band TB Hamiltonian in the continuum approximation (retaining terms up to second order in k) and considering the linear deformation regime was obtained around the Γ point as [167, 148]

$$\hat{H}^s_{\mathbf{k}} = \begin{pmatrix} u^s + \eta^s_x k_x^2 + \eta^s_y k_y^2 & \delta^s + \gamma^s_x k_x^2 + \gamma^s_y k_y^2 + i\chi^s k_x \\ \delta^s + \gamma^s_x k_x^2 + \gamma^s_y k_y^2 - i\chi^s k_x & u^s + \eta^s_x k_x^2 + \eta^s_y k_y^2 \end{pmatrix}. \tag{6.1}$$

Here, only the uniaxial strains s_x, s_y and s_z along the three principle directions, namely, the x-axis, y-axis and also the direction normal to the phosphorene plane (z-axis) have been considered. Therefore, the changes of the components of the position vector are determined by $\mathbb{X}^s = (1 + s_{\mathbb{X}})\mathbb{X}$ where $\mathbb{X} = x, y$ and z. The strain-dependent parameters in the above TB Hamiltonian are related to the unstrained ones as $u^s = u + su'$, $\eta^s_x = \eta_x + s\eta'_x$, $\eta^s_y = \eta_y + s\eta'_y$, $\gamma^s_x = \gamma_x + s\gamma'_x$, $\gamma^s_y = \gamma_y + s\gamma'_y$ and $\chi^s = \chi + s\chi'$ where $u = 0.42$ eV, $\eta_x = 1.03$ eV$\mathring{A}^2$, $\eta_y = 0.56$ eV$\mathring{A}^2$, $\delta = 0.76$ eV, $\gamma_x = 3.51$ eV$\mathring{A}$, $\gamma_y = 3.81$ eV$\mathring{A}^2$ and $\chi = -5.34$ eV$\mathring{A}$. In Table 6.1, we list the calculated parameters of the TB Hamiltonian matrix elements for a phosphorene monolayer under uniaxial strain [148]. Applied strain can, in fact, affect the inter-band coupling by changing the energy gap and χ^s. However, the relatively large bandgap of the phosphorene monolayer which results in a weak inter-band interaction, allows one to decouple the conduction and valence bands at small wave vectors. In this approximation, the phosphorene band structure is obtained as:

$$E^s_\pm(\mathbf{k}) \approx u^s + \eta^s_x k_x^2 + \eta^s_y k_y^2 \pm \left(\delta^s + \left[\gamma^s_x k_x^2 + \gamma^s_y k_y^2 + \frac{(\chi^s)^2}{2\delta^s} k_x^2\right]\right), \tag{6.2}$$

where $+(-)$ stands for the conduction (valence) band. Thus, the strain-

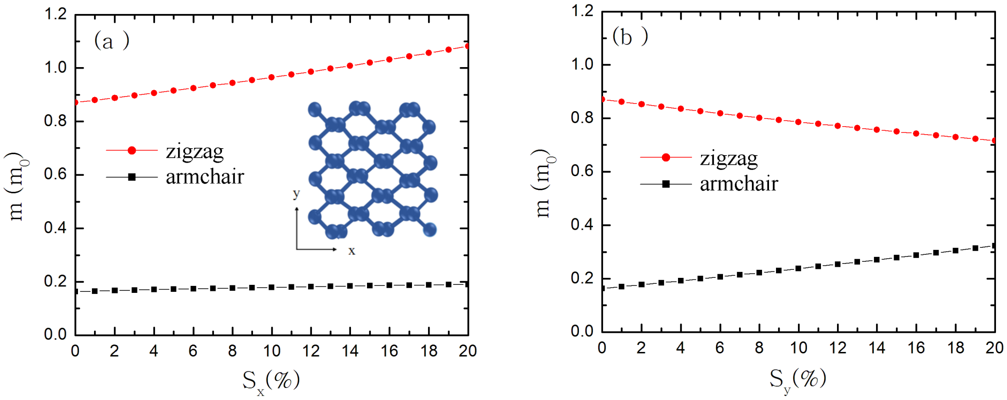

Figure 6.1: Effective masses along the armchair and zigzag directions of phosphorene as function of tensile strain applied along (a)x-axis (s$_x$) and (b) y-axis (s$_y$).

dependent electron and hole effective masses are given by

$$\begin{aligned} m^s_{ex} &= \frac{\hbar^2}{2(\eta^s_x + \gamma^s_x + (\chi^s)^2/2\delta^s)} \\ m^s_{ey} &= \frac{\hbar^2}{2(\eta^s_y + \gamma^s_y)} \\ m^s_{hx} &= \frac{\hbar^2}{2(\gamma^s_x - \eta^s_x + (\chi^s)^2/2\delta^s)} \\ m^s_{hy} &= \frac{\hbar^2}{2(\gamma^s_y - \eta^s_y)}. \end{aligned} \tag{6.3}$$

Considering only the conduction band and using the above strain-dependent electron effective masses along the armchair ($m^s_x = m^s_{ex}$) and zigzag directions ($m^s_y = m^s_{ey}$), we can obtain the following expression for the energy of the electrons [44, 167]

$$E^s(\mathbf{k}) = \frac{\hbar^2}{2}(\frac{k_x^2}{m^s_x} + \frac{k_y^2}{m^s_y}). \tag{6.4}$$

The calculated strain-dependent electron effective masses of phosphorene as functions of s_x and s_y are depicted in Figs. 6.1(a) and (b). The inset figure is the top view of monolayer phosphorene. In a relaxed (unstrained) phosphorene monolayer system, the electron effective mass is predicted to be 0.168m$_0$ in the armchair and 0.852m$_0$ in the zigzag directions [166]. The smaller electron effective mass along the armchair direction results in a favorable transport direction in phosphorene. We show that when applying uniaxial strain along x-axis, the effective mass in the armchair direction is almost insensitive to the strength of the applied strain while along the zigzag direction, it increases notably with strain. These behaviors are direct consequences of the effect of strain on the band structure and atomic orbitals of phosphorene [55]. In the case of strain applied parallel to the y-axis, the effective mass along the armchair (zigzag) direction increases (decreases). Since we used the one-band model, there are no sharp changes in the effective masses due to the direct-indirect band gap transition (see Fig. 6.1) [55].

6.3 Plasmons under uniaxial strains

In order to study plasmonic collective modes, we need to calculate the dielectric function $\epsilon_s(q,\omega)$ of the system. Within linear-response theory, plasmon modes are defined as the zeros of the dielectric function. The RPA is the simplest diagrammatic procedure to include the electron correlations in the dielectric function. It is well-known that RPA gives the exact dielectric function in the limit of infinite electron density. As a result, it makes sense to employ the RPA to calculate the dielectric function at high electron density. The strain-dependent RPA dielectric function matrix for a few-layer system in the absence of inter-layer tunneling is given by [66, 168]

$$\epsilon^s_{ij}(\mathbf{q},\omega) = \delta_{ij} + V_{ij}(q)\Pi^s_i(\mathbf{q},\omega), \tag{6.5}$$

where $V_{ij}(q) = \nu(q)\exp(-qd(1-\delta_{ij}))$ is the unscreened 2D Coulomb interaction with d being the separation between layers and $\nu(q) = 2\pi e^2/q\kappa$, where κ being the average dielectric constant. The non-interacting polarization function of ith layer can be obtained through the following equation [62]:

$$\Pi^s_i(\mathbf{q},\omega) = -\frac{2}{A}\sum_{\mathbf{k}} \frac{f^0(E^s_i(\mathbf{q})) - f^0(E^s_i(\mathbf{k}+\mathbf{q}))}{E^s_i(\mathbf{q}) - E^s_i(\mathbf{k}+\mathbf{q}) + \hbar\omega + i\xi}. \tag{6.6}$$

Here, A denotes the area of the unit cell, $f^0(E^s_i(\mathbf{q}))$ is the Fermi distribution function of layer i at strain-modified energy E^s_i corresponding to a 2D wave vector $\mathbf{q}$ and ξ being the broadening parameter which accounts for disorder in the system. In a phosphorene monolayer, the temperature-dependent dynamic polarization function for the intra-band transition has been calculated by making use of the anisotropic parabolic energy dispersion relation (Eq. (6.4)) as [44, 47]:

$$\frac{\Pi_i^s(\mathbf{q},\omega)}{g_{2d}^s} = -\int dK \frac{\Phi_i^s(K,T)}{Q}\left[sgn(\Re(Z_-))\frac{1}{\sqrt{Z_-^2-K^2}} - sgn(\Re(Z_+))\frac{1}{\sqrt{Z_+^2-K^2}}\right]. \tag{6.7}$$

In the above, we defined $\mathbf{K}(\mathbf{Q}) = \sqrt{m_d^s/\hat{M}^s}(\mathbf{k}(\mathbf{q})/k_F)$, where $\hat{M}^s$ is the strain-dependent mass tensor with diagonal elements m_x^s and m_y^s and $m_d^s = \sqrt{m_x^s m_y^s}$ is the 2D density of states mass. Here, $k_F = \sqrt{2\pi n}$ is the Fermi wave vector, n being the electron density, $\mathbf{q} = q(\cos\theta, \sin\theta)$, $g_{2d}^s = m_d^s/\pi\hbar^2$ and the rotational angle, τ_i, is defined as the angle between x-axis in the laboratory frame and x direction of the ith layer. So, we can write $Q = q\sqrt{m_d^s R_i^s(\theta)}/k_F$ in which the strain-dependent orientation factor, $R_i^s(\theta)$, is expressed as:

$$R_i^s(\theta) = \left(\frac{\cos^2(\theta-\tau_i)}{m_x^s} + \frac{\sin^2(\theta-\tau_i)}{m_y^s}\right). \tag{6.8}$$

Moreover, in Eq. (6.7) we define $Z_\pm = ((\hbar\omega + i\xi)/\hbar Q \nu_F^s) \pm (Q/2k_F)$ with $\nu_F^s = \hbar k_F/m_d^s$ and Φ_i^s is given by:

$$\Phi_i^s(K,T) = \frac{K}{1+\exp[(K^2 E_{F,i}^s - \mu_i^s)/k_B T]}, \tag{6.9}$$

where $E_{F,i}^s$ and μ_i^s are the strain-dependent Fermi energy and chemical potential of layer i, respectively and they satisfy the following particle number conservation condition [63]:

$$E_{F,i}^s = \mu_i^s + k_B T \ln[1+\exp(-\mu_i^s/k_B T)]. \tag{6.10}$$

In the limit of long-wavelength where the plasmon excitations have relatively long lifetimes, the zero-temperature polarization function can be approximated as [43]:

$$\frac{\Pi_i^s(\omega,q,\theta)}{g_{2d}^s} \approx \frac{q^2}{\omega^2} R_i^s(\theta) E_{F,i}^s. \tag{6.11}$$

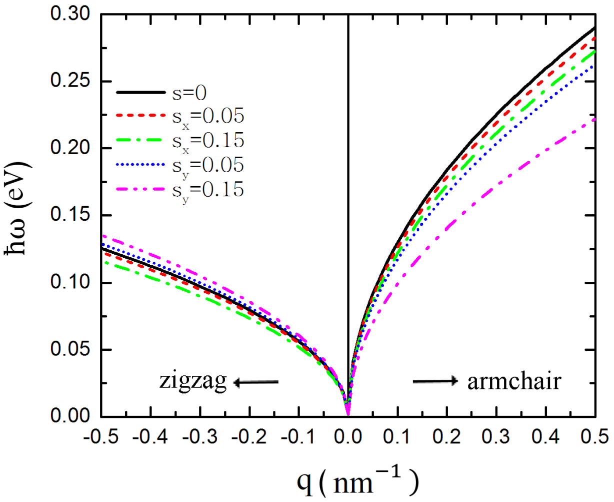

Figure 6.2: The plasmon dispersions in the unstrained and uniaxial tensile strained phosphorene monolayers along $x-$ and $y-$axis with $n = 1 \times 10^{13}\text{cm}^{-2}$. Here, the substrate is h-BN.

Thus, the long-wavelength plasmon dispersion relation of a phosphorene monolayer under uniaxial strain is obtained as

$$\omega_{pl}^{s}(q,\theta) = \sqrt{\frac{2n\pi e^2 R_i^s(\theta)q}{\kappa}}, \tag{6.12}$$

which depends on strain through the orientation factor. An important and useful feature of this formulation is that all the effects due to strain appear in the strain-dependent orientation factor $R_i^s(\theta)$ as a multiplicative modifier. Therefore, we recover the typical $\sqrt{q}$ dispersion of 2D plasmons and the strain effects are included in the effective masses. In Fig. 6.2, we show our numerical results for the strain-dependence plasmon modes in monolayer phosphorene along (a) armchair and (b) zigzag directions for a few applied uniaxial strains. For comparison, we also present numerical results for the case of relaxed system. Due to the peculiar behaviors of the effective masses under uniaxial strains along zigzag and armchair directions, plasmon modes behave differently along these directions. The energy of plasmon modes, $\hbar\omega_{pl}^{s}(q,\theta)$, along the armchair direction decreases with increasing the strength of the applied strain due to the effective mass enhancement along

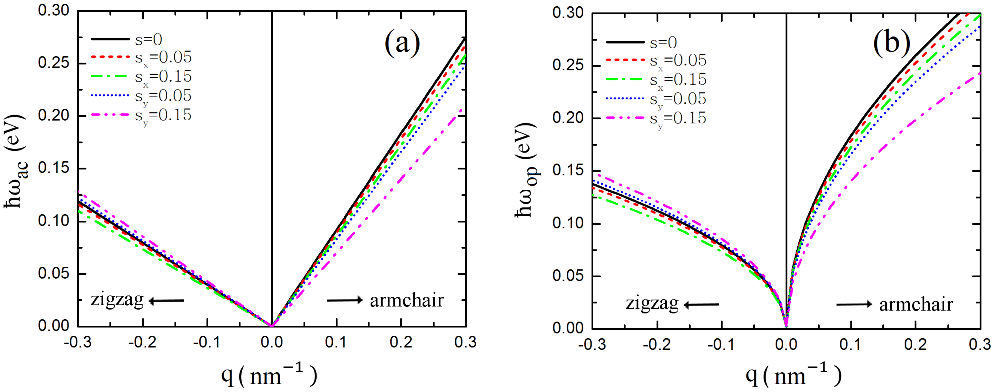

Figure 6.3: (a) Acoustic and (b) optical plasmon dispersions along armchair and zigzag directions of a double-layer phosphorene structure. Uniaxial tensile strain is applied along the $x-$ and y-axis with $n = 1 \times 10^{13}\text{cm}^{-2}$ and d =5 nm. The structure is sandwiched by h-BN.

this direction. However, as shown in Fig. 6.2, the effect of applied strain on the plasmon dispersion along the zigzag direction is different. It is important to notice that the energy of plasmon modes in the zigzag direction decreases (increases) with applied s_x (s_y) strain. This observation could be understood through the fact that the electron effective mass increases (decreases) with increasing s_x (s_y) along the zigzag direction (see Fig. 6.1). However, the effective mass along the armchair direction increases with increasing s_x and also s_y. It is worth pointing out that while the applied strain changes the energy of the plasmon modes, it does not alter the standard $\sqrt{q}$ dispersion behavior.

To show how uniaxial strain affects the plasmonic excitations in double-layer phosphorene, we solve Eq. (6.5) for a 2×2 matrix. Considering the long-wavelength limit and only the intra-band transition, there are two plasmonic branches, the so-called acoustic plasmons with q-linear behavior

$$\omega^s_{ac}(q,\theta) = 2q\sqrt{\frac{n\pi e^2 d}{\epsilon_\infty}\left(\frac{R^s_1(\theta)R^s_2(\theta)}{R^s_1(\theta)+R^s_2(\theta)}\right)}, \tag{6.13}$$

and optical plasmons with square-root dependence on q

$$\omega^s_{op}(q,\theta) = \sqrt{\frac{2n\pi e^2 q}{\epsilon_\infty}\big(R^s_1(\theta) + R^s_2(\theta)\big)}. \tag{6.14}$$

Although the optical mode, $\omega^s_{op}(q,\theta)$, corresponds to a collective excitation in which the electron densities in the two layers fluctuate in-phase and it is independent of the layer separation d for small wave vectors, the acoustic plasmon mode, $\omega^s_{ac}(q,\theta)$, accounts for an out-of-phase oscillation of the carriers in the two layers and depends on d. These branches are influenced by the strain through the strain-dependent orientation factor of the layers, $R^s_1(\theta)$ and $R^s_2(\theta)$. While these factors are combined together additively for the optical plasmon modes, they appear as a reduced form, similar to a reduced mass in the acoustic plasmon [46]. In Fig. 6.3, these modes have been illustrated for a few uniaxial strain values along the armchair and zigzag directions in phosphorene double-layer sandwiched by h-BN at an electron density $n = 1 \times 10^{13}$ cm^{-2} and with a separation distance $d = 5$ nm. When strain is applied to a double-layer system, both the optical and acoustic plasmon modes decrease along the armchair direction. However, these plasmon branches exhibit a long-wavelength behavior similar to the zigzag direction of plasmon dispersion in monolayer phosphorene under uniaxial strain.

It is appealing to model bilayer phosphorene itself by reducing the separation down to $d = 0.5$ nm. Therefore, we use the general low-energy model of anisotropic double-layer systems (see Eq. 6.4) without the inter-layer hopping of electrons. The plasmon modes of the relaxed and strained bilayer phosphorene are shown in Fig. 6.4 where an effective dielectric constant of ~ 2 (for a common h-BN substrate and air spacer) and an inter-layer distance of $d = 0.5$ nm are considered. More interestingly, due to the weak vdW interaction between phosphorene layers, the plasmon modes of our suggested bilayer phosphorene with no strain are consistent with the results have been previously obtained in the long-wavelength limit in Ref. [45]. Plasmon modes that were studied by using a TB model for a bilayer phosphorene in which the inter-layer hopping of electrons was allowed. As expected, the acoustic modes in the bilayer structure are much weaker as compared to the acoustic modes of the double-layer system because of the shorter distance between the two layers. Also, under uniaxial strain, the behavior of the optical and acoustic modes of the bilayer system is similar to the case of double-layer phosphorene along both the armchair and zigzag directions. For the strained

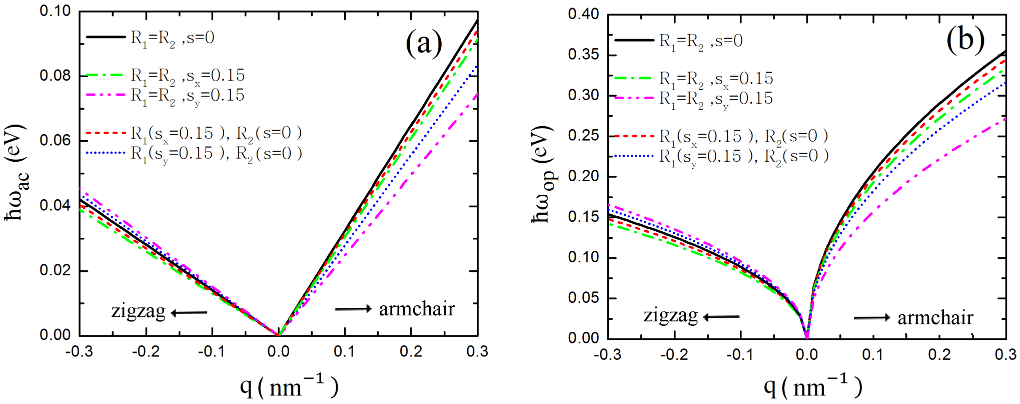

Figure 6.4: (a) Acoustic and (b) optical plasmon dispersions along armchair and zigzag directions in bilayer phosphorene. Uniaxial tensile strain is applied along the $x-$ and $y-$axis with $n = 1 \times 10^{13}\text{cm}^{-2}$ and $d = 0.5$ nm. The effective dielectric constant of ~ 2 (h-BN as substrate and air as spacer is used).

bilayer structure, we investigate two different cases: *i*) strain equally applied to the two layers, $R_1(s) = R_2(s)$, and *ii*) strain applied only to one of the layers, $R_1(s \neq 0)$ and $R_2(s = 0)$. The qualitative difference between these two cases is apparent in Fig. 6.4. As can be observed, the effect of strain on the long-wavelength plasmon energies in case *i*) is stronger than the case *ii*).

6.4 Transresistivity of phosphorene under strain

In this section, we study the transresistivity in a double-layer phosphorene under strain. It is well-known that plasmon modes contribute strongly to the momentum transfer phenomenon in Coulomb coupled electron gas systems [90, 169]. The transresistivity matrix for an anisotropic double-layer system which was recently proposed [47] is given by

$$\rho^s_{\alpha\beta} = \frac{\hbar^2}{(2\pi)^3 e^2 n_1 n_2 k_B T} \int \mathrm{d}q \int_0^\infty \mathrm{d}\omega F^s_{\alpha\beta}(q, \omega, T), \tag{6.15}$$

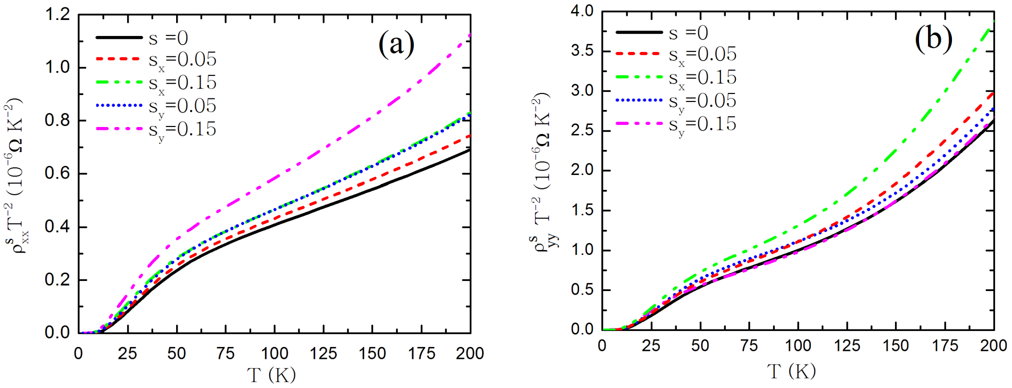

Figure 6.5: Scaled drag resistivity for a few values of tensile uniaxial strain along (a) armchair and (b) zigzag directions in a double-layer phosphorene sandwiched by h-BN with $d = 5$ nm.

where n_1 and n_2 are the electron densities in layers 1 and 2, α and β denote the Cartesian coordinates (x and y) and $F^s_{\alpha\beta}(q,\omega,T)$ is defined as:

$$F^s_{\alpha\beta}(q,\omega,T) = \int_0^{2\pi} d\theta \psi_{\alpha\beta}(\theta,\tau_1,\tau_2)\frac{q^3}{\sinh^2(\hbar\omega/2k_BT)}|U^s_{12}(q,\omega,T;\theta,\tau_1,\tau_2)|^2 \times \Im\Pi^s_1(q,\omega,T;\theta,\tau_1)\Im\Pi^s_2(q,\omega,T;\theta,\tau_2), \tag{6.16}$$

with $\psi^{\alpha\beta}$ given by

$$\psi^{\alpha\beta}(\theta,\tau_1,\tau_2) = \begin{cases} \cos(\theta-\tau_1)\cos(\theta-\tau_2), & \alpha=\beta=x \\ \sin(\theta-\tau_1)\sin(\theta-\tau_2), & \alpha=\beta=y \\ \cos(\theta-\tau_1)\sin(\theta-\tau_2), & \alpha=x,\beta=y. \end{cases} \tag{6.17}$$

The strain-dependent dynamically screened inter-layer potential $U^s_{12}(q,\omega,T;\theta,\tau_1,\tau_2) = U^s_{12}(\mathbf{q},\omega)$ can be obtained from [65]:

$$U^s_{12}(\mathbf{q},\omega) = \frac{V_{12}(q)}{det|\epsilon^s_{12}(\mathbf{q},\omega)|}, \tag{6.18}$$

where $det|\epsilon^s_{ij}(\mathbf{q},\omega)|$ is the determinant of the general dielectric matrix, Eq. (6.5). In Fig. 6.5, we show the diagonal elements of the transresistivity tensor calculated within the RPA versus temperature for two parallel aligned phosphorene monolayers sandwiched by h-BN layers and separated by a distance of $d = 5$ nm. It can be seen that the values of ρ^s_{yy} is larger than ρ^s_{xx} in the studied range of temperatures. This is a consequence of a higher electron effective mass (Fig. 6.1) which results in lower excitation energies for the acoustic and optical branches (Fig. 6.3), and thus in a larger contribution of plasmon modes to the momentum transfer phenomenon. Also, as a general result, the transresistivity is mainly influenced by the strain in such a way that it increases by increasing the applied strain. According to the results shown in Fig. 6.5, the effect of uniaxial strain on the transresistivity is stronger for higher temperatures. In the case of ρ^s_{xx}, the drag resistivity shows a neat correlation with the plasmon modes when s_x or s_y is applied. On the other hand, although, the unstrained ρ^s_{yy} has still smaller values than the strained one, it does not really follow the trend of the plasmon modes with applied s_y. We think that in this case, the effect of applied strain on the single-particle contribution to the drag resistivity dominates the strain effect on the plasmons, which results in a different behavior.

6.5 Conclusion

In this chapter, we have studied the effect of an applied uniaxial tensile strain on the plasmon dispersion of monolayer, bilayer and double-layer phosphorene structures. As a consequence of the anisotropic energy band, the changes in the plasmon dispersions are different along the armchair and zigzag directions and depend strongly on the direction of the applied uniaxial strain. Also, in the two-layer phosphorene systems, it was shown that the strain-dependent orientation factor of the layers controls the variations in the plasmon energies. In addition, we have obtained that while the behavior of the optical and acoustic modes are similar in both bilayer and double-layer phosphorene, plasmons along the armchair direction are more affected by strain. Moreover, for the strained bilayer structure, two different cases have been investigated: *i*) strain equally applied to the two layers, and *ii*) strain applied only to one of the layers. We found that the effect of strain on the long-wavelength plasmon modes in case *i*) is stronger than for case *ii*). Finally, the diagonal elements of the transresistivity tensor have been calculated within the RPA for a double-layer phosphorene in which two parallel aligned phosphorene monolayers are under strain and sandwiched by h-BN.

The results suggested that the changes in the plasmonic excitations, due to the applied strain, are mainly responsible for the predicted behaviors of the drag resistivity.

Chapter 7

Electron-hole superfluidity

"How does excitonic superfluidity occur in a electron-hole double-layer phosphorene at zero temperature ?"

We study excitonic superfluidity at zero temperature in the electron-hole double layer phosphorene system by using an anisotropic effective mass in the free-electron model. Highly anisotropic superfluidity is predicted where the magnitude of the gap function is not only momentum dependent, but also depends on the direction of **k**. Meanwhile, the peak around the maximum gap (Δ_{max}) is located in the BEC regime along the armchair direction and in the BCS-BEC crossover regime along zigzag direction. We calculate an estimated highest Kosterlitz-Thouless transition temperature with maximum value up to $\sim$ 90K in double layer phosphorene along the zigzag direction with carrier densities as high as 4×10^{12} cm^{-2}. We highlight in this work that the in-plane anisotropy plays an important role in superfluidity where in a special direction there is a transition to strongly correlated states. Our results may guide future experimental research towards the realization of anisotropic condensate states in coupled 2D devices.

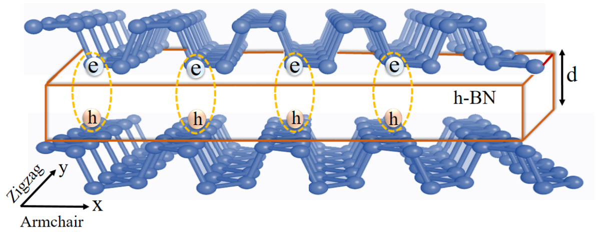

Figure 7.1: Schematic illustration of two phosphorene sheets separated by a thin barrier of h-BN layers. The electrons and holes are induced in the separately electrically contacted upper and lower phosphorene sheets by top and back gates.

7.1 Introduction

Phosphorene is unstable in air [170, 171] and therefore encapsulation with hexagonal boron nitride (h-BN) is used to make devices which are conductive and fully stable under ambient conditions [172, 30]. There has been an increasing interest in the study of van der Waals heterostructures including 2D conducting sheets separated by thin h-BN insulating layers. The interest is mainly because these systems offer the possibility for the observation of a coherent superfluid state in spatially separated electron- and hole-doped conducting sheets driven by the strong inter-layer Coulomb interaction. Unlike conventional double-GaAs quantum well structures, which typically have inter-layer electron-hole separation larger than the effective Bohr radius, the separation between the electron-hole sheets in 2D van der Waals heterostructures [1], can be as small as 1 nm (i.e. three h-BN layers) and still provide a potential barrier high enough to suppress inter-layer tunneling. This leads to a strong inter-layer coupling, boosting the onset of superfluidity. Electron-hole superfluidity has been studied in different double graphene systems, including monolayers [173], bilayers [174], few layers [8], nanoribbons [175] and hybrid graphene-GaAs quantum heterostructures [176]. Such systems may support a superflow of electron-hole pairs below the Kosterlitz-Thouless (KT) transition temperature. Except for the double electron-hole monolayer graphene system, in which a strong screening kills any superfluidity [173], multi-layer graphene systems show promising predictions for the observation of a condensate superfluid state.

In this chapter, we investigate the possibility of *anisotropic superfluid-*

ity in double electron-hole phosphorene sheets. We found that a highly anisotropic superfluid state occurs in double phosphorene sheets arising from the anisotropic low energy bands in phosphorene. Because of the anisotropic charge carrier effective mass along the armchair(x) and zigzag (y) directions, excitons in phosphorene are characterized by a strong spatial anisotropy and can exist at elevated temperatures with large binding energies [39, 177, 178]. Our system consists of two parallel monolayer phosphorene sheets. The upper sheet of electrons and the lower sheet of holes are controlled by the top and back gates, respectively. The two sheets are separated by a thin h-BN insulating barrier to prevent tunneling between the phosphorene sheets and thus prevent electron-hole recombination. The semiconductor nature of phosphorene with a large energy gap of $\sim 1.5 - 2$ eV leads to only very small contributions from the phosphorene valence band. Therefore, within our calculations we consider only contributions from the conduction band. We first extend the isotropic mean-field equations for the superfluid gap and superfluid density to the case of anisotropic energy bands considering static screened electron-hole Coulomb interaction. We calculate the superfluid energy gap and transition temperature to see whether a superfluid state can form in the double phosphorene system for experimentally attainable densities. We predict a highly anisotropic gap function and estimate an upper limit for the transition temperature that also depends on the direction of motion of the electron-hole pair, caused by the anisotropic band structure. Whereas phosphorene represents a good system to which we can apply our analysis, the approach outlined in this paper are given in the most general form to make them easily adaptable to other materials and can also be applied to other emerging anisotropic 2D materials.

7.2 Isotropic mean field equation

We employ a mean field approach in which the finite energy gap in the excitation spectrum of the system $\Delta(\boldsymbol{k})$, is a signature of the superfluid ground state. For a system with equal density of electrons and holes $n_e = n_h = n$, the pair excitation energy and the equation for the momentum dependent gap function are, respectively [179]

$$E(\boldsymbol{k}) = \sqrt{\xi^2(\boldsymbol{k}) + \Delta^2(\boldsymbol{k})}, \tag{7.1}$$

$$\Delta(\boldsymbol{k}) = -\frac{1}{\Omega}\sum_{\boldsymbol{q}} V(q)\frac{\Delta(\boldsymbol{k}-\boldsymbol{q})}{2E(\boldsymbol{k}-\boldsymbol{q})}, \tag{7.2}$$

and the mean field equation for the electron(hole) density is given by:

$$n = \frac{g_s}{\Omega}\sum_{\boldsymbol{k}'}\frac{1}{2}(1-\frac{\xi(\boldsymbol{k}')}{E(\boldsymbol{k}')}), \tag{7.3}$$

where Ω is the surface area of the system, $\xi(\boldsymbol{k}) = [\xi^e(\boldsymbol{k}) + \xi^h(\boldsymbol{k})]/2$ with $\xi^{e/h}(\boldsymbol{k})$ energy of electrons and holes measured from the chemical potential μ and $g_s = 2$ is the spin degeneracy. The screened Coulomb interaction $V(q)$, between electron(e) and hole(h) layers in the random phase approximation (RPA) is given by [180]:

$$V(q) = \frac{v_d + \Pi_a(v_q^2 - v_d^2)}{1 + 2(v_q\Pi_n + v_d\Pi_a) + (v_q^2 - v_d^2)(\Pi_n^2 - \Pi_a^2)}. \tag{7.4}$$

Here $v_q = -2\pi e^2/\kappa q$ and $v_d = v_q \exp(-qd)$ are, respectively, the intra-layer and inter-layer Coulomb interaction screened by a surrounding medium with dielectric permitivity κ. Here we set $\kappa = 3$ which is the dielectric constant of h-BN. Π_n and Π_a are the normal and anomalous polarization, respectively, which within the RPA are given by [66, 181]

$$\Pi_n(\boldsymbol{q}) = -g_s\sum_{\boldsymbol{k}}\frac{u^2(\boldsymbol{k})\nu^2(\boldsymbol{k}-\boldsymbol{q}) + \nu^2(\boldsymbol{k})\; u^2(\boldsymbol{k}-\boldsymbol{q})}{E(\boldsymbol{k}) + E(\boldsymbol{k}-\boldsymbol{q})}, \tag{7.5}$$

$$\Pi_a(\boldsymbol{q}) = g_s\sum_{\boldsymbol{k}}\frac{2u(\boldsymbol{k})\nu(\boldsymbol{k}-\boldsymbol{q})\nu(\boldsymbol{k})\; u(\boldsymbol{k}-\boldsymbol{q})}{E(\boldsymbol{k}) + E(\boldsymbol{k}-\boldsymbol{q})}, \tag{7.6}$$

where $u(\boldsymbol{k})$ and $\nu(\boldsymbol{k})$ are the coherence factors given by [182]

$$u^2(\boldsymbol{k}) = \frac{1}{2}(1+\frac{\xi(\boldsymbol{k})}{E(\boldsymbol{k})}), \quad \nu^2(\boldsymbol{k}) = \frac{1}{2}(1-\frac{\xi(\boldsymbol{k})}{E(\boldsymbol{k})}). \tag{7.7}$$

We note that $u(\boldsymbol{k})\nu(\boldsymbol{k}) = \Delta(\boldsymbol{k})/2E(\boldsymbol{k})$. The most favorable conditions for pairing occurs when $k_F d \gg 1$. In this limit, Eq. (7.4) can be approximated as [174, 8]

$$V(q) \approx \frac{v_q \exp(-qd)}{1 + 2v_q(\Pi_n[\boldsymbol{q}) + \Pi_a(\boldsymbol{q})]}. \tag{7.8}$$

7.3 Anisotropic mean field equations

Here, we extend the mean field equations (7.2) and (7.3) to the case of e-h phosphorene sheets where the energy bands are anisotropic. Here we use the effective masses $m_x^e = m_x^h \approx 0.15m_0$ and $m_y^e \approx 0.7m_0$ and $m_y^h \approx 1.0m_0$ (m_0 is the free electron mass) [64]. Because phosphorene is a semiconductor with a direct band gap at the Γ point of the first Brillouin zone [33], inter-band transitions require extremely large energies. Therefore, we include only one band and limited ourselves to contributions from the conduction band of each layer. In this case, we use equal effective masses for the e and h in each phosphorene sheet, so that we drop out the e and h indices. Here, to get rid of the anisotropy, we use the following transformation [44] $\boldsymbol{s} = \sqrt{m_D/M}\boldsymbol{q}$ and $\boldsymbol{p} = \sqrt{m_D/M}\boldsymbol{k}$. We consider $\boldsymbol{k} = k(\cos(\theta), \sin(\theta))$ where θ is the polar angle of the $\boldsymbol{k}$ vector with respect to the x axis. So, we can rewrite $p(\theta) = k\sqrt{m_d R(\theta)}$ in which the orientation factor $R(\theta) = \cos^2(\theta)/m_x + \sin^2(\theta)/m_y$ [46]. Using this simplified notation, the anisotropic energy $\xi(\boldsymbol{k})$ term (Eq. 2.10) becomes:

$$\xi(\boldsymbol{p}) = \frac{\hbar^2 p^2}{2m_d} - \mu. \tag{7.9}$$

Having this quadratic energy dispersion, we generalize the well-known analytical form of the polarizability to include anisotropy in the superfluid gap. Therefore, the zero temperature total polarization function can be calculated by using the renormalized isotropic energy bands Eq. (7.9) within the calculation of Eq. (7.5) for the normal polarization function

$$\Pi_n(\boldsymbol{s}) = -g_s \sum_{\boldsymbol{p}} \frac{u^2(\boldsymbol{s})\nu^2(\boldsymbol{p}-\boldsymbol{s}) + \nu^2(\boldsymbol{p})u^2(\boldsymbol{p}-\boldsymbol{s})}{E(\boldsymbol{p}) + E(\boldsymbol{p}-\boldsymbol{s})}, \tag{7.10}$$

and in Eq. (7.6) for the anomalous polarization function

$$\Pi_a(\boldsymbol{s}) = g_s \sum_{\boldsymbol{p}} \frac{2u(\boldsymbol{p})\nu(\boldsymbol{p}-\boldsymbol{s})\ \nu(\boldsymbol{p})u(\boldsymbol{p}-\boldsymbol{s})}{E(\boldsymbol{p}) + E(\boldsymbol{p}-\boldsymbol{s})}. \tag{7.11}$$

Using the polar notation, one can readily obtain the superfluid gap equation as

$$\Delta(\boldsymbol{p}) = -\frac{1}{\Omega} \sum_{\boldsymbol{p}'} V(\boldsymbol{p}-\boldsymbol{p}') \frac{\Delta(\boldsymbol{p}')}{2E(\boldsymbol{p}')}, \tag{7.12}$$

and the density equation

$$n = \frac{g_s}{\Omega} \sum_{\boldsymbol{p'}} \frac{1}{2}(1 - \frac{\xi(\boldsymbol{p'})}{E(\boldsymbol{p'})}). \tag{7.13}$$

7.4 Results an discussions

In this section, we present and discuss our numerical results for the superfluidity of the double-layer phosphorene. Here we solve Eqs. (7.10)-(7.13) self-consistently for the direction-dependent $\Delta(\boldsymbol{k})$. The separation of few nanometers between electron and hole sheets can be achieved in the 2D e-h double-layer systems making them good candidates for the observation of superfluidity [174, 8]. Fig. (7.2) shows the maximum of the superfluid gap Δ_{max} as a function of density for different interlayer separations d and for both (a) armchair ($\theta = 0$) and (b) zigzag ($\theta = \pi/2$) directions of phosphorene. It is important to note that, although with decreasing d the pairing interaction in the two directions become stronger and the superfluidity persists up to a higher onset density, n_c, but the maximum of the gap function, Δ_{max}, is about twice larger along zigzag than armchair direction for the same d. This effect can be understood by recalling the fact that the larger effective mass results in a significant enhanced exciton e-h binding energy. Indeed, the localized excitons happen when the effective mass is large and the dielectric constant is small. Therefore, in the zigzag direction the interactions are stronger than in the armchair direction, leading to more localized pairs, and this further reduces the effectiveness of screening. We use the one band model in which the e-h (exciton) mass ratio is fixed to unity. When the mass anisotropies of e and h are different, the Fermi surfaces for the conduction and valence bands will be different. Then the effective mass anisotropy results in the disappearance of the exciton state because excess energy is needed to create e–h pairs.

The distinction between BEC and BEC-BCS crossover regime is shown in Fig. (7.2). This separation can be estimated by the condensate fraction, $C_F = \sum_{\boldsymbol{k}} u^2(\boldsymbol{k})v^2(\boldsymbol{k}) / \sum_{\boldsymbol{k}} v^2(\boldsymbol{k})$, which describes the number of Bose-condensed particles at $T = 0$ [8]. It is shown that due to the fact $C_F > 0.8$ the peak around the maximum gap Δ_{max} is located in the BEC regime along the armchair direction and it is in the crossover from exciton BEC at low densities to the BCS-like condensate at high densities along the zigzag direction where

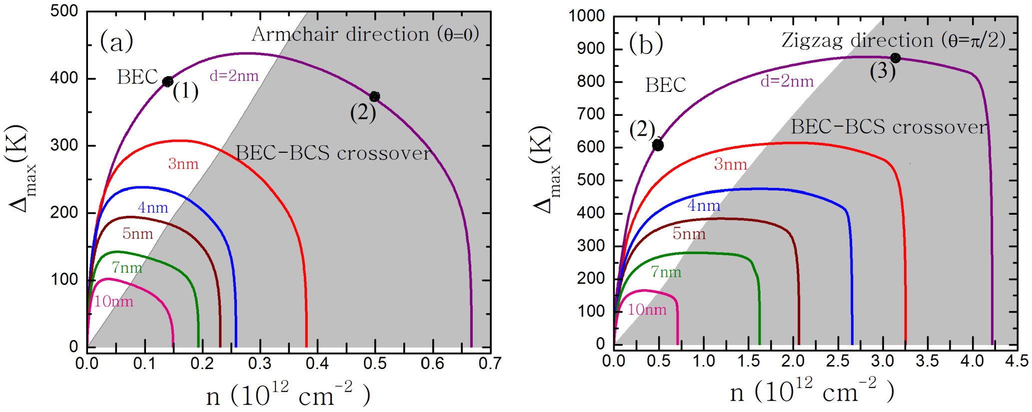

Figure 7.2: Maximum of the superfluid gap along the two main crystallographic directions of phosphorene (a) the armchair direction ($\theta = 0$) and (b) the zigzag direction ($\theta = \pi/2$) for different h-BN effective barrier thickness d.

$0.2 < C_F < 0.8$, especially in the low inter-layer distance. Furthermore, in the high density regime screening kills the superfluid gap before the BCS regime is reached for two directions.

The $\boldsymbol{k}$ dependence of the gap $\Delta(\boldsymbol{k})$ can show the nature of the superfluidity. To highlight the anisotropy of the gap function, we provide three cross sections of $\Delta_{\boldsymbol{k}}$ in Fig. 7.3 for $d =$ 2nm and density marked in Fig. 7.2. We see that in Fig. 7.3(a) for low density the peak in $\Delta_{\boldsymbol{k}}$ along both directions is centered at $k = 0$ in the strongly pairing regime of Bose-Einstein condensation (BEC). In Fig. 7.3(b) the maximum $\Delta_{\boldsymbol{k}}$ is becoming more broad along the zigzag direction but it is still centered around $k = 0$ displaying a remaining bosonic character of the Cooper pairing in the BEC regime but the maximum peak goes to the BEC-BCS crossover regime of weak coupling pairing along the armchair (x) direction. Fig. 7.3(c) shows the cross section of $\Delta(\boldsymbol{k})$ as a function of $\boldsymbol{k}/k_F$ at $n \approx 3.5 \times 10^{12}\text{cm}^{-2}$ where the gap function along the zigzag direction has its maximum. The maximum $\Delta(\boldsymbol{k})$ along zigzag direction confirms that we are in the BEC-(BCS) crossover regime of compact electron-hole pairs at high densities due to the maximum peak near k_F. Furthermore, with increasing density along zigzag direction we would reach BCS but the gap collapses before that happens and so the superfluid does not reach the BCS limit. At very low densities and at small enough interlayer distance the electron-hole system is in the very strong-coupling regime: the gap is large in units of the non interacting Fermi energy, the condensate fraction is close to one, the chemical potential becomes strongly negative and it approaches minus half of the binding energy of the two-body electron-hole problem, which is the bound state energy of an isolated exciton. Moreover, in the BEC limit the radius of the electron-hole Cooper pairs approach the radius of the exciton in the isolated exciton-limit. Therefore, the extreme BEC limit realized at very low densities in our electron-hole system at T=0 is in correspondence with the pure, weakly interacting excitonic system analyzed in detail in Ref. [178]. On the other hand, a direct quantitative comparison between the results of our work and the results of Ref. [178] is not possible and beyond the scope of the present paper, being different the model interaction between carriers and the way the Coulomb screening is included in the two approaches.

There is a condensate of pairs in the zero-momentum state below the critical temperature, the highest temperature at which the normal Fermi system becomes unstable with respect to the formation of pairs. This superfluid transition temperature in two-dimensions is determined by the well known relation

$$T_{KT} = \frac{\pi}{4}\rho_s, \tag{7.14}$$

where $\rho_s(0)$, the superfluid density can be obtained by [183]:

$$\rho_s = g_s \sum_{\boldsymbol{p}} \frac{\nu^2(\boldsymbol{p})}{m_d}. \tag{7.15}$$

Therefore, below T$_{KT}$ superfluidity exits in the e-h pairs condensate where it has an important effect on the transport properties of the condensate. Hence, it is necessary to give the variation of the KT temperature and n_c with distance between the layers. For densities above an onset density n_c if there is any superfluidity at all, the gap would be extremely small. The behavior of the onset density is indeed related to the direction of $\boldsymbol{k}$ due to the different effective masses. In Fig. 7.4(a), we depict n_c as a function of d for several relative directions of the phosphorene layers. At fixed d, the onset density is larger along the zigzag ($\theta = \pi/2$) direction and its value in this direction becomes an order of magnitude bigger than for the armchair ($\theta = 0$) direction as d decreases. The maximum value for n_c approaches 4×10^{12} cm^2 for $d = 2$nm. The maximum T_{KT} which happens in the onset

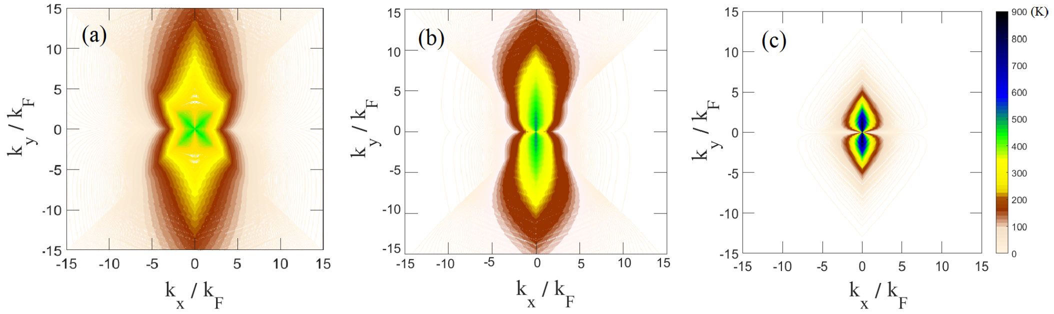

Figure 7.3: Cross section of $\Delta(\boldsymbol{k})$ in the $\boldsymbol{k}/k_F$ phase for density (a) (1) , (b) (2) and (c) (3) marked in Fig.7.2. Here the effective h-BN barrier thickness is $d = 2$nm.

density is plotted in Fig. 7.4(b) as a function of d. This is the highest temperature we find and below which we get superfluidity along the zigzag direction ($\theta = \pi/2$). Furthermore, the maximum value of the KT transition temperatures are well above those predicted for double few-layer sheets of graphene [8].

7.5 Conclusion

In this chapter, we studied the occurrence of excitonic superfluidity in electron-hole double-layer phosphorene at zero temperature. We first generalized the approach for the gap function to the case of a strongly anisotropic double-layer system such as phosphorene. We showed that the gap function is anisotropic, i.e. it depends on the direction of $\boldsymbol{k}$, in which the basic origin of the anisotropy can be explained by using an anisotropic effective mass in the free-electron model. The results showed that the gap function is larger along the zigzag direction and the peak around the maximum gap (Δ_{max}) is located in the BEC regime along the armchair direction and it is in the crossover regime from exciton BEC at low densities to the BCS-like condensate at high densities along the zigzag direction. Importantly, we estimate the anisotropic high KT transition temperature with maximum value up to ~ 90 K in double-layer phosphorene along the zigzag direction with carrier densities as high as 4×10^{12} cm^{-2}. Furthermore, there is a phase transition as a function of the wave vector direction. We showed that the electron-

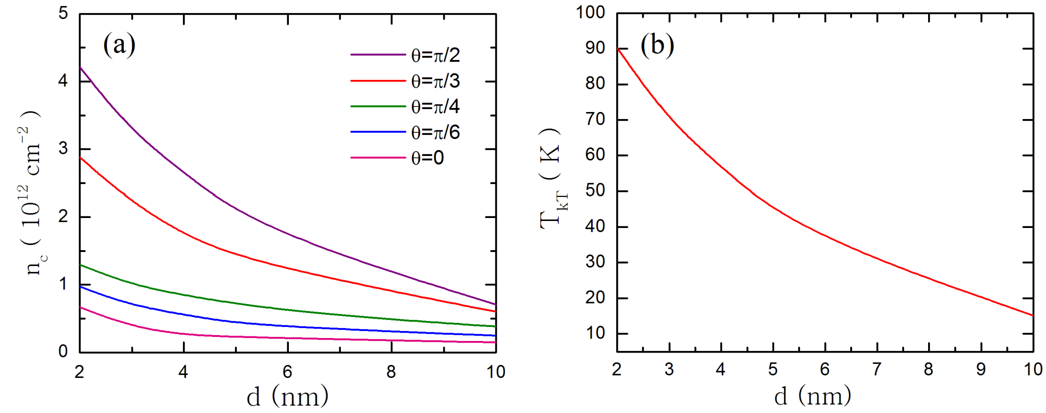

Figure 7.4: (a) Maximum density n_c for several directions as a function of the h-BN effective barrier thickness d. (b) Maximum T_{KT} as a function of the h-BN effective barrier thickness d.

hole double-layer phosphorene system is a promising candidate for revealing a variety of superfluid phases. We highlight in this work that the in-plane anisotropy effects play an important role in the superfluid state in a special direction and for the transition to strongly correlated states and it would be gratifying to observe this effect in experiments.

Chapter 8

Anisotropic charge density wave

> "Can we see charge density waves in a double layer phosphorene?"

The possibility of an inhomogeneous charge density wave phase is investigated in a system of two coupled electron and hole phosphorene monolayers separated by hexagonal boron nitride insulating layers. The charge density wave state is induced through the assumption of negative compressibility of electron/hole gases in a Coulomb drag configuration between the electron and hole phosphorene sheets. Under equilibrium conditions, we derive analytical expressions for the density oscillation along the zigzag and armchair directions of phosphorene. We find that the density modulation not only depends on the sign of the compressibility but also on the anisotropy of the phosphorene low energy bands.

8.1 Introduction

One of the most surprising phenomenon in condensed matter physics is that a Fermi liquid ground state can become unstable leading to inhomogeneous phases [184]. Charge density waves (CDWs) [185], spin density waves (SDWs) [186], and superconductivity [187] are hallmarks of such phases for electrons to lower their energy via a gap opening at the Fermi level. These are special cases of the so-called Peierls distortion, where a local symmetry is broken to achieve a lower ground state energy [188]. However, CDWs are favored in one dimensional (1D) systems or systems which look electronically 1D along a specific direction [189]. Aside from their ubiquity, CDWs tend to pop up in material systems with contemporary interest, including 1D systems and two-dimensional (2D) systems with strong interactions, some of which also happen to be superconducting [190]. Moreover, the amplitude of the CDW can be tuned by the applied drag force [191] which depend on the separation between the layers and temperature. In addition, some types of CDWs can not be explained by simple models of Fermi surface nesting, and are hence topics of active research. The CDW phase can be experimentally observed using scanning tunneling microscopy (STM) [192, 193].

One of the experimental consequences of the formation of CDW states would be the negative contribution of electron-electron correlations to the electronic compressibility [194, 195]. Another experimental indication would be the reentrant integer quantum Hall effect in such systems, induced by pinning of the hexagonal CDW due to disorder [196, 195]. Moreover, CDWs are induced when the compressibility ($\kappa^{-1} = n^2\partial\mu/\partial n$) is negative ($n$ is the density and μ is the chemical potential) [191]. A negative compressibility results from electron-electron interactions, in which the exchange and correlation energies lower the chemical potential as the electron density decreases. This effect has been observed to enhance the capacitance of semiconductor 2D electronic systems by a few percent above the expected geometric capacitance [197]. In comparison to graphene, phosphorene is chemically reactive and tends to form strong bonds with the surface of substrates which lead to structural changes [198, 199, 200]. Naturally, chemically stable 2D material systems, such as graphene and hexagonal boron nitride (h-BN) may be used to protect the fragile, low-chemical-stability of phosphorene [201]. Encapsulated of few-layer phosphorene by h-BN sheets are new ultraclean heterostructures which could be ideal anisotropic 2D systems with high mobility and possible negative compressibility of its electron/hole gas [202].

Recently, a system of two strongly coupled electron-hole bilayer graphene sheets has been investigated in Ref. [189] and new inhomogeneous coupled Wigner crystal phase (c-WC) and 1D-CDW phases were predicted which interplay with the predicted electron-hole superfuid. In contrast to graphene, the large gap in phosphorene allows the contribution of the conduction band to dominate and to change the sign of the compressibility of the electron/hole gases at experimental achievable carrier concentrations. In graphene, the

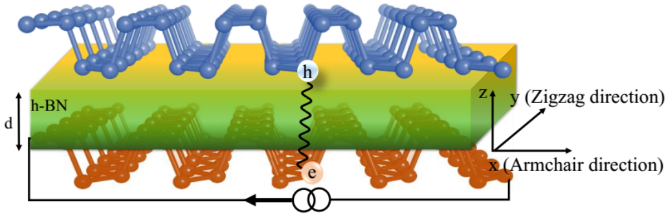

Figure 8.1: Schematic setup of the electron-hole phosphorene monolayers.

compressibility does not become negative in the absence of magnetic field because of the positive contribution of the completely filled valence band [203]. Negative compressibility has been recently observed in atomically thin BP wherein strong correlations results in an enhanced gate capacitance [202]. Importantly, negative compressibility occurs at densities as high as $n \approx 10^{12}\text{cm}^{-2}$ which is achievable in experiment [202]. It was shown that an increase in the gate capacitance of a phosphorene field-effect transistor (FET) originates from such negative compressibility at low electron densities [202].

In this chapter, we investigate the CDW phase of carriers in coupled electron-hole phosphorene sheets where the electrons and holes interact via the Coulomb interaction. In this system, a negative electronic compressibility at sufficiently low charge density enables the formation of a CDW phase through the application of a uniform force field via the Coulomb drag. In the Coulomb drag setup shown in Fig. 8.1 applying the current in one of the layers, *i.e.* the "active" drive layer, induces an electric field in the other layer, *i.e.* the "passive" drag layer, in which no current flows. When the compressibility of the drag layer is negative, the force exerted by this electric field results in CDW phases with a wave-length determined by the absolute value of the compressibility [191]. We generalize the method of Ref. [191] to investigate the controlled formation of a CDW phase caused by a negative electronic compressibility.

8.2 Charge density wave in double-layer phosphorene

We consider two strongly coupled phosphorene layers, one layer containing electrons and the other holes. We assume that an uniform and steady force is applied to the carriers in each layer due to the momentum transfer processes in a drag set up configuration. We can characterize this force using an interlayer scattering time tensor $\hat{\tau}$, *i.e.* the rate at which momentum is transfered from the drive layer to the drag layer. Therefore, the force $\boldsymbol{F}_d$ applied from the drive to the drag layer can be written as $\boldsymbol{F}_d = \hat{M}\hat{\tau}^{-1}\boldsymbol{v}$ [204], where $\boldsymbol{v}$ is the group velocity of carriers in the drive layer and $\hat{M}$ is the mass tensor with diagonal elements $m_x^{e/h}$ and $m_y^{e/h}$ along x (armchair) and y (zigzag) directions, respectively. We solve the equilibrium solution for a single layer of phosphorene to which the drag force is applied. The drag layer is modeled as a quasi-1D electron(hole) gas on a finite strip of length L with density $n_{e/h}$. As no current can flow in the direction of the electric field, the drag force must be exactly balanced by the quantum mechanical force arising from the gradient of the chemical potential $\boldsymbol{F_q} = -\boldsymbol{\nabla}\mu$. Assuming that the density remains uniform in the zigzag (armchair) direction, the equilibrium condition for the armchair (zigzag) direction can be written as

$$\boldsymbol{F}_d^{\alpha} - \nabla\mu + \int_{-L_\alpha/2}^{L_\alpha/2} d\alpha' \frac{e^2\delta n(\alpha')}{2\pi\kappa(\alpha-\alpha')} = 0, \tag{8.1}$$

where $\alpha = x, y$ and $\alpha' = x', y'$. δn is the deviation of the 2D electron density from equilibrium with κ being the dielectric constant. In the linear regime, the gradient of the chemical potential is

$$\boldsymbol{F}_q = -\frac{\partial\mu}{\partial n}\bigg|_n \nabla\delta n. \tag{8.2}$$

Inserting both the drag and quantum mechanical forces in Eq. (8.1) we find the equilibrium condition for the α direction

$$\frac{m_\alpha^e v_\alpha^e}{\tau_d^\alpha} - \frac{\partial\mu}{\partial n}\frac{d\delta n(\alpha)}{d\alpha} + \int_{-L/2}^{L/2} d\alpha' \frac{e^2\delta n(\alpha')}{2\pi\kappa(\alpha-\alpha')} = 0, \tag{8.3}$$

where τ_d^α is the scattering lifetime, the electric field is applied along the α direction in the drive layer and the current is measured along the α direction in the drag layer. We assume $\mathrm{L}_x = \mathrm{L}_y = \mathrm{L}$ and express x and y in units of L/2 and divide the equilibrium solution by the drag force. Therefore, the equilibrium condition for the α direction of the phosphorene layer becomes

$$1 - \bar{\Gamma}_\alpha \frac{d\delta n(\alpha)}{d\alpha} + (\frac{e^2 \tau_d^\alpha}{2\pi\kappa m_\alpha^e v_\alpha^e}) \int_{-1}^{1} d\alpha' \frac{\delta n(\alpha')}{(\alpha - \alpha')} = 0, \tag{8.4}$$

where $\bar{\Gamma}_\alpha = \Gamma_\alpha/\mathrm{L}$ and Γ_α is a direction dependent compressibility-related length given by

$$\Gamma_\alpha = \frac{2\ \tau_d^\alpha}{v_\alpha^e m_\alpha^e} \frac{\partial \mu}{\partial n}. \tag{8.5}$$

The density can be expanded in a series of Chebyshev polynomials

$$\delta n(\alpha) = \sum_{j=1}^{\infty} c_j^\alpha T_{2j-1}(\alpha), \tag{8.6}$$

with c_j^α the expansion coefficients. Using $T_n'(\alpha) = nU_{n-1}(\alpha)$ where $U_n(\alpha)$ is associated with the second kind Chebyshev polynomial, the derivative of the density is given by

$$\frac{d\delta n(\alpha)}{d\alpha} = \sum_{j=1}^{\infty} c_j^\alpha (2j-1) U_{2j-2}(\alpha). \tag{8.7}$$

Eqs. (8.4)-(8.7) can be solved numerically for $\delta n(\alpha)$. Substituting these expressions into Eq. (8.4), multiplying both sides by $(1-\alpha^2)^{1/2} U_{2k-2}(\alpha)$ and integrating over α with the help of standard integrals for the Chebyshev polynomials one can arrive at a set of linear algebraic equations for the coefficients c_j^α

$$\sum_{j=1}^{\infty} W_{kj}^\alpha c_j^\alpha = \delta_{k1}, \qquad k = 1, 2... \tag{8.8}$$

where W is a matrix whose elements are given by

$$W_{kj}^\alpha = (\frac{2\ e^2 \tau_\alpha}{\pi\kappa m_\alpha v_\alpha}) \left[\frac{1}{1-4(k+j-1)^2} + \frac{1}{1-4(k-j)^2} \right] + \bar{\Gamma}_\alpha (2k-1) \delta_{kj}. \tag{8.9}$$

Using Eqs. (8.8) and (8.9), we find from Eq. (8.4) the solution

$$\delta n(\alpha) = \sum_{j=1}^{\infty} [W^{-1}]^{\alpha}_{j1}\ T_{2j-1}(\alpha), \tag{8.10}$$

where W^{-1} is the inverse of matrix W. In the next subsection, we obtain the interlayer scattering time.

8.3 Interlayer scattering rate

The Coulomb drag technique allows a unique access to the interlayer scattering rate via a resistance measurement. This can be simply shown within the Drude model [165]. Considering an electron-hole double layer system, the anisotropic drag resistivity is given by [47]

$$\rho_d^{\alpha\beta} = \frac{\hbar^2}{2\pi e^2 n_1 n_2 k_B T} \int \frac{d^2q}{(2\pi)^2} q_\alpha q_\beta \int_0^\infty d\omega \frac{|U_{eh}(\boldsymbol{q},\omega)|^2 \mathrm{Im}\Pi_h(\boldsymbol{q},\omega)\mathrm{Im}\Pi_e(\boldsymbol{q},\omega)}{\sinh^2(\hbar\omega/2k_BT)}, \tag{8.11}$$

where α and β indices refer to the x and y components. We assume that the drive layer contains electrons and the drag layer contains holes. Therefore, the drag resistivity depends on the interlayer momentum relaxation rate as

$$\rho_d^{\alpha\beta} = \frac{\hat{M}^e_\alpha}{n_e e^2 \tau_d^{\alpha\beta}}. \tag{8.12}$$

The dynamically screened interlayer potential $U_{eh}(\boldsymbol{q},\omega)$ can be obtained by solving the corresponding Dyson equation [65]

$$U_{eh}(\boldsymbol{q},\omega) = \frac{V_{eh}(q)}{\det|\varepsilon_{eh}(\boldsymbol{q},\omega)|}, \tag{8.13}$$

where $V_{eh}(q) = \nu(q)\exp(-qd)$ is the unscreened 2D Coulomb interaction with d being the interlayer separation. $\nu(q) = 2\pi e^2/q\kappa$ and $\varepsilon_{eh}(\boldsymbol{q},\omega)$ is the dynamic dielectric matrix of the system. Using the random phase approximation (RPA) formalism, we obtain [66, 168]

$$\varepsilon_{eh}(\boldsymbol{q},\omega) = \delta_{eh} + V_{eh}(q)\Pi_e(\boldsymbol{q},\omega). \tag{8.14}$$

For an electron gas system, the non-interacting density–density response function can be obtained from the following equation [62]

$$\Pi_{e/h}(\boldsymbol{q},\omega) = -\frac{g_s}{\nu}\sum_{\boldsymbol{k}} \frac{f^0(E^{e/h}_{\boldsymbol{q}}) - f^0(E^{e/h}_{\boldsymbol{k}+\boldsymbol{q}})}{E^{e/h}_{\boldsymbol{q}} - E^{e/h}_{\boldsymbol{k}+\boldsymbol{q}} + \hbar\omega + i\eta}. \tag{8.15}$$

Here $f^0(E^{e/h}_{\boldsymbol{q}})$ is the Fermi-Dirac distribution at energy E corresponding to the wave vector $\boldsymbol{q}$, $g_s = 2$ is the spin degeneracy, ν is the unit cell surface and η is the broadening parameter that may account for disorder in the system. Using the following anisotropic parabolic energy dispersion relation

$$E^{e/h}_{\boldsymbol{k}} = \frac{\hbar^2}{2}\left(\frac{k_x^2}{m^x_{e/h}} + \frac{k_y^2}{m^y_{e/h}}\right) - \mu_{e/h}, \tag{8.16}$$

the temperature-dependent dynamical density-density response function for intra-band transitions in an anisotropic 2D material can be calculated

$$\begin{aligned} \frac{\Pi_{e/h}(\boldsymbol{q},\omega)}{g^{e/h}_{2D}} &= -\int dK \frac{\Phi_{e/h}(K,T)}{Q_{e/h}} \times \\ &\left[sgn(\mathrm{Re}(Z_-))\frac{1}{\sqrt{Z_-^2 - K^2}} - sgn(\mathrm{Re}(Z_+))\frac{1}{\sqrt{Z_+^2 - K^2}} \right]. \end{aligned} \tag{8.17}$$

In the above symmetric form of temperature-dependent anisotropic density-density response function, we have defined $\boldsymbol{Q_{e/h}} = (\boldsymbol{q}/k^{e/h}_F)\sqrt{m^{e/h}_D/\hat{M}^{e/h}}$, $\boldsymbol{K_{e/h}} = (\boldsymbol{k}/k^{e/h}_F)\sqrt{m^{e/h}_D/\hat{M}^{e/h}}$, $g^{2D}_{e/h} = m^{e/h}_D/\pi\hbar^2$, $Z^{\pm}_{e/h} = ((\hbar\omega + i\eta)/\hbar Q_{e/h}\nu^{e/h}_F) \pm (Q_{e/h}/2)$ with $\nu^{e/h}_F = \hbar k^{e/h}_F/m^{e/h}_D$, $m^{e/h}_D = \sqrt{m^{e/h}_x m^{e/h}_y}$ is the 2D density of state mass, and

$$\Phi_{e/h}(K_{e/h},T) = \frac{K_{e/h}}{1 + \exp[(K^2_{e/h}E^{e/h}_F - \mu^{e/h})/k_BT]}, \tag{8.18}$$

where $k^{e/h}_F = \sqrt{2\pi n^{e/h}}$ and $\mu_{e/h}$ is the chemical potential of the electron and hole layers which is determined by the particle number conservation condition [63]. We work in polar coordinates $\boldsymbol{q} = q(\cos\theta, \sin\theta)$, $Q_{e/h} = (q/k^{e/h}_F)\sqrt{m^{e/h}_D R^{e/h}(\theta)}$ in which the orientation factor $R_{e/h}$ is expressed as $R^{e/h}(\theta) = \left(\cos^2(\theta)/m^{e/h}_x + \sin^2(\theta)/m^{e/h}_y\right)$. At sufficiently low temperature and $q \ll k_F^{e/h}$ one can approximate $\mathrm{Im}[\Pi_{e/h}(\boldsymbol{q},\omega)]$ by the low frequency expression

$$\mathrm{Im}[\Pi_{e/h}(\boldsymbol{q},\omega)] \approx -\frac{(m_D^{e/h})^2\ \omega}{2\pi\hbar^3 Q_{e/h}(k_F^{e/h})^2}. \tag{8.19}$$

In this case, the screened potential of the electron-hole interaction in Eq. (8.13) $|U_{eh}(\boldsymbol{q},\omega)|$ can be approximated by the static interlayer Coulomb interaction in the long wave-length limit as

$$U_{eh}(q \to 0) = \frac{v_q e^{-qd}}{[1 - v_q \frac{\partial n_e}{\partial \mu_e}][1 - v_q \frac{\partial n_h}{\partial \mu_h}] + \frac{\partial n_e}{\partial \mu_e}\frac{\partial n_h}{\partial \mu_h} v_q^2 e^{-2qd}}. \tag{8.20}$$

An important property of this equation is the compressibility, related to the small q limit of the proper density-density response function of the compressibility sum rule [205]. There is an exact relation between the compressibility and the long wave-length limit of the static density-density response function as $\Pi_{e/h}(q \to 0) = -\partial n_{e/h}/\partial \mu_{e/h}$ [205]. Inserting Eq. (8.20) in Eq. (8.11) we have

$$U_{eh}(q \to 0) = \frac{2\pi e^2}{\kappa}\frac{q}{\epsilon_s(q)}, \tag{8.21}$$

where $\epsilon_s(q)$ is defined as

$$\epsilon_s(q) = [q^2 e^{qd} - q(q_s^e + q_s^h)e^{qd}] + q_s^e q_s^h (e^{qd} - e^{-qd}). \tag{8.22}$$

here $q_s^{(e/h)} = (2\pi e^2/\kappa)(\partial n_{e/h}/\partial \mu_{e/h})$ is the screening wave vector related to compressibility. Since the most important contribution from the integration over q comes from the region in which $q \leq 1/d$ and since $1/d \ll k_F^{e/h}$, we may neglect the first term in the denominator of Eq. (8.21) and obtain the simple form

$$U_{eh}(q \to 0) = \frac{2\pi e^2}{\kappa}\frac{q}{2q_s^e q_s^h \sinh(qd)}. \tag{8.23}$$

Using Eq. (8.23), the drag resistivity in Eq. (8.11) is given by

$$\rho_{eh}^{\alpha\beta} \approx -\frac{\hbar^2}{(2\pi)^3 e^2 n_h n_e k_B T} \frac{(m_D^e)^2 (m_D^h)^2}{(2\pi\hbar)^3 k_F^e k_F^h} \int d\theta \int \frac{q\ dq\ q_e^\alpha\ q_h^\beta}{Q_e Q_h} (\frac{\pi e^2}{\kappa})^2 \frac{q^2}{(q_{de} q_{dh})^2 (\sinh^2(qd))} \times \int_0^\infty d\omega \frac{\omega^2}{\sinh^2(\frac{\hbar\omega}{(2k_B T)})}. \tag{8.24}$$

This allows one to analytically obtain the integration over q and ω, by using $\int_0^\infty dx x^p / 4\sinh^2(x/2) = p!\ \zeta(p)$ [206]. Since $\rho_{eh}^{xy} \propto \int d\theta \sin(\theta)\cos(\theta) = 0$, the off diagonal elements of the drag resistivity vanish. The analytical results for the diagonal elements of the drag resistivity at low temperatures ($T \ll T_F$) becomes

$$\rho_{eh}^{\alpha\alpha} = \frac{e^2 \zeta(3)}{16\pi^3 \hbar^2} \frac{(k_B T)^2 \sqrt{m_\alpha^e m_\alpha^h m_d^e m_d^h}}{n_e n_h E_F^e E_F^h} \frac{1}{(q_s^e d)^2 (q_s^h d)^2}. \tag{8.25}$$

One can then use this equation into Eq. (8.12) to get a diagonal tensor for the anisotropic interlayer scattering rate

$$\tau_d^{\alpha\alpha} = \frac{16\pi^3 \hbar^2 (q_s^e d)^2 (q_s^h d)^2}{e^4 \zeta(3)} \frac{n_h E_F^e E_F^h\ \hat{M}_e^\alpha}{(k_B T)^2 \sqrt{m_e^\alpha m_h^\alpha m_D^e m_D^h}}. \tag{8.26}$$

For a system with equal electron and hole densities $n_e = n_h = n$ and equal chemical potentials, we have $q_s^e = q_s^h = (8\pi^2/\lambda)$, where $\lambda = (4\pi\kappa/e^2)(\partial\mu/\partial n)$ is the compressibility related length [191].

8.4 Results and discussion

The density modulation depends directly on the system anisotropy and also on the sign of the compressibility. In order to explore the CDW in the phosphorene layer subjected to the drag force, we study the effects of the sign of the compressibility on the equilibrium solution, *i.e.* Eq. (8.4). In Fig. 8.2(a) we show the numerical results as calculated from the equilibrium solution for a positive compressibility ($\partial\mu/\partial n > 0$) in the armchair (x) and zigzag (y) directions of phosphorene with effective masses $\mathrm{m}_x^e = 0.16\mathrm{m}_0$ and $\mathrm{m}_y^e = 1.24\mathrm{m}_0$ and $\mathrm{m}_x^h = 0.15\mathrm{m}_0$ and $\mathrm{m}_y^h = 4.95\mathrm{m}_0$ with the velocity $v_x^e = 6 \times 10^6$ (cm/s) and $v_y^e = 1.5 \times 10^6$ (cm/s) [207, 55] with m_0 being the free electron mass.

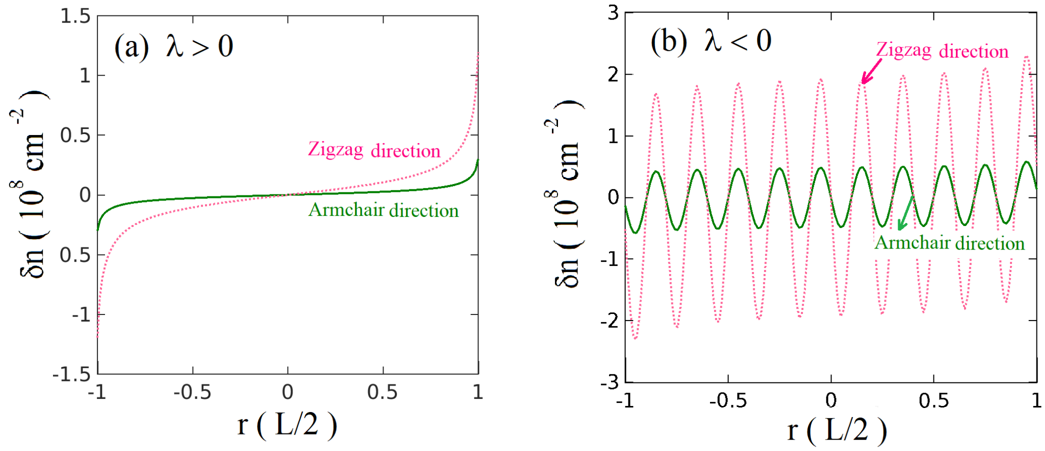

Figure 8.2: The equilibrium solutions of Eq. (8.4) for (a) positive compressibility ($\partial\mu/\partial n > 0$) and (b) negative compressibility ($\partial\mu/\partial n < 0$) with $|\partial\mu/\partial n| \approx 5\ \times 10^{-12}$ meV cm^2 along the armchair(x) and zigzag(y) directions at the equilibrium density $n = 2 \times 10^{12}\mathrm{cm}^{-2}$. Here d = 2nm and T = 2K. The length of the strip is taken to be L = 5λ.

We set the dielectric constant $\kappa \approx 4$ [208] for encapsulated phosphorene by h-BN layers [191] and L= 5λ. We can see that similar to the case of an isotropic 2DEG [191] the CDW is not stable for phosphorene along the directions where the compressibility is positive. Note that, the charge doesn't change at the center of phosphorene but it accumulates along the edges due to the strong electric field induced at the sharp edges. As a direct consequence of the band anisotropy the charge accumulation is different at the two directions of phosphorene. We show the charge modulation for phosphorene layers in Fig. 8.2(b) when the compressibility is negative. One can see that the density modulation along the zigzag (y) and armchair (x) directions have different amplitude. The amplitude and frequency of these oscillations depend on the applied electric field and the value of Γ_α in our Coulomb drag setup providing opportunity for electronic tuning. Moreover, phosphorene shows a CDWs at higher densities as compared to typical 2D electron gas systems [191].

The Coulomb interaction between the holes and electrons can also significantly enhance the occurrence of the CDW phase, especially when $r_s \gg d$, where $r_s = 1/(a_B^{*(e/h)}\sqrt{n\pi})$ is the average distance between two neighbor-

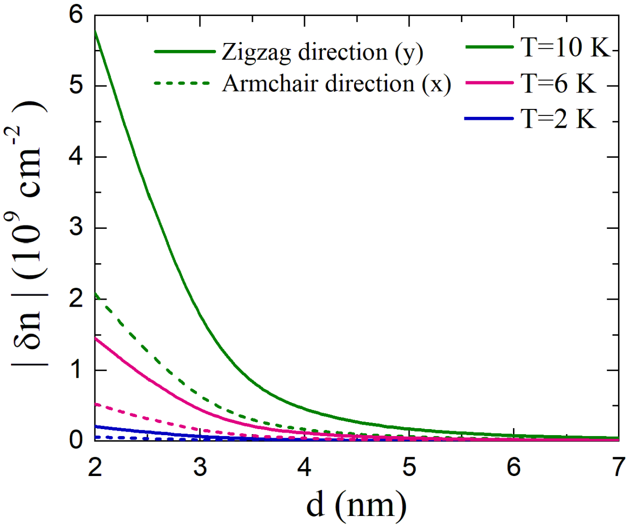

Figure 8.3: Amplitude of the charge modulation $|\delta n|$ for negative compressibility with $\partial\mu/\partial n \approx$ - 5 $\times 10^{-12}$ meV cm^2 along the zigzag (y) and armchair (x) directions as a function of the separation between the BP layers d at different temperatures for equilibrium density $n = 2 \times 10^{12}$cm^{-2} and L $= 5\lambda$.

ing in-plane carriers and $a_B^{*(e/h)} = (\hbar\kappa/m_D^{e/h} e^2)$, the effective Bohr radius. Fig. 8.3 shows the amplitude of the CDW along both zigzag and armchair directions as a function of the separation between the two layers at different temperatures. We find that the CDW state does become stable as the spacing between the layers is decreased. When we increase the separation d, the density modulation strongly reduced because at sufficiently large d, the strength of the interlayer attraction is decreased.

8.5 Conclusion

In this chapter, we considered a system of two strongly coupled electron-hole phosphorene layers interacting by the Coulomb interaction. The system we proposed is expected to support large transresistivity [47] due to the larger effective mass of the carriers and consequently the large density of states and CDW modulations in phosphorene. We showed that the negative electronic compressibility of the double layer electron-hole phosphorene system at achievable density enables the generation of a CDW phase through the application of a uniform force field via the Coulomb drag. We solved the equilibrium solutions for the drag layer modeled as a quasi-1D system. By using the compressibility sum rule in which the compressibility is related to the small momentum limit of the proper density-density response function, an analytical expression is obtained for the anisotropic drag force. We found that the density modulation not only depends on the sign of the compressibility but also depends on the system anisotropy. The amplitude of the CDW phase depends on the separation between the layers and temperature. The wave-length of the CDW can be also electrically tuned by changing the value of Γ_α. This might be changed in experiment by changing, via a gate, the density of the passive layer.

There are a number of ways that a CDW phase could be experimentally identified [209]. This phase can be detected by optical methods, such as differential absorption or diffraction and also by using STM which can detect a number of features related to the onset of CDW including charge modulation, periodic distortion of atomic position, and the opening of a gap in the density of states. Angle resolved photoemission spectroscopy (ARPES) can also show which portions of the Fermi surface are gapped out by the CDW [210]. This can give guidance whether the CDW is driven by Fermi surface nesting or by something more exotic [211]. By perturbing a material with an ultrashort laser pulse and following the resulting transient ARPES spectra, one can obtain insight into the dynamics both of quasiparticle occupations and of the electronic structure itself [212].

Chapter 9

Summary and outlook

9.1 Summary

In this thesis, the many body properties of monolayer and double layer BP were theoretically investigated. Within the linear response theory, these properties were studied for different configurations of an anisotropic two-dimensional systems like phosphorene. The main results have been presented in chapters 3 to 9 which answered the following questions:

How drag effect in BP is affected by the anisotropy band structure?

In chapter 3, the anisotropic drag resistivity was studied in a structure composed of two spatially separated 2D electron gas systems with paraboloidal band structure. The double-layer phosphorene was chosen as an example system on which the anisotropic drag theory was applied. It was shown that the drag resistivity depends not only on the typically considered parameters such as temperature, inter-layer separation, carrier density and nature of elementary excitations, but also on the direction of momentum transfer between the two layers in addition to the rotational parameter. It was also shown that while the diagonal elements of the anisotropic drag resistivity tensor has different values due to different electron effective masses along x and y directions at any temperatures of interest, there are non-zero off-diagonal elements for the rotated structure. The non-zero off-diagonal elements have not been reported before in a 2D coupled system in the absence of an applied magnetic field. Furthermore, both diagonal elements of anisotropic drag resistivity tensor increase with decreasing inter-layer separation and electron density. The results showed that the anisotropic ratio varies effectively with the change of temperature and electronic density. To improve on the RPA results at low electron density, the zero temperature Hubbard LFC factor was included in the calculations and shown that the inclusion of LFC strongly influences the drag resistivity values. The results suggested that the rotational parameter between layers can be considered as an extra degree of freedom in order to control the momentum transfer between coupled layers. The work highlights the role of anisotropic band structure on drag resistivity, as an important transport quantity in a coupled 2D structure.

What is the optical response of an anisotropic 2D electron gas system in the presence of Rashba spin-orbit interaction?
The energy spectrum and optical response of an anisotropic 2D electron gas system in the presence of Rashba spin-orbit interaction in chapter 4. Based on the Kubo formalism, the optical conductivity tensor was calculated by considering Rashba spin-flip excitations. It was found that the effective mass anisotropy plays an important role in the optical absorption spectrum through the direction-dependent Rashba spin splitting. As a general result, the diagonal components of the optical conductivity tensor were inversely proportional to the corresponding effective mass elements. Furthermore, the effective mass asymmetry was an additional degree of freedom to tune the height and width of the absorption peak. This introduced aspects to the optical conductivity for spintronic applications of 2D anisotropic materials such as phosphorene and group-IV monochalcogenides. It was also shown that larger optical absorption is generated when the polarization of the radiation is along the armchair direction and its maximal value was enhanced by increasing the effective mass ratio. However, the width of the absorption window strongly depends on both the polarization direction and the effective mass ratio. Finally, the position of the absorptive peak moved to higher frequencies with increasing Rashba parameter and electron density. The results suggested an interesting way to determine some of the spintronic characteristics of a class of 2D nanostructures, with anisotropic Rashba effect, using optical methods.

How do polar substrates/spacers influence the plasmons in monolayer and double-layer phosphorene systems?
In chapter 5, the monolayer and double-layer phosphorene systems located

on polar substrates/spacers have been considered. The dynamical dielectric function was calculated within the RPA and including many-body electron-electron interaction in phosphorene layer(s) as well as the interaction between electrons and the long range electric field generated by SO phonon modes. The anisotropic coupled plasmon-SO phonon dispersion relations were derived in the long wavelength limit. In the case of monolayer, due to the two relevant SO phonon modes of the substrate, three hybrid plasmon-SO phonon branches were obtained. It was shown that the hybrid plasmon-SO phonon modes are stronger along x direction because of lower corresponding effective mass and at large electron densities, these modes are stronger especially along x direction. Exploring the effects of specific substrates on the coupled modes showed that the phonon frequency (ω_{SO}) of a substrate is the most effective parameter that controls the phonon-like modes (ω_+^λ) whereas α parameter changes the plasmon-like modes, ω_-. Hence the choice of substrate can be utilized in order to engineer the plasmon-SO phonon dispersion phosphorene systems. Also, the analytical expressions for the hybrid modes at the long wavelength limit have been derived for the double-layer phosphorene. The results showed that there are six hybrid modes: three acoustic, $(\omega_\pm)_{ac}$, and three optical modes, $(\omega_\pm)_{op}$. By evaluating the energy loss function, it was found that similar to the case of monolayer phosphorene, all plasmon-SO phonon modes are stronger along x direction than the modes along y direction. The effect of misalignment of the two layers on the hybrid modes has been also investigated and found that the acoustic branches may become strongly damped or a transition to the optical modes can be observed at small rotations. Finally, the hybrid modes of double-layer phosphorene was studied for several separations between the two layers and a transition to the optical modes (fast damping excitations) by increasing (decreasing) d_2 was observed for the acoustic modes. As a result of the calculations, rotation angle and separation between two layers can be used as a mechanism for tuning the plasmon-SO phonon coupling effects.

Can plasmon modes of BP affect by an applied uniaxial tensile strain?

In chapter 6, we have studied the effect of an applied uniaxial tensile strain on the plasmon dispersion of monolayer, bilayer and double-layer phosphorene structures. As a consequence of anisotropic energy band, the changes of plasmon dispersions are different along the armchair and zigzag directions and strongly depend on the direction of the applied uniaxial strain. Also, in two-layer phosphorene systems, it was shown that the strain-dependent orientation factor of layers control plasmon energies. In addition, we obtained that while the behavior of the optical and acoustic modes are similar in both bilayer and double-layer phosphorene, plasmons along the armchair direction are more affected by strain. Moreover, for the strained bilayer structure, two different cases have been investigated: *i*) the strain is equally applied to the two layers, and *ii*) the strain is applied only to one of the layers. We have found that the effect of strain on the long-wavelength plasmon modes in case *i*) is stronger than the case *ii*). Finally, the diagonal elements of the transresistivity tensor have been calculated within the RPA for a double-layer phosphorene in which two parallel aligned phosphorene monolayers are under strain and sandwiched by *h*-BN. The results suggested that the changes in the plasmonic excitations, due to the applied strain, are mainly responsible for the predicted behaviors of the drag resistivity.

How does excitonic superfluidity occur in a electron-hole double-layer phosphorene at zero temperature ?
In chapter 7, the occurrence of excitonic superfluidity in electron-hole double-layer phosphorene was studied at zero temperature. At first, an approach for the gap function of the strongly anisotropic double-layer system such as phosphorene have been generalized. It was shown that the gap function is anisotropic, depending on the direction of $\boldsymbol{k}$, in which the basic origin of the anisotropy can be explained by using an anisotropic effective mass in the free-electron model. The results showed that the gap function is higher along zigzag direction and the peak around the maximum gap (Δ_{max}) is located in the BEC regime along armchair direction and it is in the crossover regime from exciton BEC at low densities to the BCS-like condensate at high densities along zigzag direction. Importantly, the anisotropic high KT transition temperature with maximum value up to ~ 90 K was estimated in double-layer phosphorene along zigzag direction with large carrier densities as high as 4×10^{12} cm^{-2}. Furthermore, it was shown that the in-plane anisotropy effects play an important role in the superfluidity for the transition to strongly correlated states in a special direction and it would be gratifying to observe this effect in experiments.

Can we see charge density waves in a double layer phosphorene?
A system consisting of two strongly coupled electron-hole phosphorene layers interacting by the Coulomb interaction was considered in chapter 8. It

was shown that the negative electronic compressibility of the double layer electron-hole phosphorene system at achievable density enables the generation of a CDW phase through the application of a uniform force field via the Coulomb drag. The equilibrium solutions were solved for the drag layer modeled as a quasi-1D system. By using the compressibility sum rule in which the compressibility is related to the small momentum limit of the proper density-density response function, an analytical expression was obtained for the anisotropic drag force. It was found that the density modulation not only depends on the sign of the compressibility but also depends on the system anisotropy. The amplitude of the CDW phase depended on the separation between the layers and temperature. The wave-length of the CDW can be also electrically tuned by changing the value of Γ_α. This can be varied in experiment by a gate, the density of the passive layer. There are a number of ways that a CDW phase could be experimentally identified [209]. This phase can be detected by optical methods, such as differential absorption or diffraction and also by using STM which can detect a number of features related to the onset of CDW including charge modulation, periodic distortion of atomic position, and the opening of a gap in the density of states. Angle resolved photoemission spectroscopy (ARPES) can also show which portions of the Fermi surface are gapped out by the CDW [210]. This can give guidance whether the CDW is driven by Fermi surface nesting or by something more exotic [211]. By perturbing a material with an ultrashort laser pulse and following the resulting transient ARPES spectra, one can obtain insight into the dynamics both of quasiparticle occupations and of the electronic structure itself [212].

9.2 Outlook

In chapter 3, the anisotropic drag resistivity was studied in a structure composed of two spatially separated double-layer phosphorene. Over the past decade, this phenomena in double-layer two-dimensional electron systems has been a subject of extensive experimental and theoretical studies. Furthermore, the hybrid structures with different 2D materials, such as graphene-MoS_2 hybrid structure, have attracted significant attentions. It would be interesting to see the Coulomb drag in heterostructures made of monolayer BP-graphene/TMDCs.

In chapter 6, the effect of an applied uniaxial tensile strain on the plasmon dispersion of monolayer, bilayer and double-layer phosphorene structures has been studied. Recently, it was shown that a graphene/dielectric/metal configuration exhibits extreme plasmon confinement, an order of magnitude higher than that of conventional graphene plasmons so called acoustic plasmons. These phenomena has been recently investigated in monolayer and multilayers of BP placed just a few nanometers above a conducting plate. In the presence of a conducting plate, the acoustic plasmon dispersion for the armchair direction was found to exhibit the characteristic linear scaling in the mid- and far-infrared regime while in the zigzag direction, such scaling behavior is not evident due to relatively tighter plasmon confinement. It is nice to see how applied uniaxial tensile strain affects on the acoustic plasmons.

In chapter 7, we have investigated the occurrence of excitonic superfluidity in electron-hole double-layer phosphorene at zero temperature. Investigation of superfluidity in this system through the Coulomb drag phenomena in the exciton regime would also be an interesting work. At lower temperatures, it was shown that the qualitative behavior of the Coulomb drag transresistance is completely determined by the requirement of least dissipation and is independent of all microscopic details. Transresistance measurements have shown a foolproof test for the presence of an excitonic condensate. Therefore, the Coulomb drag transresistance for a coupled electron-hole system is well described by the Fermi-liquid theory while when excitons form and condense new features appear.

Chapter 10

Samenvatting

Deze thesis onderzocht theoretisch verschillende veel deeltjes seigenschappen van monolaag en dubbellaagse BP. Binnen de lineaireresponse theorie werden deze eigenschappen bestudeerd voor verschillende configuraties van anisotrope tweedimensionale systemen zoals fosforeen. De belangrijkste resultaten zijn gepresenteerd in hoofdstukken 3 tot 8 en de volgende vragen werden beantwoord:

Hoe wordt het sleepeffect bij BP beïnvloed door de anisotropie van de bandenstructuur? Hoofdstuk 3 bestudeerde de anisotrope 'drag resistivity' in een structuur die bestaat uit twee ruimtelijk gescheiden 2D elektronen gas systemen met paraboloïde bandenstructuur. De dubbellaagse fosforeen is gekozen als een voorbeeldsysteem waarop de anisotrope weerstandstheorie wordt toegepast. Er werd aangetoond dat de 'drag resistivity' niet alleen afhangt van de typisch beschouwde parameters zoals temperatuur, tussenlaagscheiding, draaggolfdichtheid en aard van elementaire excitaties, maar ook van de richting van de impulsoverdracht tussen de twee lagen bovenop de rotatieparameter. Ook waren er geen niet-nul off-diagonale elementen voor de geroteerde structuur. De verschillende waarden van de diagonale elementen van de anisotrope weerstandsgevoeligheidstensor zijn een gevolg van verschillende elektron effectieve massa langs x en y richtingen. De niet-nul off-diagonale elementen zijn nog niet eerder gemeld in een 2D-gekoppeld systeem zonder een magnetisch veld. Bovendien nemen beide diagonale elementen van de anisotrope sleepweerstandsensor toe met afnemende scheiding tussen de lagen en elektronendichtheid. De resultaten toonden dat de anisotrope verhouding effectief varieert met de verandering van temperatuur en elektronische dichtheid. Om de RPA-resultaten bij een lage elektronendichtheid te verbeteren, is de Hubbard LFC-factor met een nul temperatuur opgenomen in de berekeningen. De resultaten gaven weer dat de LFC de waarden voor de weerstand sterk beïnvloedt. Verder kon de rotatieparameter tussen de lagen beschouwd worden als een extra vrijheidsgrad voor de impulsoverdracht tussen gekoppelde lagen.

Wat is de optische respons van een anisotroop 2D elektronengassysteem in de aanwezigheid van Rashba spin-baan-interactie?

Het energiespectrum en de optische respons van een anisotroop 2D-elektronen gas systeem in de aanwezigheid van Rashba spin-baan-interactie werd bestudeerd in hoofdstuk 4. Op basis van het Kubo-formalisme is de tensor voor de optische geleidbaarheid berekend door de Rashba spin-flip-excitaties in beschouwing te nemen. Er werd gevonden dat de effectieve 'massa anisotropie' een belangrijke rol speelt in het optische absorptiespectrum door de richtingsafhankelijke Rashba-rotatiesplitsing. Als een algemeen resultaat waren de diagonale componenten van de optische geleidbaarheidstensor omgekeerd evenredig met de overeenkomstige effectieve massa-elementen. Bovendien was de effectieve massa symmetrie een extra vrijheids-parameter om de hoogte en breedte van de absorptiepiek af te stemmen. Dit introduceerde aspecten van de optische geleidbaarheid relevant voor spintronische toepassingen van 2D-anisotrope materialen zoals fosfor en monochalcogeniden van groep IV. Tevens werd de grotere optische absorptie gegenereerd wanneer de polarisatie van straling langs de richting van de 'armchair' plaatsvindt en de maximale waarde ervan verbetert door de effectieve massaverhouding te vergroten. De breedte van het absorptievenster was echter sterk afhankelijk van zowel de polarisatierichting als de effectieve massaverhouding. Ten slotte verplaatste de positie van de absorptiepiek zich naar hogere frequenties met het verhogen van de Rashba parameter en elektronendichtheid.

Hoe beïnvloeden polaire substraten de plasmonen in monolaag en dubbel-laagse BP-systemen?

In hoofdstuk 5 zijn de monolaag en dubbellaagse fosfor systemen op polaire substraten / scheidingen betudeerd. De dynamische dielectrische functie werd berekend binnen de RPA. De dynamische dielectrische functie omvat veel oldtjes elektron-elektron interactie in fosfeenlagen als de interactie tussen elektronen en het lange afstand elektrisch veld dat gegenereerd is door SO fonon modi. De anisotrope gekoppelde plasmon-SO-fonondispersierelaties zijn afgeleid in de langegolflengteg limiet. In het geval van de monolaag werden, als gevolg van de twee relevante SO-fononen van het substraat, drie hybride plasmon-SO-fonontakken verkregen. Er werd bewezen dat de hybride plasmon-SO-fonon-modi sterker zijn in de richting x vanwege de lagere corresponderende effectieve massa. Bij grote elektronendichtheden zijn deze modi sterker, vooral in de richting van x. Onderzoek naar de effecten van specifieke substraten op de gekoppelde modi toonde aan dat de fononfrequentie (ω_{SO}) van een substraat de meest effectieve parameter is in fononachtige modi (ω_+^λ) terwijl de α parameter de plasmon-achtige modi verandert, ω_-. Derhalve kan de substraat keuze worden gebruikt om de plasmon-SO-fonondispersie te wijzigen. Ook zijn de analytische expressies voor de hybride modi bij de lange golflengte limiet afgeleid voor de dubbellaagse fosfeen. De resultaten demonstreerden dat er zes hybride modi zijn: drie akoestische, $(\omega_\pm)_{ac}$, en drie optische modi,$(\omega_\pm)_{op}$. Door de energieverliesfunctie te evalueren, werd vastgesteld dat, vergelijkbaar met het geval van monolaag fosfor, alle plasmon-SO fonon-modi sterker zijn in de richting x dan de modi langs de richting y. Daarnaast is het effect van verkeerde uitlijning van de twee lagen op de hybride modi onderzocht. Zo konden de akoestische takken sterk worden gedempt of kon een overgang naar de optische modi worden waargenomen bij kleine rotaties. Tenslotte werden de hybride modi van de dubbellaagse fosforeen onderzocht voor verschillende scheidingen tussen de twee lagen. Ook werd een overgang naar de optische modi (snelle dempingsexcitaties) door het verhogen (afnemen) van d_2 waargenomen voor de akoestische modi. Als resultaat van de berekeningen kan de rotatiehoek en de scheiding tussen twee lagen worden gebruikt als een mechanisme voor het afstemmen van de plasmon-SO-fononkoppelingseffecten.

Kunnen plasmamodi van BP worden beïnvloed door een uniaxiale trekspanning?

Hoofdstuk 6 bestudeerde het effect van een uniaxiale trekspanning op de plasmondispersie van de monolaag, dubbellaag en de dubbellaagse fosforstructuren. Als een gevolg van de anisotrope energieband zijn de plasmondispersies verschillend langs de 'armchair' en de zigzagrichting. Ook zijn de veranderingen sterk afhankelijk van de richting van de uniaxiale spanning. Tevens werd voor de tweelaagse fosforeen systemen aangetoond dat de spanningsafhankelijke oriëntatiefactor van de lagen de plasmon-energieën beinvloed. Bovendien hebben we vastgesteld dat hoewel het gedrag van de optische en akoestische modi vergelijkbaar is in zowel bilaag als dubbellaagse fosfor, de plasmonen in de ‘armchair’ richting meer worden beïnvloed door de spanning. Bovendien zijn voor de gespannen dubbellaagstructuur twee diverse gevallen onderzocht: (i) de spanning wordt gelijtijdig toegepast op de twee lagen en (ii) de spanning wordt alleen toegepast op één van de lagen. We hebben ontdekt dat het effect van spanning op de plasmonen met lange golflengte in geval (i) sterker is dan de casus (ii). Ten slotte zijn de diagonale elementen van de trans-weerstandtensor berekend binnen de RPA voor een dubbellaagse fosfor, waarin twee parallel uitgelijnde fosfor-monolagen onder spanning staan en worden ingeklemd door h-BN. De resultaten toonden aan dat de veranderingen in de plasmonische excitaties, vanwege de toegepaste spanning, hoofdzakelijk verantwoordelijk zijn voor het voorspelde gedrag van de ‘drag resistivity’.

Hoe manifesteert de exciton superfluïditeit voor het dubbele elektron-gat monolaag BP?

Hoofdstuk 7 bestudeerde de excitonische superfluiditeit in elektron-holte dubbellaags fosforeen bij nul-temperatuur. In eerste instantie is een benadering voor de klooffunctie van het sterk anisotrope dubbellaags systeem fosfor veralgemeend. Er werd aangetoond dat de gap-functie anisotroop is, nl.afhankelijk van de richting van $\boldsymbol{k}$,en de oorsprong van de anisotropie kan worden verklaard door een anisotrope effectieve massa in het model met vrije elektronen te gebruiken. De resultaten toonden aan dat de gap-functie groter is in de richting van de zigzag en dat de piek rond de maximale kloof (Δ_{max}) zich bevindt in het BEC-regime langs de ‘armchair’ richting. Voor lage dichtheden zitten we in het overgangsregime van BEC, terwijl voor hoge dichtheden een BCS-achtige condensaat in de zigzag richting wordt gevonden. Belangrijk is dat de anisotrope hoge KT-overgangstemperatuur met maximale waarde tot $\sim$ 90K werd geschat in dubbellaags fosforeen in de zigzag richting, voor grote dichtheden tot 4×10^{12} cm^{-2}. Verder werd aangetoond dat de anisotropie-effecten in het vlak een belangrijke rol spelen in de superfluïditeit voor de overgang naar sterk gecorreleerde toestanden in een speciale richting. Het zou interessant zijn om dit effect experimenteel waar te nemen.

Kunnen we de ladingsdichtheidsgolven in een dubbele monolaag BP zien? Dit werd bestudeerd in hoofdstuk 8. Er werd bewezen dat de negatieve elektronische samendrukbaarheid van het dubbellaagse elektronenholte fosfeen systeem bij een haalbare dichtheid een CDW-fase mogelijk maakt dankzij een uniform krachtveld via de Coulomb-weerstand. De evenwichtsoplossingen wordt bekomen voor de sleeplaag gemodelleerd als een quasi-1D-systeem. Door gebruik te maken van de samendrukbaarheidssomregel waarin de samendrukbaarheid is gerelateerd aan de kleine momentum limiet van de dichtheidsresponsefunctie, werd een analytische uitdrukking verkregen voor de anisotrope sleepkracht. Het bleek dat de dichtheidsmodulatie niet alleen afhankelijk is van het teken van de samendrukbaarheid, maar ook van de anisotropie van het systeem. De amplitude van de CDW-fase hing af van de scheiding tussen de lagen en de temperatuur. De golflengte van de CDW kan ook elektrisch worden afgestemd door de waarde ervan te wijzigen. In een experiment kan dit worden gerealiseerd via een poort die de dichtheid van de passieve laag verandert. Er zijn een aantal manieren waarop een CDW-fase experimenteel kan worden geïdentificeerd [209]. Deze fase kan worden gedetecteerd door optische methoden, zoals differentiële absorptie of diffractie. Een STM kan de ladingsmodulatie, de periodieke vervorming van de atomaire positie en het openen van een opening in de toestandsdichtheid waarnemen. Daarnaast kan hoekopgeloste foto-emissiespectroscopie (ARPES) laten zien welke gedeelten van het Fermi-oppervlak worden weggewerkt door de CDW [210]. Dit kan aanwijzingen geven of het CDW wordt aangestuurd door Fermi-oppervlaktenesten of door iets exotischer [211]. Door een materiaal te verstoren met een ultrakorte laserpuls en de resulterende voorbijgaande ARPES-spectra te volgen, kan men inzicht verkrijgen in de dynamica van zowel de quasideeltjes als van de elektronische structuur zelf [212].

Appendix A

Drag resistivity tensor

Here, we present a derivation of Eq. (3.1) for the drag resistivity tensor in a rotationally misaligned double-layer electron gas system with anisotropic parabolic band structure by following closely the approach of Ref. [87]. We suppose that the intra-layer transport time is independent of the wave vector. So, in a 2D system with the energy dispersion of the form of Eq. (2.12), the effective mass, $\hat{M}$, transport time, $\hat{\tau}_t$, and mobility, $\hat{\mu}_t$, are symmetric and constant 2×2 tensors and are related by:

$$\hat{\mu}_t = e_i \hat{M}^{-1} \hat{\tau}_t. \tag{A.1}$$

We assume one layer (layer 1) is fixed and take its lattice principal axes along the laboratory coordinate system but the other layer (layer 2) is rotated by an angle τ. Hence, in the laboratory frame, $\hat{M}$, $\hat{\tau}_t$, and $\hat{\mu}_t$ have zero and non-zero off-diagonal elements in the fixed and rotated layers, respectively. In layer 2, these non-diagonal matrices can be expressed in terms of the diagonal ones by introducing the rotation matrix, $\hat{R}(\tau)$, *e.g.* for the effective mass tensor we have

$$\hat{M}_2 = \hat{R}(-\tau) \hat{M}_1 \hat{R}(\tau). \tag{A.2}$$

Since we are dealing with the symmetric effective mass and transport time tensors, each one is equal to its transpose. Moreover, due to the diagonal representations of these tensors in the laboratory frame, we have:

$$\hat{M}_i^{-1} \hat{\tau}_{t,i} = \hat{\tau}_{t,i} \hat{M}_i^{-1}. \tag{A.3}$$

In the Boltzmann transport equation framework, we define a deviation function $g(\mathbf{k})$ as

$$\delta f \equiv f(\mathbf{k}) - f^0(\mathbf{k}) = -k_B T \left(\frac{\partial f^0(\mathbf{k})}{\partial E_{\mathbf{k}}} \right) g(\mathbf{k}). \tag{A.4}$$

where $f(\mathbf{k})$ is the non-equilibrium Fermi distribution function and $f^0(\mathbf{k}) = f^0(E_{\mathbf{k}})$. The linearized interlayer collision integral is given by:

$$\begin{aligned} S[g_1, g_2](\mathbf{k_2}) =& 2\int \frac{d\mathbf{k_1}}{(2\pi)^2} \int \frac{d\mathbf{q}}{(2\pi)^2} w(\mathbf{q}, E_{\mathbf{k_1+q}} - E_{\mathbf{k_1}}) f_1^0(\mathbf{k_1}) f_2^0(\mathbf{k_2})[1 - f_1^0(\mathbf{k_1} + \mathbf{q})] \times \\ & [1 - f_2^0(\mathbf{k_2} - \mathbf{q})][g_1(\mathbf{k_1}) + g_2(\mathbf{k_2}) - g_1(\mathbf{k_1} + \mathbf{q}) - g_2(\mathbf{k_2} - \mathbf{q})] \times \\ & \delta(E_{\mathbf{k_1}} + E_{\mathbf{k_2}} - E_{\mathbf{k_1+q}} - E_{\mathbf{k_2-q}}), \end{aligned} \tag{A.5}$$

with $w(\mathbf{q}, \omega) = 4\pi\hbar^{-1}|U_{21}(\mathbf{q}, \omega)|^2$. Considering weak interlayer interaction, the coupled Boltzmann equations are given by:

$$e_1(\frac{\partial f_1^0}{\partial E})(\mathbf{v_1})^t.\mathbf{\Xi_1} = -\hat{H}_1[g_1](\mathbf{k_1}), \tag{A.6}$$

and

$$e_2(\frac{\partial f_2^0}{\partial E})(\mathbf{v_2})^t.\mathbf{\Xi_2} = -\hat{H}_2[g_2](\mathbf{k_2}) + S[g_1, g_2 = 0](\mathbf{k_2}), \tag{A.7}$$

where the superscript t means the transpose and $\mathbf{\Xi_i}$ and $\hat{H}_i$ are DC electric field and the negative of the linearized intra-layer collision operator in layer i, respectively. In a 2D semiconductor with anisotropic parabolic band structure, the electron velocity is simply related to the wave vector

$$\mathbf{v_i}(\mathbf{k_i}) = \hbar \hat{M}_i^{-1} \mathbf{k_i}. \tag{A.8}$$

From the above equations g_1 and g_2 can be obtained as:

$$g_1(\mathbf{k_1}) = -e_1 \hat{H}_1^{-1} \big[(\frac{\partial f_1^0}{\partial E})(\mathbf{v_1})^t \big](\mathbf{k_1}).\mathbf{\Xi_1}, \tag{A.9}$$

and

$$g_2(\mathbf{k_2}) = -e_2 \hat{H}_2^{-1} \big[(\frac{\partial f_2^0}{\partial E})(\mathbf{v_2})^t \big](\mathbf{k_2}).\mathbf{\Xi_2} + \hat{H}_2^{-1}[S](\mathbf{k_2}). \tag{A.10}$$

Since the current in layer 2 is equal to zero

$$\mathbf{J_2} = -2e_2 k_B T \int \frac{d\mathbf{k_2}}{(2\pi)^2}\Big((\frac{\partial f_2^0}{\partial E})\mathbf{v_2}\Big) g_2(\mathbf{k_2}) = 0, \tag{A.11}$$

one finds the following relation:

$$\begin{aligned} &2e_2^2 k_B T \int \frac{d\mathbf{k_2}}{(2\pi)^2}\Big((\frac{\partial f_2^0}{\partial E})\mathbf{v_2}\Big)\hat{H}_2^{-1}\big[(\frac{\partial f_2^0}{\partial E})(\mathbf{v_2})^t\big](\mathbf{k_2}).\mathbf{\Xi_2} = \\ &-2e_2 k_B T \int \frac{d\mathbf{k_2}}{(2\pi)^2}\Big((\frac{\partial f_2^0}{\partial E})\mathbf{v_2}\Big)\hat{H}_2^{-1}[S](\mathbf{k_2}). \end{aligned} \tag{A.12}$$

The left hand side of the above equation is equals to $n_2 e_2 \hat{\mu}_{t,2}.\mathbf{\Xi_2}$. By employing the following identities to Eq. (A.5)

$$\delta(E_{\mathbf{k_1}}+E_{\mathbf{k_2}}-E_{\mathbf{k_1+q}}-E_{\mathbf{k_2-q}}) = \hbar\int_0^\infty d\omega\,\delta(E_{\mathbf{k_1}}-E_{\mathbf{k_1+q}}-\hbar\omega)\delta(E_{\mathbf{k_2}}-E_{\mathbf{k_2-q}}+\hbar\omega). \tag{A.13}$$

and

$$f^0(E_1)[1-f^0(E_2)] = [f^0(E_2)-f^0(E_1)]n_B(E_1-E_2), \tag{A.14}$$

Eq.(A.12) can be rewritten as:

$$\begin{aligned} n_2 e_2 \hat{\mu}_{t,2}.\Xi_2 = &-\frac{4e_2 k_B T}{\pi}\int \frac{d\mathbf{q}}{(2\pi)^2}\int_0^\infty d\omega |U_{21}(\mathbf{q},\omega)|^2 n_B(\hbar\omega) n_B(-\hbar\omega) \\ &\times \Big[\int \frac{d\mathbf{k_2}}{(2\pi)^2}[f_2^0(\mathbf{k_2}) - f_2^0(\mathbf{k_2}+\mathbf{q})]\delta(E_{\mathbf{k_2}} - E_{\mathbf{k_2+q}} - \hbar\omega)\hat{H}_2^{-1}\big[(\frac{\partial f_2^0}{\partial E})\mathbf{v_2}\big](\mathbf{k_2})\Big] \\ &\times \Big[\int \frac{d\mathbf{k_1}}{(2\pi)^2}[f_1^0(\mathbf{k_1}) - f_1^0(\mathbf{k_1}+\mathbf{q})]\delta(E_{\mathbf{k_1}} - E_{\mathbf{k_1+q}} - \hbar\omega)[g_1(\mathbf{k_1}) - g_1(\mathbf{k_1}+\mathbf{q})]\Big]. \end{aligned} \tag{A.15}$$

where $n_B(\hbar\omega)$ is the Bose distribution function and in the second line we use the Hermitian property of H_2^{-1}. Using the relaxation time approximation, one can define:

$$g_i(\mathbf{k_i}) = -e_i \hat{H}_i^{-1}\big[(\frac{\partial f_i^0}{\partial E})(\mathbf{v_i})^t\big](k_i).\mathbf{\Xi_i} \equiv \frac{e_i\big(\hat{\tau}_{t,i}\mathbf{v_i}(\mathbf{k_i})\big)^t.\mathbf{\Xi}_i}{k_B T}. \tag{A.16}$$

Hence, Eq. (A.15) can be written as:

$$
\begin{aligned}
&n_2 e_2 \hat{\mu}_{t,2}.\mathbf{\Xi}_2 = -\frac{4e_2 k_B T}{\pi}\int \frac{d\mathbf{q}}{(2\pi)^2}\int_0^\infty d\omega |U_{21}(\mathbf{q},\omega)|^2 n_B(\hbar\omega) n_B(-\hbar\omega)\\
&\times\left[\frac{1}{2k_BT}\int\frac{d\mathbf{k_2}}{(2\pi)^2}[f_2^0(\mathbf{k_2})-f_2^0(\mathbf{k_2}+\mathbf{q})]\delta(E_{\mathbf{k_2}}-E_{\mathbf{k_2}+\mathbf{q}}-\hbar\omega)]\hat{\tau}_{t,2}[\mathbf{v}_2(\mathbf{k_2}+\mathbf{q})-\mathbf{v}_2(\mathbf{k_2})]\right]\\
&\times\left[\frac{e_1}{k_BT}\int\frac{d\mathbf{k_1}}{(2\pi)^2}[f_1^0(\mathbf{k_1})-f_1^0(\mathbf{k_1}+\mathbf{q})]\delta(E_{\mathbf{k_1}}-E_{\mathbf{k_1}+\mathbf{q}}-\hbar\omega)\right.\\
&\left.\times\left(\hat{\tau}_{t,1}[\mathbf{v}_1(\mathbf{k_1}+\mathbf{q})-\mathbf{v}_1(\mathbf{k_1})]\right)^t.\mathbf{\Xi}_1\right],
\end{aligned}
\tag{A.17}
$$

The DC electric fields in the two layers are related by:

$$
\mathbf{\Xi}_2 = \hat{\rho}_{21}\mathbf{J}_1 = n_1 e_1 \hat{\rho}_{21}\hat{\mu}_{t,1}.\mathbf{\Xi}_1. \tag{A.18}
$$

Inserting Eqs. (A.8) and (A.18) into Eq. (A.15) and considering the properties of effective mass and transport time tensors, one gets:

$$
\begin{aligned}
&n_1 e_1 n_2 e_2 \hat{\mu}_{t,2}\hat{\rho}_{21}\hat{\mu}_{t,1}.\mathbf{\Xi}_1 = -\frac{4e_2 k_B T}{\pi}\int \frac{d\mathbf{q}}{(2\pi)^2}\int_0^\infty d\omega |U_{21}(\mathbf{q},\omega)|^2 n_B(\hbar\omega) n_B(-\hbar\omega)\\
&\times\left[\frac{\hat{\tau}_{t,2}\hat{M}_2^{-1}\hat{R}(-\tau)\mathbf{q}}{2k_BT}\int\frac{d\mathbf{k_2}}{(2\pi)^2}[f_2^0(\mathbf{k_2})-f_2^0(\mathbf{k_2}+\mathbf{q})]\delta(E_{\mathbf{k_2}}-E_{\mathbf{k_2}+\mathbf{q}}-\hbar\omega)]\right]\\
&\times\left[\frac{\mathbf{q}^t e_1\hat{M}_1^{-1}\hat{\tau}_{t,1}.\mathbf{\Xi}_1}{k_BT}\int\frac{d\mathbf{k_1}}{(2\pi)^2}[f_1^0(\mathbf{k_1})-f_1^0(\mathbf{k_1}+\mathbf{q})]\delta(E_{\mathbf{k_1}}-E_{\mathbf{k_1}+\mathbf{q}}-\hbar\omega)\right].
\end{aligned}
\tag{A.19}
$$

By multiplying both sides of the above equation by $\hat{\mu}_{t,2}^{-1}$ and using the mobility relation, Eq. (A.1), commutative property Eq. (A.16) and the equality $4n_B(\hbar\omega)n_B(-\hbar\omega) = -\sinh^{-2}(\hbar\omega/2k_BT)$, Eq. (A.19) can be written as:

$$
\begin{aligned}
\rho_{21}^{\alpha\beta} = &\frac{\hbar^2}{2\pi n_1 e_1 n_2 e_2 k_B T}\int\frac{d\mathbf{q}}{(2\pi)^2}q_\alpha q_\beta\int_0^\infty d\omega\frac{|U_{21}(\mathbf{q},\omega)|^2}{\sinh^2(\hbar\omega/2k_BT)}\\
&\times\left[\int\frac{d\mathbf{k_1}}{(2\pi)^2}[f_1^0(\mathbf{k_1})-f_1^0(\mathbf{k_1}+\mathbf{q})]\delta(E_{\mathbf{k_1}}-E_{\mathbf{k_1}+\mathbf{q}}-\hbar\omega)\right]\\
&\times\left[\int\frac{d\mathbf{k_2}}{(2\pi)^2}[f_2^0(\mathbf{k_2})-f_2^0(\mathbf{k_2}+\mathbf{q})]\delta(E_{\mathbf{k_2}}-E_{\mathbf{k_2}+\mathbf{q}}-\hbar\omega)\right],
\end{aligned}
\tag{A.20}
$$

where q_α and q_β are the α and β components of the transferred wave vector corresponding to layer 1 and layer 2 in the laboratory frame, respectively. Finally by using the definition of the polarizability function , Eq. (8.15), one obtains the Eq.(3.1).

Appendix B

Electron-SO phonon modes

B.1 Monolayer phosphorene

Inserting Eq. (3.5) into Eq. (5.11), we have:

$$\epsilon(\omega, q, \theta) = 1 - \frac{\omega^2_{pl}(q, \theta)}{\omega^2(q, \theta)} + \sum_{\lambda} \frac{\alpha e^{-2qz}}{1 - \alpha e^{-2qz} - \omega^2(q, \theta)/(\omega^\lambda_{so})^2}. \tag{B.1}$$

From the zeros of dielectric function (here we drop the q and θ for simplicity):

$$\omega^2(\omega^2 - (\omega^\lambda_{SO})^2) - \omega^2_{pl}(\omega^2 - (\omega^\lambda_{SO})^2) - \omega^2_{pl}(\omega^\lambda_{SO})^2\alpha e^{-2qz} = 0, \tag{B.2}$$

the coupled plasmon-SO phonon modes are obtained as:

$$(\omega^\lambda_{(\pm)})^2 = \frac{1}{2}\Bigg[\big((\omega^\lambda_{SO})^2 + \omega^2_{pl}\big) \pm \big[((\omega^\lambda_{SO})^2 - \omega^2_{pl}) + 4\omega^2_{pl}(\omega^\lambda_{SO})^2\alpha e^{-2qz}\big]^{1/2}\Bigg]. \tag{B.3}$$

By Taylor expanding the right hand side of Eq. (B.3), we get:

$$\omega^\lambda_{(+)}(q, \theta) = \omega^\lambda_{so}\big(1 + \alpha e^{-2qz}\frac{\omega^2_{pl}}{(\omega^\lambda_{so})^2 - \omega^2_{pl}}\big), \tag{B.4}$$

$$\omega^\lambda_{(-)}(q, \theta) = \omega_{pl}\big(1 - \frac{\alpha e^{-2qz}}{2}\frac{(\omega^\lambda_{so})^2}{(\omega^\lambda_{so})^2 - \omega^2_{pl}}\big). \tag{B.5}$$

Since $\omega_{pl} \to 0$ in the long-wavelength limit, one can safely ignore ω_{pl} in the denominator of the above equations and obtain Eqs. (5.12) and (5.13).

B.2 Double-layer phosphorene

Here, we calculate the coupled plasmon-SO phonon modes in double-layer systems with anisotropic band structure. In such systems, the rotation of one layer with respect to the other should be considered. In order to determine the dispersion relation of the coupled modes, we need to calculate the zeros of the determinant of the total dielectric matrix (Eq. (5.6)) in the long-wavelength limit:

$$\begin{aligned}\epsilon(\omega,q,\theta) = 1 &- (R_1(\theta)+R_2(\theta))\Pi'(q,\omega)U_0(q,\omega)\\ &+ (U_0(q,\omega)\Pi'(q,\omega))^2 R_1(\theta)R_2(\theta)(1-e^{-2qd_{12}}),\end{aligned} \tag{B.6}$$

where $\Pi'(\omega,q,\theta)=\Pi_i(\omega,q,\theta)/R_i(\theta)$. After some algebra, we get the following relation:

$$\begin{aligned}\epsilon(\omega,q,\theta) = U_0^2(q,\omega)(2qd_{12})R_1(\theta)R_2(\theta)[\Pi'(\omega,q,\theta)-\Pi_+(\omega,q,\theta)]\\ \times[\Pi'(\omega,q,\theta)-\Pi_-(\omega,q,\theta)],\end{aligned} \tag{B.7}$$

where Π_+ and Π_- are defined as

$$\Pi_+(\omega,q,\theta) = \frac{R_1(\theta)+R_2(\theta)}{(R_1(\theta)R_2(\theta)U_0(q,\omega)2qd_{12}}, \tag{B.8}$$

and

$$\Pi_-(\omega,q,\theta) = \frac{1}{(R_1(\theta)+R_2(\theta))U_0(q,\omega)}. \tag{B.9}$$

The dispersion relation of the couple modes is given by $\Pi'(\omega,q,\theta)=\Pi_\pm(\omega,q,\theta)$. Using the Eqs. (5.4-5.9) in the $\Pi'(\omega,q,\theta)=\Pi_+(\omega,q,\theta)$ condition, we get:

$$\omega^2\big(\omega^2-(\omega^\lambda_{SO})^2\big)-q^2 f_{ac}(\theta)\big[\omega^2-(\omega^\lambda_{SO})^2+(\omega^\lambda_{SO})^2\alpha e^{-2qz}\big]=0 \tag{B.10}$$

where $f_{ac}(\theta)$ is defined as:

$$f_{ac}(\theta) = \frac{4\pi n e^2 d_{12}}{\epsilon_\infty}\frac{R_1(\theta)R_2(\theta)}{R_1(\theta)+R_2(\theta)}. \tag{B.11}$$

After some algebra, we obtain the following relation:

$$(\omega^\lambda_{ac(\pm)})^2 = \frac{(\omega^\lambda_{so})^2+q^2 f_{ac}(\theta)}{2} \pm \sqrt{\frac{\big((\omega^\lambda_{SO})^2-q^2 f_{ac}(\theta)\big)^2+4q^2 f_{ac}(\theta)(\omega^\lambda_{SO})^2\alpha e^{-2qz}}{4}}, \tag{B.12}$$

which can be simplified in the long-wavelength limit as:

$$(\omega^{\lambda}_{ac(+)})^2 = (\omega^{\lambda}_{so})^2\left[1 + \frac{f_{ac}(\theta)q^2\alpha e^{-2qz}}{(\omega^{\lambda}_{so})^2}\right], \tag{B.13}$$

and

$$(\omega^{\lambda}_{ac(-)})^2 = f_{ac}(\theta)q^2[1 - \alpha e^{-2qz}]. \tag{B.14}$$

Substituting the relation for $f_{ac}(\theta)$ in above relations, one obtains Eqs. (5.17) and (5.18) for the coupled acoustic modes. In the case of the coupled optical modes, we use the $\Pi'(q,\omega) = \Pi_{-}(q,\omega)$ condition and get the following equation:

$$\begin{aligned}\omega^2\big(\omega^2 - (\omega^{\lambda}_{so})^2\big) - f_{op}(\theta)\big[\omega^2 \\ - (\omega^{\lambda}_{so})^2 + (\omega^{\lambda}_{so})^2\alpha e^{-2qz}\big] = 0\end{aligned} \tag{B.15}$$

where $f_{op}(\theta)$ is given by:

$$f_{op}(\theta) = \frac{2\pi n e^2}{\epsilon_\infty}\big(R_1(\theta) + R_2(\theta)\big). \tag{B.16}$$

Solving Eq. (B.15) yields:

$$(\omega^{\lambda}_{op(\pm)})^2 = \frac{(\omega^{\lambda}_{so})^2 + q f_{op}(\theta)}{2} \pm \sqrt{\frac{\big((\omega^{\lambda}_{so})^2 - q f_{op}(\theta)\big)^2 - 4q f_{op}(\theta)(\omega^{\lambda}_{so})^2(1 - \alpha e^{-2qz})}{4}}. \tag{B.17}$$

In the long-wavelength limit, we end up with the following expressions for the coupled optical modes:

$$(\omega^{\lambda}_{op(+)})^2 = (\omega^{\lambda}_{so})^2\left[1 + \frac{q f_{op}(\theta)\alpha e^{-2qz}}{(\omega^{\lambda}_{so})^2}\right] \tag{B.18}$$

and

$$(\omega^{\lambda}_{op(-)})^2 = q f_{op}(\theta)[1 - \alpha e^{-2qz}]. \tag{B.19}$$

Finally, by inserting $f_{op}(\theta)$ into Eqs. (B.18) and (B.19) one obtains Eqs. (5.19) and (5.20).

Bibliography

[1] R. V. Gorbachev, A. K. Geim, M. I. Katsnelson, K. S. Novoselov, T. Tudorovskiy, I. V. Grigorieva, A. H. MacDonald, S. V. Morozov, K. Watanabe, T. Taniguchi, and L. A. Ponomarenko, “Strong Coulomb drag and broken symmetry in double-layer graphene,” *Nature Physics*, vol. 8, pp. 896–901, 2012.

[2] D. Pesin and A. H. MacDonald, “Spintronics and pseudospintronics in graphene and topological insulators,” *Nature Materials*, vol. 11, pp. 409–416, 2012.

[3] A. K. Geim and I. V. Grigorieva, “Van der Waals heterostructures,” *Nature*, vol. 499, pp. 419–425, 2013.

[4] Q. H. Wang, K. Kalantar-Zadeh, A. Kis, J. N. Coleman, and M. S. Strano, “Electronics and optoelectronics of two-dimensional transition metal dichalcogenides,” *Nature Nanotechnology*, vol. 7, pp. 699–712, 2012.

[5] Y. M. Xiao, W. Xu, B. Van Duppen, and F. M. Peeters, “Infrared to terahertz optical conductivity of n-type and p-type monolayer MoS_2 in the presence of Rashba spin-orbit coupling,” *Phys. Rev. B*, vol. 94, p. 155432, Oct 2016.

[6] W. Zhao, Q. Wu, Q. Hao, J. Wang, M. Li, Y. Zhang, K. Bi, Y. Chen, and Z. Ni, “Plasmon–phonon coupling in monolayer Ws2,” *Appl. Phys. Lett.*, vol. 108, no. 13, pp. –, 2016.

[7] R. A. Doganov, S. P. Koenig, Y. Yeo, K. Watanabe, T. Taniguchi, and B. Özyilmaz, "Transport properties of ultrathin black phosphorus on hexagonal boron nitride," *Appl. Phys. Lett.*, vol. 106, no. 8, pp. –, 2015.

[8] M. Zarenia, A. Perali, D. Neilson, and F. Peeters, "Enhancement of electron-hole superfluidity in double few-layer graphene," *Scientific Reports*, vol. 4, p. 7319, 2014.

[9] B. Sa, Y.-L. Li, Z. Sun, J. Qi, C. Wen, and B. Wu, "The electronic origin of shear-induced direct to indirect gap transition and anisotropy diminution in phosphorene," *Nanotechnology*, vol. 26, no. 21, p. 215205, 2015.

[10] K. F. Mak, C. Lee, J. Hone, J. Shan, and T. F. Heinz, "Atomically thin MoS_2: A new direct-gap semiconductor," *Phys. Rev. Lett.*, vol. 105, p. 136805, Sep 2010.

[11] Y. Zhang, Y.-W. Tan, H. L. Stormer, and P. Kim, "Experimental observation of the quantum Hall effect and Berry's phase in graphene," *Nature*, vol. 438, pp. 201–204, 2005.

[12] X. Gan, "Strong enhancement of light-matter interaction in graphene coupled to a photonic crystal nanocavity," *Nano Lett.*, vol. 12, no. 11, pp. 5626–5631, 2012.

[13] G. Eda and S. A. Maier, "Two-dimensional crystals: Managing light for optoelectronics," *ACS nano*, vol. 7, no. 7, pp. 5660–5665, 2013.

[14] F. Xia, H. Wang, D. Xiao, and .M Dubey "Two-dimensional material nanophotonics," *Nature Photonics*, vol. 8, pp. 899–907, 2014.

[15] M. Ishigami, J. Chen, W. Cullen, M. Fuhrer, and E. Williams, "Atomic structure of graphene on SiO_2," *Nano Lett.*, vol. 7, no. 6, pp. 1643–1648, 2007.

[16] F. Schwierz, "Graphene transistors," *Nature Nanotechnology*, vol. 5, pp. 487–496, 2010.

[17] B. Radisavljevic, A. Radenovic, J. Brivio, V. Giacometti, and A. Kis, "Single-layer MoS_2 transistors," *Nature Nanotechnology*, vol. 6, pp. 147–150, 2010.

[18] R. Fivaz and E. Mooser, "Mobility of charge carriers in semiconducting layer structures," *Phys. Rev.*, vol. 163, pp. 743–755, Nov 1967.

[19] K. Bolotin, K. Sikes, Z. Jiang, M. Klima, G. Fudenberg, J. Hone, P. Kim, and H. Stormer, "Ultrahigh electron mobility in suspended graphene," *Solid State Communications*, vol. 146, no. 9, pp. 351–355, 2008.

[20] C. R. Dean A. F. Young, I. Meric, C. Lee, L. Wang, S. Sorgenfrei, K. Watanabe, T. Taniguchi, P. Kim, K. L. Shepard and J. Hone, "Boron nitride substrates for high-quality graphene electronics, "*Nature Nanotechnology*, vol. 5, pp. 722–726, 2010.

[21] A. Carvalho, M. Wang, X. Zhu, A. S. Rodin, H. Su, and A. H. C. Neto, "Phosphorene: from theory to applications," *Nature Reviews Materials*, vol. 1,no. 16061, 2016.

[22] X. Ling, H. Wang, S. Huang, F. Xia, and M. S. Dresselhaus, "The renaissance of black phosphorus, "*Proc. Natl. Acad. Sci. U.S.A.*, vol. 112, no. 15, pp. 4523–4530, 2015.

[23] E. Taghizadeh Sisakht, F. Fazileh, M. H. Zare, M. Zarenia, and F. M. Peeters, "Strain-induced topological phase transition in phosphorene and in phosphorene nanoribbons," *Phys. Rev. B*, vol. 94, p. 085417, 2016.

[24] M. Zare, B. Z. Rameshti, F. G. Ghamsari, and R. Asgari, "Thermoelectric transport in monolayer phosphorene," *Phys. Rev. B*, vol. 95, p. 045422, 2017.

[25] S. Brener, A. N. Rudenko, and M. I. Katsnelson, "Effect of flexural phonons on the hole states in single-layer black phosphorus," *Phys. Rev. B*, vol. 95, p. 041406, Jan 2017.

[26] R. W. Keyes, "The electrical properties of black phosphorus," *Phys. Rev.*, vol. 92, pp. 580–584, 1953.

[27] J. C. Jamieson, "Crystal structures adopted by black phosphorus at high pressures," *Science*, vol. 139, pp. 1291–1292, 1963.

[28] P. W. Bridgman, “Two new modifications of phosphorus,” *J. Am. Chem. Soc.*, vol. 36, p. 1344–1363, 1914.

[29] S. Appalakondaiah, G. Vaitheeswaran, S. Lebègue, N. E. Christensen, and A. Svane, “Effect of van der Waals interactions on the structural and elastic properties of black phosphorus,” *Phys. Rev. B*, vol. 86, p. 035105, 2012.

[30] L. Li, J. Kim, C. Jin, G. J. Ye, D. Y. Qiu, F. H. Jornada, Z. Shi, L. Chen, Z. Zhang, F. Yang, K. Watanabe, T. Taniguchi, W. Ren, S. G. Louie, X. H. Chen, Y. Zhang and F. Wang, “Direct observation of the layer-dependent electronic structure in phosphorene,” *Nat. Nanotechnol*, vol. 12, pp. 21–25, 2017.

[31] L. Li, Y. Yu, G. J. Ye, Q. Ge, X. Ou, H. Wu, D. Feng, X. H. Chen, and Y. Zhang, “Black phosphorus field-effect transistors,” *Nat. Nanotechnol.*, vol. 9, pp. 372–377, 2014.

[32] F. Xia, H. Wang, and Y. Jia, “Rediscovering black phosphorus as an anisotropic layered material for optoelectronics and electronics,” *Nat. Commun.*, vol. 5, pp. 4458–, 2014.

[33] V. Tran, R. Soklaski, Y. Liang, and L. Yang, “Layer-controlled band gap and anisotropic excitons in few-layer black phosphorus,” *Phys. Rev. B*, vol. 89, p. 235319, 2014.

[34] S. Bohloul, L. Zhang, K. Gong, and H. Guo, “Theoretical impurity-limited carrier mobility of monolayer black phosphorus,” *Appl. Phys. Lett.*, vol. 108, no. 3, pp. 033508 , 2016.

[35] H. Liu, A. T. Neal, Z. Zhu, Z. Luo, X. Xu, D. Tománek, and P. D. Ye, “Phosphorene: an unexplored 2D semiconductor with a high hole mobility,” *ACS Nano*, vol. 8, no. 4, pp. 4033–4041, 2014.

[36] B. Ostahie and A. Aldea, “Phosphorene confined systems in magnetic field, quantum transport, and superradiance in the quasiflat band,” *Phys. Rev. B*, vol. 93, p. 075408, 2016.

[37] J. E. Padilha, A. Fazzio, and A. J. R. da Silva, “van der Waals heterostructure of phosphorene and graphene: Tuning the Schottky barrier and doping by electrostatic gating,” *Phys. Rev. Lett.*, vol. 114, p. 066803, 2015.

[38] D. Cakir, H. Sahin, and F. M. Peeters, "Tuning of the electronic and optical properties of single-layer black phosphorus by strain," *Phys. Rev. B*, vol. 90, p. 205421, 2014.

[39] X. Wang, A. M. Jones, K. L. Seyler, V. Tran, Y. Jia, H. Zhao, H. Wang, L. Yang, X. Xu, and F. Xia, "Highly anisotropic and robust excitons in monolayer black phosphorus," *Nat. Nanotechnol.*, vol. 10, pp. 517–521, 2015.

[40] S. Saberi-Pouya, T. Vazifehshenas, T. Salavati-fard, M. Farmanbar, and F. M. Peeters, "Strong anisotropic optical conductivity in two-dimensional puckered structures: The role of the Rashba effect," *Phys. Rev. B*, vol. 96, p. 075411, 2017.

[41] J. Qiao, X. Kong, Z.-X. Hu, F. Yang, and W. Ji, "High-mobility transport anisotropy and linear dichroism in few-layer black phosphorus," *Nat. Commun.*, vol. 5, pp. 4458 –, 2014.

[42] D. A. Prishchenko, V. G. Mazurenko, M. I. Katsnelson, and A. N. Rudenko, "Coulomb interactions and screening effects in few-layer black phosphorus: a tight-binding consideration beyond the long-wavelength limit," *2D Materials*, vol. 4, no. 2, p. 025064, 2017.

[43] S. Saberi-Pouya, T. Vazifehshenas, T. Salavati-fard, and M. Farmanbar, "Anisotropic hybrid excitation modes in monolayer and double-layer phosphorene on polar substrates," *Phys. Rev. B*, vol. 96, p. 115402, Sep 2017.

[44] T. Low, R. Roldán, H. Wang, F. Xia, P. Avouris, L. M. Moreno, and F. Guinea, "Plasmons and screening in monolayer and multilayer black phosphorus," *Phys. Rev. Lett.*, vol. 113, p. 106802, Sep 2014.

[45] F. Jin, R. Roldán, M. I. Katsnelson, and S. Yuan, "Screening and plasmons in pure and disordered single- and bilayer black phosphorus," *Phys. Rev. B*, vol. 92, p. 115440, Sep 2015.

[46] A. S. Rodin and A. H. Castro Neto, "Collective modes in anisotropic double-layer systems," *Phys. Rev. B*, vol. 91, p. 075422, Feb 2015.

[47] S. Saberi-Pouya, T. Vazifehshenas, M. Farmanbar, and T. Salavati-fard, "Coulomb drag in anisotropic systems: a theoretical study on

a double-layer phosphorene," *Journal of Physics: Condensed Matter*, vol. 28, no. 28, p. 285301, 2016.

[48] S. Zhang, J. Yang, R. Xu, F. Wang, W. Li, M. Ghufran, Y. W. Zhang, Z. Yu, G. Zhang, Q. Qin, and Y. Lu, "Extraordinary photoluminescence and strong temperature/angle-dependent raman responses in few-layer phosphorene," *ACS nano*, vol. 8, no. 9, pp. 9590–9596, 2014.

[49] J. Yang and Y. Lu, "Optical properties of phosphorene," *Chinese Physics B*, vol. 26, no. 3, p. 034201, 2017.

[50] T. Low, A. S. Rodin, A. Carvalho, Y. Jiang, H. Wang, F. Xia, and A. H. Castro Neto, "Tunable optical properties of multilayer black phosphorus thin films," *Phys. Rev. B*, vol. 90, p. 075434, 2014.

[51] K. F. Mak, M. Y. Sfeir, Y. Wu, C. H. Lui, J. A. Misewich, and T. F. Heinz, "Measurement of the optical conductivity of graphene," *Phys. Rev. Lett.*, vol. 101, p. 196405, 2008.

[52] D. Akinwande, C. J. Brennan, J. S. Bunch, P. Egberts, J. R. Felts, H. Gao, R. Huang, J.-S. Kim, T. Li, Y. Li, K. M. Liechti, N. Lu, H. S. Park, E. J. Reed, P. Wang, B. I. Yakobson, T. Zhang, Y.-W. Zhang, Y. Zhou, and Y. Zhu, "A review on mechanics and mechanical properties of 2D materials—graphene and beyond," *Extreme Mechanics Letters*, vol. 13, no. Supplement C, pp. 42 – 77, 2017.

[53] D. G. Papageorgiou, I. A. Kinloch, and R. J. Young, "Mechanical properties of graphene and graphene-based nanocomposites," *Progress in Materials Science*, vol. 90, no. Supplement C, pp. 75 – 127, 2017.

[54] J.-W. Jiang and H. S. Park, "Mechanical properties of single-layer black phosphorus," *Journal of Physics D: Applied Physics*, vol. 47, no. 38, p. 385304, 2014.

[55] X. Peng, Q. Wei, and A. Copple, "Strain-engineered direct-indirect band gap transition and its mechanism in two-dimensional phosphorene," *Phys. Rev. B*, vol. 90, p. 085402, Aug 2014.

[56] J. Tao, W. Shen, S. Wu, L. Liu, Z. Feng, C. Wang, C. Hu, P. Yao, H. Zhang, W. Pang, X. Duan, J. Liu, C. Zhou, and D. Zhang,

"Mechanical and electrical anisotropy of few-layer black phosphorus," *ACS Nano*, vol. 9, no. 11, pp. 11362–11370, 2015.

[57] J.-W. Jiang and H. S. Park, "Negative poisson's ratio in single-layer black phosphorus," *Nature Communications*, vol. 5, no. 4727, 2014.

[58] A. Morita, "Semiconducting black phosphorus," *Applied Physics A*, vol. 39, pp. 227–242, 1986.

[59] A. S. Rodin, A. Carvalho, and A. H. Castro Neto, "Strain-induced gap modification in black phosphorus," *Phys. Rev. Lett.*, vol. 112, p. 176801, 2014.

[60] R. Winkler, *Spin-orbit Coupling Effects in Two-Dimensional Electron and Hole Systems.* Springer Berlin Heidelberg, 2003.

[61] Y. Liu, T. Low, and P. P. Ruden, "Mobility anisotropy in monolayer black phosphorus due to scattering by charged impurities," *Phys. Rev. B*, vol. 93, p. 165402, 2016.

[62] D. Bohm and D. Pines, "A collective description of electron interactions: III. Coulomb interactions in a degenerate electron gas," *Phys. Rev.*, vol. 92, pp. 609–625, 1953.

[63] N. Ashcroft and N. Mermin, *Solid State Physics.* Philadelphia: Saunders College, 1976.

[64] T. Low, A. S. Rodin, A. Carvalho, Y. Jiang, H. Wang, F. Xia, and A. H. Castro Neto, "Tunable optical properties of multilayer black phosphorus thin films," *Phys. Rev. B*, vol. 90, p. 075434, 2014.

[65] S. M. Badalyan and F. M. Peeters, "Enhancement of Coulomb drag in double-layer graphene structures by plasmons and dielectric background inhomogeneity," *Phys. Rev. B*, vol. 86, p. 121405, 2012.

[66] E. H. Hwang and S. Das Sarma, "Plasmon modes of spatially separated double-layer graphene," *Phys. Rev. B*, vol. 80, p. 205405, 2009.

[67] M. Jonson, "Electron correlations in inversion layers," *J. Phys. C: Sol. State Phys.*, vol. 9, no. 16, p. 3055, 1976.

[68] R. F. Egerton, "Electron energy-loss spectroscopy in the TEM," *Reports on Progress in Physics*, vol. 72, no. 1, p. 016502, 2009.

[69] T. Eberlein, U. Bangert, R. R. Nair, R. Jones, M. Gass, A. L. Bleloch, K. S. Novoselov, A. Geim, and P. R. Briddon, "Plasmon spectroscopy of free-standing graphene films," *Phys. Rev. B*, vol. 77, p. 233406, Jun 2008.

[70] S. C. Liou, C.-S. Shie, C. H. Chen, R. Breitwieser, W. W. Pai, G. Y. Guo, and M.-W. Chu, "π-plasmon dispersion in free-standing graphene by momentum-resolved electron energy-loss spectroscopy," *Phys. Rev. B*, vol. 91, p. 045418, 2015.

[71] P. Johari and V. B. Shenoy , "Tunable Dielectric Properties of Transition Metal Dichalcogenides," *ACS Nano*, vol. 5, p. 5903—5908, 2011.

[72] R. Schuster, J. Trinckauf, C. Habenicht, M. Knupfer, and B. Büchner, "Anisotropic particle-hole excitations in black phosphorus," *Phys. Rev. Lett.*, vol. 115, p. 026404, Jul 2015.

[73] L. Shulenburger, A. Baczewski, Z. Zhu, J. Guan, and D. Tománek, "The nature of the interlayer interaction in bulk and few-layer phosphorus," *Nano Lett.*, vol. 15, no. 12, pp. 8170–8175, 2015.

[74] T. Vazifehshenas, T. Amlaki, M. Farmanbar, and F. Parhizgar, "Temperature effect on plasmon dispersions in double-layer graphene systems," *Physics Letters A*, vol. 374, no. 48, pp. 4899 – 4903, 2010.

[75] R. Roldán and L. Brey, "Dielectric screening and plasmons in AA-stacked bilayer graphene," *Phys. Rev. B*, vol. 88, p. 115420, Sep 2013.

[76] B. Tanatar and A. K. Das, "Self-consistent theory of localization and Coulomb drag effect," *Phys. Rev. B*, vol. 61, pp. 15959–15964, 2000.

[77] T. Vazifehshenas and A. Eskourchi, "Thickness effects on the Coulomb drag rate in double quantum layer systems," *Physica E*, vol. 36, no. 2, p. 147–152, 2007.

[78] A. Gamucci, D. Spirito, M. Carrega, B. Karmakar, A. Lombardo, M. Bruna, L. N. Pfeiffer, K. W. West, A. C. Ferrari, M. Polini, and V. Pellegrini, "Anomalous low-temperature Coulomb drag in graphene-GaAs heterostructures," *Nat. Commun.*, vol. 5, no. 5824, 2014.

[79] K. Flensberg and B. Y.-K. Hu, "Coulomb drag as a probe of coupled plasmon modes in parallel quantum wells," *Phys. Rev. Lett.*, vol. 73, pp. 3572–3575, 1994.

[80] P. M. Solomon, P. J. Price, D. J. Frank, and D. C. La Tulipe, "New phenomena in coupled transport between 2D and 3D electron-gas layers," *Phys. Rev. Lett.*, vol. 63, pp. 2508–2511, 1989.

[81] A.-P. Jauho and H. Smith, "Coulomb drag between parallel two-dimensional electron systems," *Phys. Rev. B*, vol. 47, pp. 4420–4428, Feb 1993.

[82] C. P. Weber, N. Gedik, J. E. Moore, J. Orenstein, J. Stephens, and D. D. Awschalom, "Observation of spin Coulomb drag in a two-dimensional electron gas," *Nature*, vol. 437, pp. 1330–1333, 2005.

[83] A. F. Croxall, K. Das Gupta, C. A. Nicoll, M. Thangaraj, H. E. Beere, I. Farrer, D. A. Ritchie, and M. Pepper, "Anomalous Coulomb drag in electron-hole bilayers," *Phys. Rev. Lett.*, vol. 101, p. 246801, 2008.

[84] E. H. Hwang, R. Sensarma, and S. Das Sarma, "Coulomb drag in monolayer and bilayer graphene," *Phys. Rev. B*, vol. 84, p. 245441, Dec 2011.

[85] M. Carrega, T. Tudorovskiy, A. Principi, M. I. Katsnelson, and M. Polini, "Theory of Coulomb drag for massless Dirac fermions," *New J. Phys.*, vol. 14, no. 6, p. 063033, 2012.

[86] M. Ezawa, "Highly anisotropic physics in phosphorene," *J. Phys.: Conf. Ser.*, vol. 603, no. 1, p. 012006, 2015.

[87] K. Flensberg and B. Y.-K. Hu, "Plasmon enhancement of Coulomb drag in double-quantum-well systems," *Phys. Rev. B*, vol. 52, pp. 14796–14808, Nov 1995.

[88] M. I. Katsnelson, "Coulomb drag in graphene single layers separated by a thin spacer," *Phys. Rev. B*, vol. 84, p. 041407, 2011.

[89] L. Zheng and A. H. MacDonald, "Coulomb drag between disordered two-dimensional electron-gas layers," *Phys. Rev. B*, vol. 48, pp. 8203–8209, 1993.

[90] K. Flensberg, B. Y.-K. Hu, A.-P. Jauho, and J. M. Kinaret, "Linear-response theory of Coulomb drag in coupled electron systems," *Phys. Rev. B*, vol. 52, pp. 14761–14774, Nov 1995.

[91] X. Chen, Y. Wu, Z. Wu, Y. Han, S. Xu, L. Wang, W. Ye, T. Han, Y. He, Y. Cai, and N. Wang, "High-quality sandwiched black phosphorus heterostructure and its quantum oscillations," *Nat. Commun.*, vol. 6, no. 7315, 2015.

[92] H. Zhu, S. McDonnell, X. Qin, A. Azcatl, L. Cheng, R. Addou, J. Kim, P. D. Ye, and R. M. Wallace, "Al_2O_3 on Black Phosphorus by Atomic Layer Deposition: An in Situ Interface Study," *ACS. Appl. Mater. Inter.*, vol. 7, no. 23, pp. 13038–13043, 2015.

[93] T. J. Gramila, J. P. Eisenstein, A. H. MacDonald, L. N. Pfeiffer, and K. W. West, "Mutual friction between parallel two-dimensional electron systems," *Phys. Rev. Lett.*, vol. 66, pp. 1216–1219, 1991.

[94] L. Świerkowski, J. Szymański, and Z. W. Gortel, "Coupled electron-hole transport: Beyond the mean field approximation," *Phys. Rev. Lett.*, vol. 74, pp. 3245–3248, 1995.

[95] X. Luo, Y. Rahbarihagh, J. Hwang, H. Liu, Y. Du, and P. Ye, "Temporal and Thermal Stability of Al_2O_3-Passivated Phosphorene MOSFETs," *Electron Device Letters, IEEE*, vol. 35, pp. 1314–1316, 2014.

[96] I. Žutić, J. Fabian, and S. Das Sarma, "Spintronics: Fundamentals and applications," *Rev. Mod. Phys.*, vol. 76, pp. 323–410, 2004.

[97] K. V. Shanavas and S. Satpathy, "Electric field tuning of the Rashba effect in the polar perovskite structures," *Phys. Rev. Lett.*, vol. 112, p. 086802, 2014.

[98] V. Galitski and I. B. Spielman, "Spin-orbit coupling in quantum gases," *Nature*, vol. 494, pp. 49–54, 2013.

[99] G. Dresselhaus, "Spin-orbit coupling effects in zinc blende structures," *Phys. Rev.*, vol. 100, pp. 580–586, 1955.

[100] E. I. Rashba, "Properties of semiconductors with an extremum loop. 1. Cyclotron and combinational resonance in a magnetic field perpendicular to the plane of the loop," *Sov. Phys. Solid State*, vol. 2, pp. 1224–1238, 1960.

[101] C. L. Kane and E. J. Mele, "Quantum spin Hall effect in graphene," *Phys. Rev. Lett.*, vol. 95, p. 226801, 2005.

[102] D. W. Yuan, W. Xu, Z. Zeng, and F. Lu, "Optical spectrum of a spin-split two-dimensional electron gas," *Phys. Rev. B*, vol. 72, p. 033320, 2005.

[103] C. H. Yang, W. Xu, Z. Zeng, F. Lu, and C. Zhang, "Optical spectrum of a two-dimensional hole gas in the presence of spin-orbit interaction," *Phys. Rev. B*, vol. 74, p. 075321, 2006.

[104] L. C. Gomes and A. Carvalho, "Phosphorene analogues: Isoelectronic two-dimensional group-IV monochalcogenides with orthorhombic structure," *Phys. Rev. B*, vol. 92, p. 085406, 2015.

[105] C. Kamal, A. Chakrabarti, and M. Ezawa, "Direct band gaps in group IV-VI monolayer materials: Binary counterparts of phosphorene," *Phys. Rev. B*, vol. 93, p. 125428, 2016.

[106] L. Medrano Sandonas, D. Teich, R. Gutierrez, T. Lorenz, A. Pecchia, G. Seifert, and G. Cuniberti, "Anisotropic thermoelectric response in two-dimensional puckered structures," *The Journal of Physical Chemistry C*, vol. 120, no. 33, pp. 18841–18849, 2016.

[107] Z. Tian, C. Guo, M. Zhao, R. Li, and J. Xue, "Two-dimensional SnS: A phosphorene analogue with strong in-plane electronic anisotropy," *ACS Nano*, vol. 11, no. 2, p. 2219–2226, 2017.

[108] M. Kurpas, M. Gmitra, and J. Fabian, "Spin-orbit coupling and spin relaxation in phosphorene: Intrinsic versus extrinsic effects," *Phys. Rev. B*, vol. 94, p. 155423, 2016.

[109] Z. S. Popović, J. M. Kurdestany, and S. Satpathy, "Electronic structure and anisotropic Rashba spin-orbit coupling in monolayer black phosphorus," *Phys. Rev. B*, vol. 92, p. 035135, 2015.

[110] J. Zhou, W.-Y. Shan, and D. Xiao, "Spin responses and effective hamiltonian for the two-dimensional electron gas at the oxide interface $LaAlO_3$ /$SrTiO_3$," *Phys. Rev. B*, vol. 91, p. 241302, 2015.

[111] A. Mawrie and T. K. Ghosh, "Optical conductivity of a 2DEG with anisotropic Rashba interaction at the interface of $LaAlO_3$ /$SrTiO_3$," *Journal of Physics: Condensed Matter*, vol. 28, no. 42, p. 425302, 2016.

[112] D. Yudin and I. A. Shelykh, "Two-dimensional electron gas in the regime of strong light-matter coupling: Dynamical conductivity and all-optical measurements of Rashba and Dresselhaus coupling," *Phys. Rev. B*, vol. 94, p. 161404, Oct 2016.

[113] T.-H. Liu and C.-C. Chang, "Anisotropic thermal transport in phosphorene: effects of crystal orientation," *Nanoscale*, vol. 7, pp. 10648–10654, 2015.

[114] F. Xia, H. Wang, and Y. Jia, "Rediscovering black phosphorus as an anisotropic layered material for optoelectronics and electronics," *Nature Communications*, vol. 5, p. 4458, 2014.

[115] A. S. Rodin, A. Carvalho, and A. H. Castro Neto, "Strain-induced gap modification in black phosphorus," *Phys. Rev. Lett.*, vol. 112, p. 176801, 2014.

[116] L. Magarill, A. Chaplik, and M. Éntin, "Spin-plasmon oscillations of the two-dimensional electron gas," *Journal of Experimental and Theoretical Physics*, vol. 92, no. 1, pp. 153–158, 2001.

[117] A. Bácsi and A. Virosztek, "Low-frequency optical conductivity in graphene and in other scale-invariant two-band systems," *Phys. Rev. B*, vol. 87, p. 125425, 2013.

[118] F. Cadiz, D. Paget, and A. C. H. Rowe, "Effect of Pauli blockade on spin-dependent diffusion in a degenerate electron gas," *Phys. Rev. Lett.*, vol. 111, p. 246601, 2013.

[119] W. Ebeling, D. Blaschke, R. Redmer, H. Reinholz, and G. Ropke, "The influence of Pauli blocking effects on the properties of dense hydrogen," *Journal of Physics A: Mathematical and Theoretical*, vol. 42, no. 21, p. 214033, 2009.

[120] H. J. Krenner, E. C. Clark, T. Nakaoka, M. Bichler, C. Scheurer, G. Abstreiter, and J. J. Finley, "Optically probing spin and charge interactions in a tunable artificial molecule," *Phys. Rev. Lett.*, vol. 97, p. 076403, 2006.

[121] Y. Liu and R. F. Willis, "Plasmon-phonon strongly coupled mode in epitaxial graphene," *Physical Review B*, vol. 81, no. 8, p. 081406, 2010.

[122] E. H. Hwang, R. Sensarma, and S. Das Sarma, "Plasmon-phonon coupling in graphene," *Phys. Rev. B*, vol. 82, p. 195406, 2010.

[123] V. W. Brar, M. S. Jang, M. Sherrott, S. Kim, J. J. Lopez, L. B. Kim, M. Choi, and H. Atwater, "Hybrid surface-phonon-plasmon polariton modes in graphene/monolayer h-BN heterostructures," *Nano Lett.*, vol. 14, no. 7, pp. 3876–3880, 2014.

[124] M. Moreno-Moreno, G. Lopez-Polin, A. Castellanos-Gomez, C. Gomez-Navarro, and J. Gomez-Herrero, "Environmental effects in mechanical properties of few-layer black phosphorus," *2D Materials*, vol. 3, no. 3, p. 031007, 2016.

[125] J. Gao, G. Zhang, and Y.-W. Zhang, "The critical role of substrate in stabilizing phosphorene nanoflake: A theoretical exploration," *Journal of the American Chemical Society*, vol. 138, pp. 4763–4771, 2016.

[126] C. R. Dean, A. F. Young, I. Meric, C. Lee, L. Wang, S. Sorgenfrei, K. Watanabe, T. Taniguchi, P. Kim, K. Shepard, *et al.*, "Boron nitride substrates for high-quality graphene electronics," *Nat. Nanotechnol.*, vol. 5, pp. 722–726, 2010.

[127] A. Mogulkoc, Y. Mogulkoc, A. N. Rudenko, and M. I. Katsnelson, "Polaronic effects in monolayer black phosphorus on polar substrates," *Phys. Rev. B*, vol. 93, p. 085417, 2016.

[128] M. Zarenia, O. Leenaerts, B. Partoens, and F. M. Peeters, "Substrate-induced chiral states in graphene," *Phys. Rev. B*, vol. 86, p. 085451, 2012.

[129] H. Yan, T. Low, W. Zhu, Y. Wu, M. Freitag, X. Li, F. Guinea, P. Avouris, and F. Xia, "Damping pathways of mid-infrared plasmons in graphene nanostructures," vol. 7, pp. 394–399, 2013.

[130] Z. Liu and K. Aydin, "Localized surface plasmons in nanostructured monolayer black phosphorus," *Nano Lett.*, vol. 9, no. 1, pp. 312–316, 2016.

[131] M. A. Stroscio and M. Dutta, *Phonons in nanostructures.* Cambridge University Press, 2001.

[132] J.-H. Chen, C. Jang, S. Xiao, M. Ishigami, and M. S. Fuhrer, "Intrinsic and extrinsic performance limits of graphene devices on SiO_2," *Nature Nanotechnology*, vol. 3, pp. 206–209, 2008.

[133] V. Perebeinos and P. Avouris, "Inelastic scattering and current saturation in graphene," *Phys. Rev. B*, vol. 81, p. 195442, May 2010.

[134] I.-T. Lin and J.-M. Liu, "Surface polar optical phonon scattering of carriers in graphene on various substrates," *Appl. Phys. Lett.*, vol. 103, no. 8, pp. 081606, 2013.

[135] Z.-W. Wang, L. Liu, and Z.-Q. Li, "Energy gap induced by the surface optical polaron in graphene on polar substrates," *Appl. Phys. Lett.*, vol. 106, no. 10, pp. 101601, 2015.

[136] W. Xiaoguang, F. M. Peeters, and J. T. Devreese, "Plasmon-phonon coupling in a two-dimensional electron gas," *Phys. Rev. B*, vol. 32, pp. 6982–6985, Nov 1985.

[137] E. H. Hwang and S. Das Sarma, "Surface polar optical phonon interaction induced many-body effects and hot-electron relaxation in graphene," *Phys. Rev. B*, vol. 87, p. 115432, Mar 2013.

[138] K. Kaasbjerg, K. S. Thygesen, and K. W. Jacobsen, "Phonon-limited mobility in n-type single-layer MoS_2 from first principles," *Phys. Rev. B*, vol. 85, p. 115317, Mar 2012.

[139] R. Jalabert and S. Das Sarma, "Quasiparticle properties of a coupled two-dimensional electron-phonon system," *Phys. Rev. B*, vol. 40, pp. 9723–9737, Nov 1989.

[140] V. Perebeinos, S. V. Rotkin, A. G. Petrov, and P. Avouris, "The effects of substrate phonon mode scattering on transport in carbon nanotubes," *Nano Lett.*, vol. 9, no. 1, pp. 312–316, 2008.

[141] S. Ahn, E. H. Hwang, and H. Min, “Inelastic carrier lifetime in a coupled graphene/electron-phonon system: Role of plasmon-phonon coupling,” *Phys. Rev. B*, vol. 90, p. 245436, 2014.

[142] S. Fratini and F. Guinea, “Substrate-limited electron dynamics in graphene,” *Phys. Rev. B*, vol. 77, p. 195415, May 2008.

[143] W.-K. Tse and S. Das Sarma, “Phonon-induced many-body renormalization of the electronic properties of graphene,” *Phys. Rev. Lett.*, vol. 99, p. 236802, 2007.

[144] C. Zhang and Y. Takahashi, “Dynamical conductivity of a two-layered structure with electron-acoustic phonon coupling,” *Journal of Physics: Condensed Matter*, vol. 5, no. 28, p. 5009, 1993.

[145] S. Sarma and B. Mason, “Optical phonon interaction effects in layered semiconductor structures,” *Annals of Physics*, vol. 163, no. 1, pp. 78 – 119, 1985.

[146] A. N. Rudenko and M. I. Katsnelson, “Quasiparticle band structure and tight-binding model for single- and bilayer black phosphorus,” *Phys. Rev. B*, vol. 89, p. 201408, 2014.

[147] A. Manjanath, A. Samanta, T. Pandey, and A. K. Singh, “Semiconductor to metal transition in bilayer phosphorene under normal compressive strain,” *Nanotechnology*, vol. 26, no. 7, p. 075701, 2015.

[148] Y. Mohammadi and B. A. Nia, “Strain engineering the charged-impurity-limited carrier mobility in phosphorene,” *Superlattices and Microstructures*, vol. 89, pp. 204–215, 2016.

[149] B. Mohan, A. Kumar, and P. Ahluwalia, “Electronic and optical properties of silicene under uni-axial and bi-axial mechanical strains: A first principle study,” *Physica E: Low-dimensional Systems and Nanostructures*, vol. 61, pp. 40–47, 2014.

[150] H. Shi, H. Pan, Y.-W. Zhang, and B. Yakobson, “Quasiparticle band structures and optical properties of strained monolayer MoS_2 and WS_2,” *Phys. Rev. B*, vol. 87, p. 155304, Apr 2013.

[151] W. S. Yun, S. W. Han, S. C. Hong, I. G. Kim, and J. D. Lee, "Thickness and strain effects on electronic structures of transition metal dichalcogenides: 2H-MX_2 semiconductors (M= Mo, W; X = S, Se, Te)," *Phys. Rev. B*, vol. 85, p. 033305, Jan 2012.

[152] Y. Ge, W. Wan, F. Yang, and Y. Yao, "The strain effect on superconductivity in phosphorene: a first-principles prediction," *New Journal of Physics*, vol. 17, no. 3, p. 035008, 2015.

[153] G. Q. Huang and Z. W. Xing, "Band-gap tunability and dynamical instability in strained monolayer and bilayer phosphorenes," *Journal of Physics: Condensed Matter*, vol. 27, no. 17, p. 175006, 2015.

[154] T. Ando, A. B. Fowler, and F. Stern, "Electronic properties of two-dimensional systems," *Rev. Mod. Phys.*, vol. 54, pp. 437–672, 1982.

[155] P. K. Pyatkovskiy, "Dynamical polarization, screening, and plasmons in gapped graphene," *Journal of Physics: Condensed Matter*, vol. 21, no. 2, p. 025506, 2009.

[156] S. Das Sarma and Q. Li, "Intrinsic plasmons in two-dimensional Dirac materials," *Phys. Rev. B*, vol. 87, p. 235418, 2013.

[157] K. Thygesen, "Calculating excitons, plasmons, and quasiparticles in 2d materials and van der Waals heterostructures: Topical Review," *2D materials*, vol. 4, no. 2, p. 022004, 2017.

[158] D. E. C. T. J. Constant, S. M. Hornett and E. Hendry, "All-optical generation of surface plasmons in graphene," *Nature Physics*, vol. 12, p. 124, 2016.

[159] D. E. C. Frank H. L. Koppens and F. J. G. de Abajo, "Graphene plasmonics: A platform for strong light–matter interactions," *Nano Lett.*, vol. 11, no. 8, p. 3370, 2011.

[160] A. Agarwal, S. Chesi, T. Jungwirth, J. Sinova, G. Vignale, and M. Polini, "Plasmon mass and Drude weight in strongly spin-orbit-coupled two-dimensional electron gases," *Phys. Rev. B*, vol. 83, p. 115135, 2011.

[161] A. Scholz, T. Dollinger, P. Wenk, K. Richter, and J. Schliemann, "Plasmons in spin-orbit coupled two-dimensional hole gas systems," *Phys. Rev. B*, vol. 87, p. 085321, 2013.

[162] F. M. D. Pellegrino, G. G. N. Angilella, and R. Pucci, "Linear response correlation functions in strained graphene," *Phys. Rev. B*, vol. 84, p. 195407, 2011.

[163] F. Jin, R. Roldán, M. I. Katsnelson, and S. Yuan, "Screening and plasmons in pure and disordered single- and bilayer black phosphorus," *Phys. Rev. B*, vol. 92, p. 115440, 2015.

[164] Y. Jiang, R. Roldán, F. Guinea, and T. Low, "Magnetoelectronic properties of multilayer black phosphorus," *Phys. Rev. B*, vol. 92, p. 085408, 2015.

[165] B. N. Narozhny and A. Levchenko, "Coulomb drag," *Rev. Mod. Phys.*, vol. 88, p. 025003, 2016.

[166] A. N. Rudenko and M. I. Katsnelson, "Quasiparticle band structure and tight-binding model for single- and bilayer black phosphorus," *Phys. Rev. B*, vol. 89, p. 201408, 2014.

[167] J. M. Pereira and M. I. Katsnelson, "Landau levels of single-layer and bilayer phosphorene," *Phys. Rev. B*, vol. 92, p. 075437, 2015.

[168] W.-L. You and X.-F. Wang, "Dynamic screening and plasmon spectrum in bilayer graphene," *Nanotechnology*, vol. 23, no. 50, p. 505204, 2012.

[169] B. N. Narozhny, M. Titov, I. V. Gornyi, and P. M. Ostrovsky, "Coulomb drag in graphene: Perturbation theory," *Phys. Rev. B*, vol. 85, p. 195421, 2012.

[170] J. O. Island, G. A. Steele, H. S. J. van der Zant, and A. Castellanos-Gomez, "Environmental instability of few-layer black phosphorus," *2D Materials*, vol. 2, no. 1, p. 011002, 2015.

[171] A. Favron, E. Gaufrès, F. Fossard, A . L'Heureux, N. Y-W. Tang, P. Lévesque, A. Loiseau, R. Leonelli, S. Francoeur, and R. Martel, "Photooxidation and quantum confinement effects in exfoliated black phosphorus," *Nature Materials*, vol. 14, pp. 826–832, 2015.

[172] Y. Cao, A. Mishchenko, G. L. Yu, E. Khestanova, A. P. Rooney, E. Prestat, A. V. Kretinin, P. Blake, M. B. Shalom, C. Woods†, J. Chapman, G. Balakrishnan, I. V. Grigorieva, K. S. Novoselov, B. A. Piot, M. Potemski, K. Watanabe, T. Taniguchi, S. J. Haigh, A. K. Geim, and R. V. Gorbachev, "Quality heterostructures from two-dimensional crystals unstable in air by their assembly in inert atmosphere," *Nano Lett.*, vol. 15, no. 8, pp. 4914–4921, 2015.

[173] Y. E. Lozovik, S. L. Ogarkov, and A. A. Sokolik, "Condensation of electron-hole pairs in a two-layer graphene system: Correlation effects," *Phys. Rev. B*, vol. 86, p. 045429, 2012.

[174] A. Perali, D. Neilson, and A. R. Hamilton, "High-temperature superfluidity in double-bilayer graphene," *Phys. Rev. Lett.*, vol. 110, p. 146803, 2013.

[175] M. Zarenia, A. Perali, F. M. Peeters, and D. Neilson, "Large gap electron-hole superfluidity and shape resonances in coupled graphene nanoribbons," *Scientific Reports*, vol. 6, p. 24860, 2016.

[176] J. Zhang and E. Rossi, "Chiral superfluid states in hybrid graphene heterostructures," *Phys. Rev. Lett.*, vol. 111, p. 086804, Aug 2013.

[177] A. Surrente, A. A. Mitioglu, K. Galkowski, W. Tabis, D. K. Maude, and P. Plochocka, "Excitons in atomically thin black phosphorus," *Phys. Rev. B*, vol. 93, p. 121405, Mar 2016.

[178] O. L. Berman, G. Gumbs, and R. Y. Kezerashvili, "Bose-einstein condensation and superfluidity of dipolar excitons in a phosphorene double layer," *Phys. Rev. B*, vol. 96, p. 014505, Jul 2017.

[179] Z. Gortel and L. ?wierkowski, "Superfluid ground state in electron-hole double layer systems," *Surface Science*, vol. 361, pp. 146 – 149, 1996.

[180] I. Sodemann, D. A. Pesin, and A. H. MacDonald, "Interaction-enhanced coherence between two-dimensional Dirac layers," *Phys. Rev. B*, vol. 85, p. 195136, May 2012.

[181] J.-J. Zhu, S. M. Badalyan, and F. M. Peeters, "Plasmonic excitations in coulomb-coupled n-layer graphene structures," *Phys. Rev. B*, vol. 87, p. 085401, Feb 2013.

[182] Y. E. Lozovik and V. Yudson, "A new mechanism for superconductivity: pairing between spatially separated electrons and holes," *Zh. Eksp. Teor. Fiz*, vol. 71, p. 738, 1976.

[183] L. Benfatto, M. Capone, S. Caprara, C. Castellani, and C. Di Castro, "Multiple gaps and superfluid density from interband pairing in a four-band model of the iron oxypnictides," *Phys. Rev. B*, vol. 78, p. 140502, Oct 2008.

[184] M. Zarenia, D. Neilson, B. Partoens, and F. M. Peeters, "Wigner crystallization in transition metal dichalcogenides: A new approach to correlation energy," *Phys. Rev. B*, vol. 95, p. 115438, Mar 2017.

[185] G. Grüner, "The dynamics of charge-density waves," *Rev. Mod. Phys.*, vol. 60, pp. 1129–1181, Oct 1988.

[186] D. Makogon, R. van Gelderen, R. Roldán, and C. M. Smith, "Spin-density-wave instability in graphene doped near the van Hove singularity," *Phys. Rev. B*, vol. 84, p. 125404, Sep 2011.

[187] Z.-W. Wang, L. Liu, and Z.-Q. Li, "Superconductivity and other macroscopic quantum phenomena," *Physics Today*, vol. 43, no. 12, p. 25, 1990.

[188] R. Peierls, "More surprises in theoretical physics," *Physics Today*, vol. 45, p. 68, 1992.

[189] M. Zarenia, D. Neilson, and F. M. Peeters, "Inhomogeneous phases in coupled electron-hole bilayer graphene sheets: Charge density waves and coupled Wigner crystals," *Sci. Rep.*, vol. 7, p. 11510, 2017.

[190] S. A. Kivelson, I. P. Bindloss, E. Fradkin, V. Oganesyan, J. M. Tranquada, A. Kapitulnik, and C. Howald, "How to detect fluctuating stripes in the high-temperature superconductors," *Rev. Mod. Phys.*, vol. 75, pp. 1201–1241, Oct 2003.

[191] E. E. Hroblak, A. Principi, H. Zhao, and G. Vignale, "Electrically induced charge-density waves in a two-dimensional electron liquid: Effects of negative electronic compressibility," *Phys. Rev. B*, vol. 96, p. 075422, Aug 2017.

[192] C. Brun, Z.-Z. Wang, P. Monceau, and S. Brazovskii, “Surface charge density wave phase transition in $NbSe_3$,” *Phys. Rev. Lett.*, vol. 104, p. 256403, 2010.

[193] C. G. Slough, B. Giambattista, A. Johnson, W. W. McNairy, C. Wang, and R. V. Coleman, “Scanning tunneling microscopy of 1t-$TiSe_2$ and 1t-TiS_2 at 77 and 4.2 k,” *Phys. Rev. B*, vol. 37, pp. 6571–6574, 1988.

[194] C. Tőke and V. I. Fal’ko, “Charge-density-wave states in double-layer structures at a high magnetic field,” *Phys. Rev. B*, vol. 90, p. 035404, Jul 2014.

[195] J. P. Eisenstein, L. N. Pfeiffer, and K. W. West, “Compressibility of the two-dimensional electron gas: Measurements of the zero-field exchange energy and fractional quantum Hall gap,” *Phys. Rev. B*, vol. 50, pp. 1760–1778, Jul 1994.

[196] O. Poplavskyy, M. O. Goerbig, and C. Morais Smith, “Local density of states of electron-crystal phases in graphene in the quantum Hall regime,” *Phys. Rev. B*, vol. 80, p. 195414, Nov 2009.

[197] L. Li, C. Richter, S. Paetel, T. Kopp, J. Mannhart, and R. C. Ashoori, “Very large capacitance enhancement in a two-dimensional electron system,” vol. 332, pp. 825–828, 2011.

[198] J. R. Brent, N. Savjani, E. A. Lewis, S. J. Haigh, D. J. Lewis, and P. O’Brien, “Production of few-layer phosphorene by liquid exfoliation of black phosphorus,” *Chem. Commun.*, vol. 50, pp. 13338–13341, 2014.

[199] L. Shao, H. Ye, Y. Wu, D. Yinxiao, P. Ding, F. Zeng, and Q. Yuan, “Interaction between phosphorene and the surface of a substrate,” *Materials Research Express*, vol. 3, no. 2, p. 025013, 2016.

[200] S. Saberi-Pouya, T. Vazifehshenas, T. Salavati-fard, and M. Farmanbar, “Anisotropic hybrid excitation modes in monolayer and double-layer phosphorene on polar substrates,” *Phys. Rev. B*, vol. 96, p. 115402, Sep 2017.

[201] M. Bokdam, P. A. Khomyakov, G. Brocks, Z. Zhong, and P. J. Kelly, “Electrostatic doping of graphene through ultrathin hexagonal boron nitride films,” *Nano Lett.*, vol. 11, pp. 4631–4635, 2011.

[202] Y. Wu, X. Chen, Z. Wu, S. Xu, T. Han, J. Lin, B. Skinner, Y. Cai, Y. He, C. Cheng, and N. Wang, "Negative compressibility in graphene-terminated black phosphorus heterostructures," *Phys. Rev. B*, vol. 93, p. 035455, Jan 2016.

[203] V. N. Kotov, B. Uchoa, V. M. Pereira, F. Guinea, and A. H. Castro Neto, "Electron-electron interactions in graphene: Current status and perspectives," *Rev. Mod. Phys.*, vol. 84, pp. 1067–1125, Jul 2012.

[204] T. J. Gramila, J. P. Eisenstein, A. H. MacDonald, L. N. Pfeiffer, and K. W. West, "Mutual friction between parallel two-dimensional electron systems," *Phys. Rev. Lett.*, vol. 66, pp. 1216–1219, Mar 1991.

[205] G. Giuliani and G. Vignale, *Quantum theory of the electron liquid.* Cambridge University Press, 2005.

[206] I. Gradshteyn and I. Ryzhik, *Table of Integrals, Series, and Products.* Academic Press, 2007.

[207] Z. Jin, J. T. Mullen, and K. W. Kim, "Highly anisotropic electronic transport properties of monolayer and bilayer phosphorene from first principles," *Appl. Phys. Lett.*, vol. 109, p. 053108, 2016.

[208] G. C. Constantinescu and N. D. M. Hine, "Multipurpose black-phosphorus/h-BN heterostructures," *Nano Lett.*, vol. 16, no. 4, pp. 2586–2594, 2016.

[209] E. DiMasi, M. C. Aronson, J. F. Mansfield, B. Foran, and S. Lee, "Chemical pressure and charge-density waves in rare-earth tritellurides," *Phys. Rev. B*, vol. 52, pp. 14516–14525, Nov 1995.

[210] A. Fang, N. Ru, I. R. Fisher, and A. Kapitulnik, "STM studies of TbTe_3: Evidence for a fully incommensurate charge density wave," *Phys. Rev. Lett.*, vol. 99, p. 046401, Jul 2007.

[211] L. Perfetti, P. A. Loukakos, M. Lisowski, U. Bovensiepen, M. Wolf, H. Berger, S. Biermann, and A. Georges, "Femtosecond dynamics of electronic states in the mott insulator 1t-TaS_2 by time resolved photoelectron spectroscopy," *New J. Phys.*, vol. 10, no. 5, p. 053019, 2008.

[212] C. L. Smallwood, R. A. Kaindl, and A. Lanzara, “Ultrafast angle-resolved photoemission spectroscopy of quantum materials,” *EPL*, vol. 115, no. 2, p. 27001, 2016.

CURRICULUM VITAE

Samira Saberi-Pouya

CURRICULUM VITAE

☎ *+32 493 067 857, +98 905 837 2943*
✉ *s_saberi@sbu.ac.ir & samira.saberi-pouya@uantwerpen.be*

Personal Information

Date of borth	**28 March 1988**.
Gender	**Female**.
Nationality	**Iranian**.

Education

2006–2010	**Bachelor of Science**, *Shahid Chamran University*, Ahwaz, Khuzestan, Iran. Top 3% of Bachalor students
2010–2013	**Master of Science**, *Shahid Beheshti University*, Tehran,Iran. Ranked first between Master students
2013–2018	**Ph.D condidate**, *Shahid Beheshti University*, Tehran,Iran. Ranked first between Ph.D students
2016–2018	**Ph.D condidate**, *Antwerpen University*, Antwerp, Belgium.

Master thesis

title	Diclusters Stopping Power of Semiconductor Systems and Graphene
supervisors	Dr. Taraneh Vazifehshenas
Grade	Excellent

Ph.D thesis

title	Many body Properties in Monolayer and Double-layer Phosphorene
Supervisors	Dr. Taraneh Vazifehshenas Tehran(Iran) and Professor Francois Peeters Antwerpen (Belgium)

Publications

1 **Strong anisotropic optical conductivity in two dimensional puckered structures: The role of Rashba effect** , *S Saberi-Pouya, T Vazifehshenas, T Salavati-fard, M Farmanbar, FM Peeters,*, Physical Review B, 96 (7), 075411 (2017).

2 **Anisotropic hybrid excitation modes in monolayer and double-layer phosphorene on polar substrates** , *S Saberi-Pouya, T Vazifehshenas, T Salavati-fard, M Farmanbar*, Physical Review B, 96 (11), 115402 (2017).

3 **Coulomb drag in anisotropic systems: a theoretical study on a double-layer phosphorene** , *S Saberi-Pouya, T Vazifehshenas, M Farmanbar, T Salavati-Fard,*, Journal of Physics: Condensed Matter, 28 (28), 285301 (2016) .

4 **Local Field Correction Effect on Dicluster Stopping Power in a Strongly Coupled Two-Dimensional Electron Gas System**, *T Vazifehshenas, S Saberi-Pouya,*, Journal of Sciences, Islamic Republic of Iran , 24 (1), 81-85 (2013).

5 **Plasmon modes in monolayer and double-layer black phosphorus under applied uniaxial strain**, *S Saberi-Pouya, T Vazifehshenas, M.Saleh, M Farmanbar and T Salavati-fard*, Journal of Applied Physics 123, 174301 (2018).

6 **Highly anisotropic superfluidity in electron-hole phosphorene monolayers** , *S Saberi-Pouya, M Zarenia, A. Perali, T. Vazifehshenas and F.M. Peeters,*, Physical Review B 97, 174503 (2018).

7 **Anisotropic charge density wave in electron-hole double phosphorene monolayers**, *S Saberi-Pouya, M Zarenia, T. Vazifehshenas and F.M. Peeters*, Submited to PRB.

Conferences Proceeding and Workshops

1 **Stopping power of a nanolayer for slow two-ion projectiles beyond the Random Phase Approximation**, *T Vazifehshenas, S Saberi-Pouya,*, 5th International Congress on Nanoscience and Nanotechnology, (ICNN2014), 407-409.
Theran, Iran (2014).

2 **Diclusters Stopping Power in Semiconductor nanolayers and Graphene**, *T Vazifehshenas, S Saberi-Pouya*, Proceedings of the 5th International Conference on Nanostructures (ICNS5), 3 1432-1434 Kish island.
Iran (2014).

3 International advanced mini-workshop on recent progress on graphene, Kish Island, Iran, (2014).

4 Second PAM International School on Emergent Quantum Phenomena in graphene, department physics at Sharif University of Technology, Iran, 26-28 April (2015).

5 **Highly anisotropic electron-hole superfluidity in double layer phosphorene**, *S Saberi-Pouya, M Zarenia, T. Vazifehshenas and F.M. Peeters,*, Solvay Workshop, Brussels, 6-8 September (2017)..

6 **Anisotropic Charge Density Wave in Electron-Hole Double Phosphorene Monolayers: The Role of Negative Compressibility**, *S Saberi-Pouya, M Zarenia, T. Vazifehshenas and F.M. Peeters,*, General Scientific Meeting of the Belgian Physical Society, Antwerpen, April 11 (2018)..

7 **Highly anisotropic superfluidity in electron-hole phosphorene monolayers**, *S Saberi-Pouya, M Zarenia, A. Perali, T. Vazifehshenas and F.M. Peeters,*, Conference on Multi-condensate Superconductivity and superfluidity in Solids and Ultracold Gases, ICTP, Trieste, Italy 14-18 May (2018)..

Honors and Awards

I Ranked first in the Ph.D. class in Shahid Beheshti University, 2013-2014.

II Ranked first in Condensed matter physics M.Sc graduated students in Shahid Beheshti University, 2013.

III Accepted as a top(talented) student for Ph.D. Position in Department of Physics at Shahid Beheshti University without an entrance exam as a qualified M.Sc student.

IV Elected as a talented student for Shahid Shahriary scholarship.

Languages

Language 1	Persion
Language 2	English

Computer skills

Category 1	Programming : Fortran (Excellent), Python (basic knowledge)
Category 2	Scientific packages/programs: Matlab, Mathematica, Origin, LaTex

Interests

Hobby 1	Reading
Hobby 2	Calligraphy
Hobby 3	Movie
Hobby 4	Teakwondo

Advanced Courses

- Quantum field theory
- Many-Body theory of Equilibrium systems I and II
- Many-Body theory of Non-Equilibrium systems
- Advanced Solid-State Physics I and II
- Advanced Quantum Mechanics I and II
- Advanced Quantum Optics
- Quantum Transport

Teaching Experiences

1 Master of General Physics: Physics Holiday II for bachelor students (2016)

2 Teaching Assistant: Advanced Quantum Mechanics (I and II): Graduate Course SBU (2015)

3 Master of Lab : General Physics1 SBU (2015)

4 Teaching Assistant: Solid State Physic1: Undergraduate Course SBU (2014)